Fall 2016

Design and analysis of an axisymmetric aerospike supersonic micro-nozzle for a refrigerant-based cold-gas propulsion system for small satellites

Abdalla Ali Bani

Recommended Citation

Bani, Abdalla Ali, "Design and analysis of an axisymmetric aerospike supersonic micro-nozzle for a refrigerant-based cold-gas propulsion system for small satellites" (2016). *Masters Theses*. 7591.
https://scholarsmine.mst.edu/masters_theses/7591

DESIGN AND ANALYSIS OF AN AXISYMMETRIC AEROSPIKE SUPERSONIC MICRO-NOZZLE FOR A REFRIGERANT-BASED COLD-GAS PROPULSION SYSTEM FOR SMALL SATELLITES

by

ABDALLA ALI BANI

A THESIS

Presented to the Graduate Faculty of the

MISSOURI UNIVERSITY OF SCIENCE AND TECHNOLOGY

In Partial Fulfillment of the Requirements for the Degree

MASTER OF SCIENCE

in

MECHANICAL ENGINEERING

2016

Approved by

Dr. Henry J. Pernicka, Advisor
Dr. David W. Riggins
Dr. Joshua L. Rovey

ABSTRACT

The cold-gas propulsion system being developed by M-SAT requires improvements to its original nozzle design. This study documents the research, design, and analysis of a supersonic plug nozzle concept that could be integrated to the refrigerant-based cold-gas propulsion system to possibly improve its performance. As documented in this thesis, CFD analysis showed that the outlined nozzle design method resulted in a feasible nozzle concept that has the ability to out-perform a conventional nozzle of the same area ratio. The flow-fields and thrust of the aerospike nozzle, for the full and truncated nozzles, were investigated. The purpose of this study is to investigate other rocket nozzles that might have the ability to improve performance of a propulsion system without a large penalty on vehicle mass or cost. Based on the information presented in this thesis, university-based satellite teams can manipulate the inputs of the design and analysis methods to investigate the use of an aersopike nozzle design concept to meet their design goals.

ACKNOWLEDGMENTS

I would like to express my sincere thanks and gratitude to my advisor, Dr. Henry Pernicka, who gave me the opportunity to be a part of the outstanding M-SAT project and for always donating his time and effort to offer help and guidance when needed, and also for being a great advisor and mentor in and outside of research work. I am forever indebted to your scholarship, professionalism, kindness and friendship.

I would also like to extend my thanks and appreciation to my committee members, Dr. David Riggins and Dr. Joshua Rovey. I thank Dr. Riggins for your time and effort and for introducing me to aerospace engineering through your classes that I have enjoyed greatly. I would like to thank Dr. Rovey for introducing me to the fundamentals of propulsion systems and for always willing to put in time and effort to provide assistance and feedback. I would like to thank Dr. Pernicka, Dr. Riggins, and Dr. Rovey for being outstanding educators and scholars and for positively impacting the lives of countless young men and women.

I would also like to thank Dr. Isaac and Dr. Hosder for providing assistance and input in the computational fluid dynamics areas of this research. I would also like to extend my thanks to Dr. Homan for volunteering his time to help with this research.

My thanks go to the current and previous M-SAT and LCQ team members as it was their hardwork and dedication that made this work possible. I would like to specifically mention David Hobbs, Garret McMillan, Bradyn Morton and Austin Holmsley for their great engineering skills and leadership.

Finally, I would like to thank my parents who have sacrificed so much to support me and my brothers throughout our lives and education, for if it was not for their continued support and sacrifice I wouldn't be where I am today. Thank you for allowing me to dream.

TABLE OF CONTENTS

Page

SECTION

APPENDICES

LIST OF ILLUSTRATIONS

Figure Page

LIST OF TABLES

1. INTRODUCTION

1.1. SMALL SATELLITE BACKGROUND AND HISTORICAL PERSPECTIVE

The beginning of the Space Age was marked by the launch of the first satellites in the International Geophysical Year (IGY) of 1957-58. Sputnik I, Explorer I, and Vanguard 1 were the first satellites launched to space and they were a major milestone in the quest by humans to reach the final frontier, and they were all small satellites. The Soviet Union had the lead when it launched Sputnik I on October 4, 1957. The chirping sound of Sputnik I (Figure 1.1 taken from [1]) transmission, famously called the "Deep Beep-Beep" by the Associated Press, lasted three-tenths of a second, followed by three-tenths of a second pause [2]. That three-tenths of a second marked the first transmission to Earth from "outer space." The beach ball-sized Sputnik I was a polished aluminum-magnesium-titanium sphere and had a mass of a mere 83.6 kg (184 lbs) and had a diameter of 58.5 cm [3]. Even though Sputnik I was very simple and did not do more than orbit the Earth and send radio blips, its effects on geopolitics were unprecedented and grew greater with time. Sputnik I proved that a spacecraft orbiting Earth could survive in hostile space environment without being punctured by meteorites or having its electronics damaged by solar or cosmic radiation [3]. It also transmitted internal and skin temperature data to the ground for a few weeks before its batteries became depleted. It allowed physicists to measure alterations in the paths of its radio transmission to determine ion density in the upper Earth atmosphere [3]. Sputnik I orbited the Earth 1440 times and on January 4, 1958, three months after its launch, Sputnik descended deep enough into the upper atmosphere to be vaporized by aerodynamic heating [3].

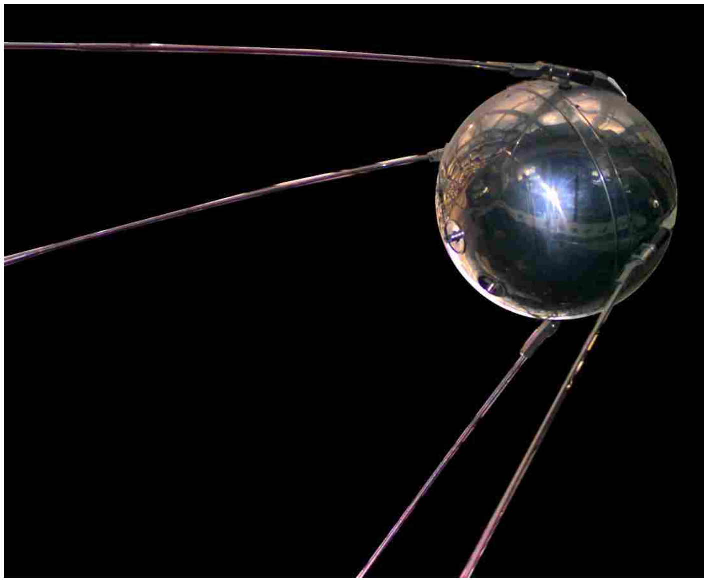

Figure 1.1 Sputnik I Satellite

The Soviet Sputnik II followed on November 3, 1957, carrying a dog, Laika, making it the first creature to orbit the Earth. Sputnik II was a high cone-shaped capsule and had mass of around 500 kg. Sputnik I was the first and last small satellite launched by the Soviet Union [3].

As a quick response to the success of the Soviet Union's Sputnik I launch, the United States launched its fist satellite on January 31, 1958, Explorer [4]. Explorer I (Figure 1.2 taken from [5]) was designed and built and operated by NASA Jet Propulsion Laboratory (JPL) and carried a cosmic ray detector which helped the Principal Investigator of the mission, Dr. James Van Allen, to discover the radiation belts, later to be known as Van Allen Belts, around earth [4]. Explorer I's mass was a mere 13.9 kg, of which 8.3 kg was the actual payload that consisted of a cosmic-ray detector and a micrometeorite detector [3]. Explorer I made its final transmission to Earth on May 23, 1958, after approximately

105 days on orbit [3]. However, the spacecraft remained in orbit for 12 years until May 31, 1970 when it re-entered Earth's atmosphere and was destroyed [4]. Explorer I was not only the first United States satellite, but also the first satellite to carry science instruments [5].

Figure 1.2 From Left to Right: Dr. William H. Pickering, former JPL Director, Dr. James van Allen, and Dr. Werhner von Braun Holding Explorer 1 Spacecraft

After Explorer I was launched, The United States launched its second satellite, Vanguard I (Figure 1.3 taken from [6]), to orbit on March 17, 1958, almost six weeks after the launch of Explorer I. The Vanguard project suffered major setbacks before its eventual success. Two unsuccessful launch attempts took place on December 6, 1957 and again on February 5, 1958 [3]. The first attempt suffered a first-stage motor turbine underpressurization problem and fell and exploded on its launchpad seconds after it took off [3]. The second attempt broke up 57 seconds after launch due to a control system failure on February 5, 1958 [3]. The aluminum spherical shaped Vanguard I weighed only 1.46 kg and was 16.5 cm in diameter and was designed to test the launch capabilities of a three-stage launch vehicle and to investigate the effects of the environment on a satellite and its systems in Earth orbit [6]. Vanguard I was also used to collect geodetic measurements through orbital analysis and was the first satellite to use solar cell power [6]. Vanguard I paved the way for the rest of the Vanguard series. Despite its small size, Vanguard I had two separate transmitters. Its battery powered-transmitter provided internal package temperature for 16 days and and sent tracking signals for an additional 20 years [3]. Its solar-powered transmitter provided measurements of the temperature of the inside surface of the satellite's shell and sent tracking signals for more than six years and 25,000 orbits [3]. As of today, Vanguard I is still orbiting Earth and it is expected to continue doing so for another 150 years [3].

These major missions ushered in the Space Age and paved the way for more complex and powerful satellites. The first satellites launched into orbit were all small satellites, however it was not until 1991 that the first small satellite with a propulsion system was launched to orbit. Over the last five decades more than 860 microsatellites, 680 nanosatellites, and 38 picosatellites have been launched worldwide [3]. Small satellites have proved to be very useful since the beginning of the Space Age. They have recorded data on terrestrial and space environment near the Earth and the Moon [3]. Small satellites were also very important in helping in the search of other planets in other star systems [3]. And their effect on telecommunication systems that we enjoy today is astronomical. Furthermore, due to

Figure 1.3 Vanguard I Satellite

their lower cost, small satellites served a platform to develop new space technologies and as hands-on educational tools for many students in many universities across the world.

1.2. SMALL SATELLITE CLASSIFICATION

Satellites can be classified in many different ways. They can be classified, for example, based on orbit, function, or size. Classifying satellites based on size is, usually, a good indicator of their function and cost. Generally, satellites with masses over 1000 kg (2000 lbs) are categorized as large satellites, satellites having masses between 500-1000 kg (1000-2000 lbs) are usually classified as medium-sized satellites, and small satellites are defined as satellites with masses of 500 kg (1000 lbs) or less [7]. However, the phrase "small satellite" is very broad and it is more beneficial to classify small satellites according to their mass as well. The terminology adopted for categorizing small satellites is shown in Table 1.1 [7].

Limitations of size and mass capabilities of launch systems dictated the use of small satellites since the beginning of the space program. About 20% of all satellites flown are small satellites of mass less than 400 kg [7]. Historically, small satellites are attributed with simplicity and limited payload capability. However, the advancements and microminimaztion that created the modern computers and cell phones have, also, allowed an increase in the capability and reliability of small satellites [7]. The fewer requirements and the higher tolerance of risk associated with small satellites have allowed them to be developed in a fraction of the time and cost associated with large satellites.

Table 1.1 Small Satellite Classification [7]

Category	**Mass (kg)**
Minisatellite	100 – 500
Microsatellite	10 – 100
Nanosatellite	1 – 10
Picosatellite	0.1 – 1
Femtosatellite	< 0.1

1.3. TYPES OF SATELLITE PROPULSION

The word "propulsion" is derived from the past participle of the of Latin verb propellere, propulsus, which means to drive away. Propulsion is the act of changing the motion of a body in a certain direction [8]. The function of a propulsion system is to provide the force (thrust) that moves the body. This process is done by ejecting matter (propellant) that is previously stored in the vehicle through a nozzle. The significance of propulsion systems is in providing enough force to a flying vehicle. Propulsion systems can be classified based on the type of vehicle they drive, their basic function, or the type of fuel they utilize. Basic propulsion systems have been used as far as 800 years ago by the Chinese. However, major advancements and developments in aero and space vehicles propulsion systems came about in the twentieth century. Satellite propulsion systems can be classified by the type of energy source they utilize in three major categories.

The use of certain propulsion system in a satellite depend on the mission requirements. The required thrust and the lifespan of a certain mission will usually dictate which method of propulsion chosen by engineers. Table 1.2 [9] summarizes the specific impulse (I_{sp}) and thrust values for different propulsion methods. As can be seen in the table, chemical propulsion provides the highest thrust values and the lowest I_{sp} values. On the other side of the propulsion spectrum, electrical propulsion methods have the highest I_{sp} capabilities and the lowest thrust values.

Specific impulse is a very important figure of merit in propulsion systems. Much like the miles per gallon in an automobile, the specific impulse measures the performance and efficiency of a certain propulsion system. It is defined as the total impulse (or change in momentum) per unit weight of propellant supplied to the propulsion system [10]. Specific impulse is measured in seconds. According to Newton's third law of motion, thrust is the reaction experienced by a structure of a vehicle due to the ejection of matter, usually at high velocities. Thrust is a force generated by the propulsion system acting on the vehicle. Approximate performance values of exhaust velocities as a function of typical vehicle accelerations for various propulsion systems, with zero payload, are shown in Figure 1.4 taken from [8].

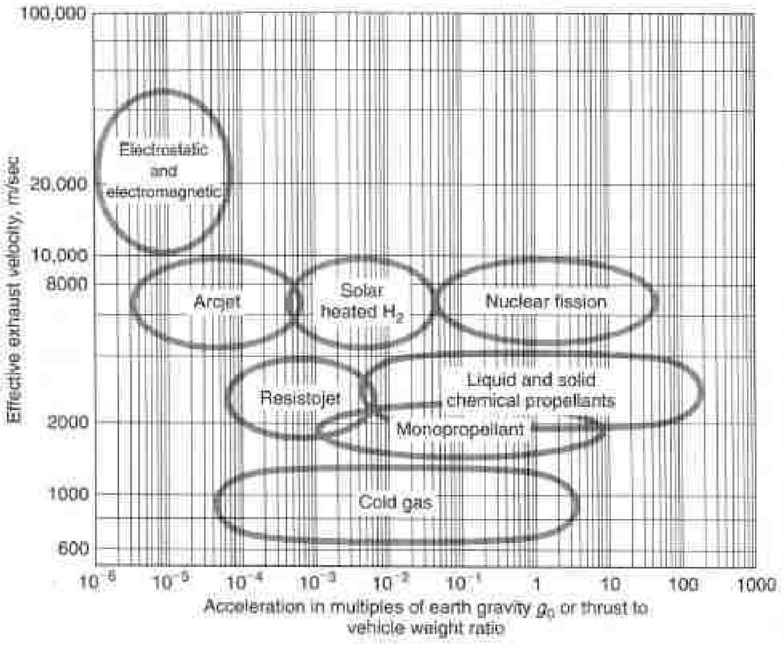

Figure 1.4 Exhaust Velocities as Function of Vehicle Acceleration [8]

1.3.1. Chemical Propulsion. Space travel has always been driven and limited, at the same time, by chemical propulsion. Chemical rocket engines are used as first and upper stage engines to propel a payload into an initial orbit [7]. These large expensive engines are necessary to haul a small amount of payload. The very high energy from the high-pressure combustion process of propellant chemicals, in the form of an oxidizer and a fuel, results in extremely high-temperature reaction products that are then expanded in a nozzle and accelerated to very high velocities. The huge thrust of chemical propulsion systems made them the primary propulsion mechanism to enable spaceflight. However, this high thrust capability comes with a big trade-off in efficiency. The mass of the propellants in chemical rockets makes up the majority of the vehicle's mass leaving only a small portion for the actual payload [8]. It is very critical for the future of spaceflight to continue developing a solution

Table 1.2 Comparison of I_{sp} and Thrust Values for Different Propulsion Systems [9]

Propulsion System	**Type**	$\mathbf{I_{SP}}$ (sec)	**Thrust (N)**
Cold Gas	**Cold Gas**	50 – 75	0.05 – 200
Chemical	**Solid**	280 – 300	10 – 10^6
	Liquid		
	Monopropellant	150 – 225	50 – $5\text{x}10^6$
	Bipropellant	330 – 450	3 – $5\text{x}10^6$
	Hybrid	225	225 – $3.5\text{x}10^6$
Electrical	**Electrothermal**		
	Resistojet	150 – 700	0.005 – 0.5
	Arcjet	450 – 700	0.05 – 5
	Electrostatic		
	Ion	$2\text{x}10^2$ – $6\text{x}10^2$	$5\text{x}10^{-6}$ – 0.5
	Colloid	$1.2\text{x}10^3$	$5\text{x}10^{-6}$ – 0.05
	Hall Effect Thruster	$1.5\text{x}10^3$ – $2.5\text{x}10^3$	$5\text{x}10^{-6}$ – 0.1
	Electromagnetic		
	Magnetoplasmadynamic	$2\text{x}10^3$	25 – 200
	Pulsed Plasma	$1.5\text{x}10^3$	$5\text{x}10^{-6}$ – 0.005
	Pulsed Inductive	$2.5\text{x}10^3$ – $4\text{x}10^3$	2 – $2\text{x}10^3$

that will significantly reduce the cost of launching payloads of all sizes. Developing a more efficient high-thrust propulsion system is one of the biggest challenges facing humans in their quest for outer space and interplanetary travel.

1.3.2. Electrical Propulsion. Electrical propulsion, unlike chemical propulsion, is not bounded by the intrinsic molecular bond energy. Chemical propulsion is inextricably dependable on mass, so there is a huge energy expense associated with placing chemical propulsion in orbit [10]. Electric propulsion has the ability to increase the specific impulse to extremely high values and because, in theory, any amount of electrical energy can be added to any given mass, the propellant mass consumption of an electrical propulsion system can be greatly reduced [7] [10]. However, the high efficiency of this propulsion system results in very low thrust values, between 0.005 to 1 N. In an electrical propulsion system it is necessary to apply the low thrust and accelerations for a long period of time to increase the velocity of the vehicle [8]. Electrical propulsion is classified by three major categories based on propellant acceleration mechanism:

Electrothermal, where heating of the propellant can be achieved by electrical heating through walls, resistojet, or by an electrical arc discharge through the propellant fluid, arcjet [10]. The hot gas is then expanded and accelerated through a nozzle to supersonic velocities.

Electrostatic, where the charged particles are accelerated by electric fields, electrostatic forces. The discrete particles are charged by electron bombardment [8] [10].

Electromagnetic, where the forces on the charged particles is produced by a magnetic field and velocity of the charged particles. Electromagnetic forces are most suitable for pulsed operations producing short bursts of thrust [10].

1.3.3. Cold Gas Propulsion. In cold gas propulsion systems the propellant is accelerated and exhausted through a nozzle. The nozzle allows for the extraction of the fluid dynamic properties of the fluid to produce the desired thrust characteristics. Cold gas systems have the advantage of being very simple. A cold gas system will usually consist of valves, regulators, filters and relief valves connecting the high pressure tank to a nozzle [7]. The thrust of a cold gas systems is generated by releasing a gas, stored under high pressure conditions in a tank, as a cold propellant through a thruster. The cold gas system, also, has the advantage of being safer than traditional chemical propulsion systems because it does not depend on the use of highly explosive or toxic chemicals, such as hydrazine. The cold gas system is a very practical option when simplicity and reliability are required. Cold gas systems can provide very precise orbital maneuvers due to their low thrust capabilities. This low thrust requirements makes most chemical propulsion systems unfit when very precise orbital maneuvers are required for small satellites. Furthermore, the size limitations of small satellites restricts potential solar cell coverage making the use of electrical systems that require a great amount of power unlikely [9]. The low thrust and efficiency of a cold gas systems permits the development of a reliable system with a fraction of the cost of other systems. However, the high pressure storage, up to 60 MPa (8702 psi), and the large volume of tanks required to host the propellant might serve as a disadvantage to cold gas propulsion [11]. Typical gases used in cold gas systems include ammonia (NH_3), helium (He), N_2 and xenon (Xe). A cold gas propellant can be stored as a high pressure gas or a two-phase saturated liquid.

Early forms of orbital satellite propulsion were mostly cold gas systems [11]. Surrey Satellite Technology Ltd., SSTL, a spin-off company of the University of Surrey in the United Kingdom, is a leader in small satellites and small satellite propulsion. Their Surrey Nanosatellite Application Program (SNAP-1) spacecraft (Figure 1.5 taken from [12]) had a mass of 6.5 kg and utilized a cold gas propulsion system. The micro-propulsion system (MPS) of SNAP-1 had a maximum thrust of 0.001 N at chamber pressure of 400 kPa capable of 3 m/s ΔV. The 32.6 grams of propellant, butane, were stored in a triangular-shaped titanium tube measuring 1.1 m in length with a volume of 65 cm^3 [12]. The size limitations of the spacecraft dictated the use of the titanium tubing to reduce the cost and time associated with developing a custom tank for the mission [9].

The European Space agency, ESA, PROBA-2 satellite (Figure 1.6 taken from [13]) is among the smallest ever to be flown by the agency. Launched at the end of 2009, the satellite weighed only 130 kg [13]. PROBA-2 was set to explore the effects of the active Sun on the near Earth environment [13]. PROBA-2 objectives can be divided into two main experiments: solar observation experiments and space weather experiments, which include measuring electron density and temperature in the background plasma of the Earth's magnetosphere [13]. The spacecraft's low-cost propulsion system was developed by SSTL and it utilized either xenon or nitrogen as propellants. It had a dry mass of 6.72 kg and a

Figure 1.5 SSTL SNAP-1 Spacecraft

propellant mass of 500 g for xenon, and 176 grams for nitrogen. The system is capable of providing thrust values between 20-50 mN and specific impulses between 40-100 seconds. Electrical power could be utilized to warm up the gas and increase the specific impulse of the system [14].

ESA also designed the CryoSat-2 spacecraft (Figure 1.7 taken from [15]) as an effort to monitor and measure the thickness of floating sea ice. CryoSat-2 mission is to observe annual variations and survey the surface of ice sheets very accurately to detect the smallest of changes [15]. CryoSat-2 was a follow up spacecraft to CryoSat-1, which was lost when the launch vehicle encountered an unexpected problem in the second stage causing a failure in separation [11]. CryoSat-2 was launched to low Earth orbit in April, 2010 weighing 720 kg, including 37 kg of gaseous nitrogen propellant mass stored at 278.6 kPa in a high pressure tank [16]. The spacecraft cold gas system utilized sixteen 10 mN attitude control thrusters to ensure minimum correction due to gravity-gradient disturbances, and four 40 mN orbital control thruster.

Figure 1.6 ESA Proba 2 Satellite

As of April, 2016, CryoSat-2 remains in orbit and has surpassed its mission design life of 3.5 years. It has enough fuel to remain in orbit and sustain itself into the early 2020s, if it doesn't suffer any major component damage or failure [16].

Cold gas systems have been used in small and larger satellites and have proven to be very reliable when simplicity, low-cost, and safety are desired.

1.4. MISSOURI UNIVERSITY OF SCIENCE AND TECHNOLOGY SATELLITE RESEARCH TEAM (M-SAT)

The Missouri University of Science and Technology Research Satellite Team (M-SAT) works with faculty and industry mentors to design, construct, and launch small satellites. M-SAT was one of ten university satellite teams invited to participate in the UNP Nanosat-8 (NS8) competition that concluded in January, 2015 [17]. The team's

Figure 1.7 ESA CryoSat-2 Spacecraft

spacecraft was awarded first place among ten competing teams at the final competition review. UNP, University Nanosat Program, started in January of 1999 as a collaboration between the Defense Advanced Research Projects Agency (DARPA), the Air Force Research Laboratory (AFRL) Space Vehicle Directorate (RV), the U.S. Air force Office of Scientific Research (AFSOR), NASA Goddard Space Flight Center, and the American Institute of Aeronautics and Astronautics (AIAA), and nine universities [18]. UNP's mission is to promote satellite development, education and knowledge for students in university-based satellite teams. Recently, UNP became a collaboration between AFRL/RV, AFSOR, and AIAA [18]. UNP strives to support development and sustainment of space science research at the university level with large emphasis on research and development of small satellites through a practical application of fabrication, integration, and testing [18] [19].

UNP oversees a two-year cyclic competition program associated with reviewing the developments and progress of the involved teams over the span of the two years and at the end of each cycle the teams are required to present an Engineering Design Unit (EDU) [18]. The winner of the competition will have the chance to secure a launch opportunity through the Department of Defense (DoD) Space Test Program (STP) after successful review from DoD Space Experiments Review Board (SERB) [11].

M-SAT is currently working on two main projects. The first project consists of two microsatellites, MR SAT (Missouri-Rolla Satellite) and MRS SAT (Missouri-Rolla Second Satellite). The pair is launched together, and MR SAT will act as inspector satellite while MRS SAT will simulate an uncooperative resident space object (RSO). The MR/MRS SAT project goal is testing new technologies in support of missions involving proximity operations [17]. A stereoscoping imager sensor is used to determine the real-time relative distance and velocity vectors between the MR and MRS SAT [17]. Furthermore, the project involves the study of an R-134a cold gas propulsion system for use in formation flying applications. The pair is designed to advance studies and knowledge of distributed space systems (DSS) missions. The use of small satellites in formation can prove to be very beneficial. Small spacecraft formation flying might have the ability to match and perhaps outperform mission objectives of larger spacecraft with reduced cost, complexity and failure [11].

The second project M-SAT is working on is Cube Quest. Cube Quest is a part of NASA's Centennial Challenge Program. The goal of this challenge is designing, constructing, and launching a cubesat [17]. The cubesat, Lunar CubeQuestador (LCQ), participated in NASA's Lunar Derby Competition, where the goal of the spacecraft mission was to orbit the Moon [17]. As a part of UNP's Nanosat-9 competition, M-SAT and LCQ teams are also working with the Aerospace Plasma Laboratory (APLab) at Missouri University of Science and Technology (Missouri ST) to test the APLab's multi-mode microtube-electrospray propulsion system that can operate as low-thrust high-specific impulse electrical or high-thrust low-specific impulse chemical propulsion system and combines a catalytic chemical microtube propulsion system with an electric electrospray propulsion system [20]. M-SAT's Nanosat-9 CubeSat mission will be enhanced with NASA's Undergraduate Student Instrument Project (USIP). USIP is an Educational Flight Opportunity (EFO) that solicits universities for proposals to design and develop a 3U CubeSat that will fly in low Earth orbit (LEO). The goal of USIP is to promote interest and proficiency in Science, Technology, Engineering and Mathematics (STEM) Education. USIP and Nanosat-9 help develop and enhance the scientific and technical skills for a university-based satellite team by providing hands-on flight project development experience.

1.5. PURPOSE AND MOTIVATION

The development of a low cost, reliable, and safe cold gas propulsion system has been a goal for the Missouri University of Science and Technology Research Team (M-SAT) since its inception. In any cold gas propulsion system the propellant is accelerated and exhausted through a nozzle. The nozzle allows for the extraction of the fluid dynamic properties of the propellant to produce the desired flow characteristics. A well-designed nozzle will ensure that the propulsion system functions efficiently and accordingly. However, after the performance of the propulsion system of MR SAT was reviewed and analyzed, it was apparent that the fidelity of the analysis of the originally designed nozzle needed improvement. The flow of the nozzle did not choke and did not fully expand resulting in significant performance losses. Furthermore, with the M-SAT taking on new challenges such as the AFRL NS-9 competition and NASA's USIP CubeSat program and the need for a new and improved nozzle to ensure that the propulsion system performs its required tasks allowing for a successful mission became very evident.

This thesis study explores the design, simulation and analysis through methods of computational fluid dynamics (CFD) of a new micro-nozzle concept that can be integrated with MR SAT or even a CubeSat to enhance the performance of the propulsion system. This study could serve as a resource for universities developing a low-pressure cold gas refrigerant propulsion system for use on micro, nano, and cube satellites. The proposed design could include spatial and volume savings and improved performance characteristics.

1.6. THESIS ORGANIZATION

The introductory section of this thesis is followed by five other sections, which are described below:

1. LITERATURE REVIEW - A review of common nozzle configurations and a breakdown of their advantages and disadvantages. A discussion of aerospike nozzles use is included in this section as well. Further, a summarized description of the previous work and research done on the MR-SAT and LCQ propulsion systems.
2. PROPELLANT SELECTION AND NOZZLE DESIGN - A discussion of the propellant selection criteria and selected propellants is outlined in this section. A breakdown of the methodology and procedures used to design the contour and the three-dimensional model of the supersonic micro-nozzle is provided.
3. NOZZLE CFD PERFORMANCE ANALYSIS - A detailed explanation of the CFD method used to determine the nozzle performance and characteristics. A procedure to design, analyze and interpret the result of the CFD simulations is given.
4. RECOMMENDATIONS AND FUTURE WORK - Suggestions and recommendations based on the obtained results of the analysis are made in this section. A

discussion of possible future work that extends beyond the scope of this thesis is presented.

5. CONCLUSIONS - A review of the results found during the course of this research and concluding remarks regarding the findings of the presented analysis. Possible benefits to a university-based satellite teams are discussed in this section.

2. LITERATURE REVIEW

2.1. ROCKET NOZZLES

In this section the primary functions of nozzles are discussed and common nozzle geometries reviewed.

Generally, the primary function of a rocket nozzle in most propulsion systems is to convert the chemical-thermal energy of the combustion process into kinetic energy; this is done by accelerating slow moving, high pressure, high temperature gas in the combustion chamber into a high velocity gas of lower pressure and temperature. Similarly, in any cold gas propulsion system the propellant is accelerated and exhausted through a nozzle. The nozzle allows for the extraction of the fluid-dynamic properties of the fluid to produce the desired thrust. The produced thrust is in fact a product of the velocity and mass of the fluid, hence a very high velocity is a desirable outcome of any rocket nozzle. Some of the most common nozzle configuration can be seen in Figure 2.1 [8].

The objectives of good nozzle configurations are to achieve the highest practical I_{sp}, minimize inert nozzle mass, and minimize vehicle length. Shorter nozzles have the ability to reduce the overall length and mass of the vehicle. Nozzle geometries used to accelerate the propellant gas and achieve the desirable thrust values can be divided into two main types: convergent-divergent nozzles and nozzles with aerodynamic boundaries.

2.1.1. Convergent-Divergent Nozzles. Convergent-Divergent nozzles, C-D nozzles, is a widely used term that refers to a number of physical-boundary nozzle configurations, most famously it refers to conical and bell nozzles. Convergent-divergent nozzles, in all their configurations, are the most commonly used nozzles. These nozzles will usually have a circular cross-section converging section, a throat, and a circular cross-section

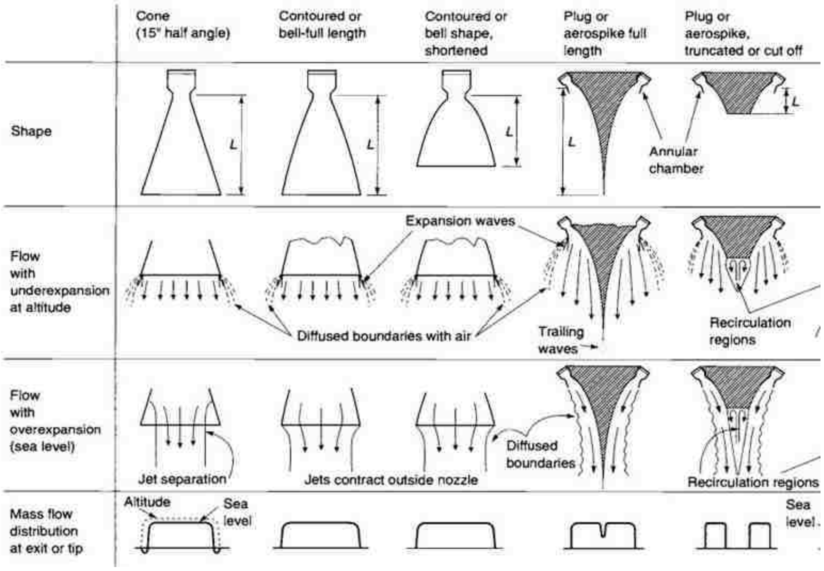

Figure 2.1 Various Nozzle Configurations and their Flow [8]

diverging section. The subsonic flow in the convergent section of a C-D nozzle can be easily turned at very low pressure drops and at any radius, cone angle, wall contour or curve, or nozzle inlet shape. Hence the converging section is not critical in achieving high performance and the flow is not highly dependable on it [8]. In fact, some small attitude control thrust chambers have had their nozzle at 90° from the combustion chamber axis without any performance losses [8]. Furthermore, the nozzle throat contour is not critical to the nozzle performance and any radius or curve is usually acceptable [8] [10]. In the convergent and throat sections of the nozzle, the flow will adhere to the walls due to high pressure gradients. This makes the C-D nozzle configuration dependant on the diverging section of the nozzle.

C-D nozzles are frequently refereed to as de Laval nozzles. The terminology comes from the fact that in the late 1800s a Swedish engineer by the name of Carl G. P. de

Laval designed a steam turbine which utilized supersonic expansion nozzles upstream of the turbine blades. This innovative turbine design by de Laval sparked a huge interest in the fluid mechanics of flow through such nozzles at the turn of the twentieth century [21]

2.1.1.1. Conical nozzles. A conical nozzle is a cone shaped nozzle that is described by the cone's half angle (β) measured from the centerline of the divergent section of the nozzle to the nozzle wall. Conical nozzles are the oldest and simplest nozzle configurations. A theoretical correction factor, κ, for a conical rocket nozzle can be applied to the exit momentum of the ideal rocket (discussed in 3.2). The parameter κ can be described as the ratio between the momentum of the gases in a nozzle with a finite nozzle angle, 2β, and the momentum of an ideal nozzle with all gases flowing in an axial direction [8] as

$$\kappa = \frac{1}{2}(1 + cos(\beta)) \tag{2.1}$$

For ideal rockets $\kappa = 1$, and for a nozzle with divergence cone angle of 30^o ($\beta = 15$), which is usually referred to as the reference case, $\kappa = 0.983$. This indicates that the exit momentum and exhaust velocity will be 98.3% of the ideal exhaust velocity [8]. The correction factor for different α values for any nozzle that has uniform mass flow per unit exit area can be found in [8].

Conical nozzles are the oldest and simplest nozzles. They have been used for a long time with asginifcant body of historical data associated with them. Conical nozzles are relatively easy to fabricate and manufacture. Major disadvantages of conical nozzles include the trade-off between divergence angle and nozzle length, which affects the mass of the propulsion system. A large divergence angle allows for a short, lightweight nozzle but with low performance. A small divergence angle results in increased axial momentum and gives high specific impulse, but also results in a longer nozzle which imposes a penalty on propulsion system mass, overall vehicle mass, and adds to the design complexity of the nozzle [8].

Conical nozzles are not as popular as they once were. The use of shortened bell nozzles allow for similar performance characteristics at shorter nozzle lengths and lighter weights.

2.1.1.2. Bell nozzles. The gas expansion process in a bell nozzle is more efficient than in its conical nozzle counterpart of similar expansion ratio (AR) and nozzle length. This is due to the fact that the wall contour of a bell nozzle is designed to minimize losses. The design of the wall contour of a bell nozzle can be achieved using the method of characteristics [21]. The terms "bell" and "contoured" nozzle are used interchangeably. The higher efficiency of the contoured nozzles makes them the most commonly used nozzle configuration today [8]. Because it is preferred to have a nozzle of shorter length, as the length of a nozzle is a good indicator of its weight, it is desirable to obtain a nozzle of limited length without a compromise on thrust and performance. This can be done by introducing characteristic surfaces as control surfaces of momentum, mass flow, and the length of the nozzle [22]. This allows for the reduction of the governing differential equations of the gas flow to one ordinary differential equation [22]. A method for designing a contoured nozzle for optimum thrust is outlined in [22].

A bell nozzle will usually have a high expansion angle section downstream of the nozzle throat (up to 50°). This very high expansion is followed by a gradual reversal of nozzle contour slope resulting in a smaller divergence angle at the nozzle exit (usually less than 10°) [8]. The length of a bell nozzle is usually given as a fraction of the length of the reference conical nozzle, Figure 2.2 (taken from [8]). As seen in Figure 2.2, an 80% bell nozzle configuration that has the same area ratio (AR) as 15° half angle conical nozzle will be 20% shorter in length.

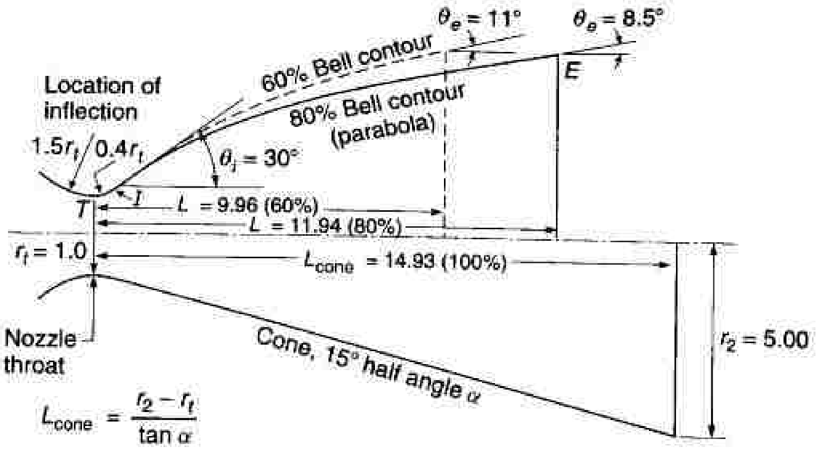

Figure 2.2 Comparison of a 15 Degree Conical Nozzle (Reference Nozzle) with 80% and 60% Bell Nozzles, all at an Area Ratio (AR) of 25 [8]

Bell nozzles were famously used the in Space Shuttle Main Engine, SSME, RS-25, developed by Aerojet Rocketdyne. C-D bell nozzles have also been used in multiple launch vehicles such as the Atlas V. More recently, they have been used on Merlin engines, Figure 2.3 [23], which powers Space Exploration Technologies' (SpaceX) Falcon 9 reusable launch vehicles [23].

C-D nozzles have been the dominant nozzles in the aerospace industry due to their many advantages including relative simplicity, the availability of experimental data, and ease

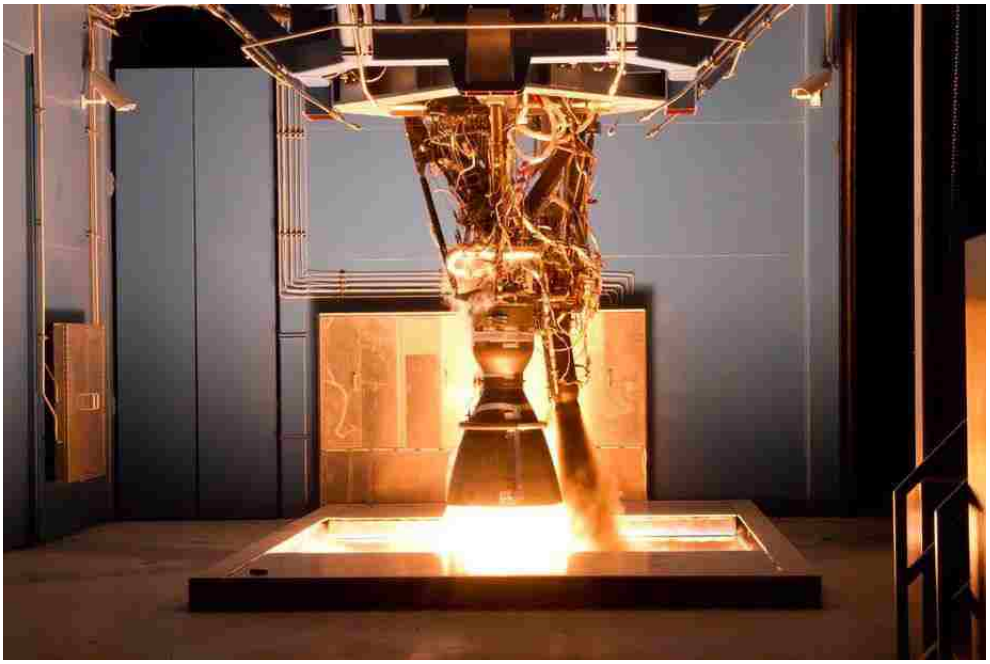

Figure 2.3 SpaceX’s Merlin Engine Being Tested in Texas [23]

of manufacturing. However, poor performance is encountered when macroscale designs are scaled down for micropropulsion systems.

2.1.2. Aerospike Nozzles. The term "plug nozzle" can be used to refer to the full-spike configuration of the nozzle. "Aerospike" usually refers to the truncated nozzle because of the flow circulating in the lower pressure base region forming an aerodynamic spike with the base flow [24]. "Spike nozzle," similar to plug nozzle, usually refers to the full physical spike configuration. In the scope of this thesis, plug, aerospike, and spike will refer to the full configuration with the physical spike unless stated otherwise.

Plug nozzles were developed as an attempt to compensate for the loss of thrust originating from altitude change of a rocket. These nozzles allow for near optimum expansion at all altitudes. The optimum expansion is achieved by having an aerodynamic boundary, ambient conditions, to the flow of the nozzle. The expanding gas in a plug nozzle will flow radially through an annular throat. The expanding flow is exposed to the ambient pressure and the expansion of the flow becomes dependent on the ambient conditions in the diverging section rather than a physical boundary [24] [10]. A plug nozzle has an annular shaped throat with an annular nozzle slot. The outside aerodynamic boundary of the gas flow in the divergent section of the nozzle is the actual interface between the expanding gas and the ambient pressure. The flow expands on the central spike of the nozzle as well. As the vehicle ascends in flight, the aerodynamic boundary expands outward causing a change in pressure distribution on the central spike and allows for a continuous and automatic altitude compensation [8]. A plug nozzle can be visualized as a bell nozzle turned inside out and the solid wall is the surface area upon which the axial component of the wall pressure acts to generate thrust [24]. Furthermore, the mass flow per unit area is relatively uniform over the exit cross section and the divergence losses are minimum [8].

Rocket engines with plug nozzles have been developed and ground tested. Multiple tests with pressurized feed systems and trubopump feed systems have been successful [8]. However, as of today, none of these rocket engines with aerodynamic nozzle boundaries have flown in a production vehicle due to the lack of significant research, test, and flight data available on them [8].

Plug nozzles can be truncated to save weight with minimal effects on the performance of the nozzle. The effects of central plug cut-off can be offset by injecting a small amount of gas flow through the base plate of the plug. This enhances the back pressure on the base. Truncated nozzles have the advantage of being shorter than a full spike nozzles resulting in lower vehicle mass and ease of integration in some cases, full altitude compensation, and no flow separation from wall at lower altitudes [8].

Plug nozzles are not a new concept. The research in the topic started back in the 1950s. However, static fire tests did not take place until the the 1960s. The use of plug nozzles was actually considered for the use on the Space Shuttle Main Engine (SSME) but the lack of sufficient flight data associated with plug nozzles deemed the technology too risky. As a part of the X-33 program NASA and Lockheed Martin invested in plug nozzle technology for Single-Stage-to-Orbit (SSTO) reusable launch vehicles (RLVs) [25]. This was done as an effort by NASA to tackle the challenge of developing an efficient, lightweight, powerful, and low-cost propulsion system with short turnaround time [25].

Even though the project was canceled in 2001, NASA engineers at Marshall Space Flight Center have conducted three hydrogen-cooled thruster tests on the aerospike engine [25]. A 5% scale model of the X-33 aerospike engine was tested in a wind tunnel at the Air Force's Arnold Engineering Development Center [25]. The test was aimed at characterizing the interaction between the aerospike engine and the exhaust. Flight qualification testing began in 1998 at Stennis Space Center [25]. It was not until the year 2000 that NASA engineers first, successfully, operated the aerospike engine at full power and exceeded the expected operating time [25]. The first X-33 aerospike engine completed fifteen successful hot-air fire tests accumulating more than 1,460 seconds of total operating time [25]. Albeit the X-33 aerospike engine was not flown, the research on it lead to significant advancements in the field and contributed to the credibility of the technology.

As a part of the California Launch Vehicle Initiative (CALVEIN), California State University, Long Beach and Gravey Spacecraft Corporation have successfully conducted a static fire test of a 1000-lbf annular plug nozzle rocket engine in the Mojave desert [26]. The engine was designed for the Prospector-2 and 3 rockets. The pressure-fed system uses LOX and ethanol as propellants [26]. During testing, the tank pressure was set to 390 psi and the chamber pressure was set to 300 psi to meet the design requirement of 90 psi pressure drop [26]. During the test the plug nozzle failed structurally resulting in an explosion of the engine, after running for 200 ms. The engine was able to approximately provide an I_{SP} of 235 seconds [26].

Firefly, a new space launch company specifically tailored for small satellites, are utilizing a truncated plug nozzle for their Firefly α launch vehicle [27]. The first stage engine of the Firefly Alpha, FRE-2, features a number of small combuster nozzles arranged in a circular pattern around a central plug. The system is capable of providing 99,600 lb of thrust with an I_{sp} of around 299 seconds [27]. Their first demonstration of CubeSat launch is set for early 2018.

There have been a couple of efforts to design a plug nozzle engine for satellite and rocket propulsion use. However, most of the efforts did not go further than analytical and computational analysis of the problem due to some disadvantages of the plug nozzle. One major disadvantage that plug nozzles face is active cooling of the central plug. Due to the small throat area of the plug nozzle when monopropellants and bipropellants are used the expanding gas coming from the combustion chamber might cause the central plug to overheat and fail. The central plug of a spike nozzle being heated to values higher than material limitations meant that a secondary cooling system had to be installed to cool the plug and prevent failure. Overcoming this problem using secondary active cooling systems greatly affects the vehicle mass. This is one of the major reasons why plug nozzles are often overlooked.

Utah State Univeristy (USU) was able to develop and test a hybrid propulsion unit that utilizes a small-scale plug nozzle for nano and CubeSats [28]. The Multiple Use Plug Hybrid for Nanosats (MUPHyN) uses a non-toxic and safe N_2O and ABS grain as green system propellants [28]. The plug also offers a non-mechanical thrust vectoring secondary fluid injection, which is used to control attitude during burns [28]. However, the

MUPHyN prototype was not mission optimized nor intended to provide high accuracy heat flux measurements. The plug is cooled by nitrous oxide using a secondary cooling system [28]. The testing demonstrated that the aerospike temperature stayed within material limits. Furthermore, the I_{SP} ranged between 106 and 144 seconds and thrust values eight times larger than desirable for CubeSats [28]. This is simply due to the fact that plug nozzles allow higher expansion ratios in significantly smaller volumes.

2.2. PREVIOUS WORK

2.2.1. M-SAT Propulsion System. This section provides a review of the previous research and analysis of the propulsion system in development of MR SAT conducted by [11] and the M-SAT team. More detailed information about the design and analysis of the MR SAT propulsion system can be found in the original source [11]

With mission objectives to study close formation flight, MR SAT requires a propulsion system capable of providing small orbital maneuvers with the ability to arrest launch vehicle ejection tumble (tip-off) and fine tune three-axis attitude corrections. Along with meeting the overall mission requirements, performing efficiently, and being financially feasible, the propulsion system must fulfill system and safety requirements set by UNP. The satellite pair will be equipped with attitude determination hardware as well as magnetic coils as primary attitude control devices. However, only the larger satellite, MR SAT, will be integrated with a propulsion system. During formation flight it is necessary for MR SAT to follow the orbit of MRS SAT using the propulsion system to maintain a distance of 10 m within 1 m of tolerance. The main use of a propulsion system is to provide the spacecraft with means to maneuver through space by changing the spacecraft's orbit shape and size. The secondary use of the propulsion system is to provide means for attitude control. Previously conducted research [11] and [9] concluded that a cold gas thruster system with two-phase propellant, saturated liquid R-134a, was the most feasible. Due to design limitations specified by Nanosat-4 through 8 competitions, the use of R-134a required in-depth analysis and testing prior to being accepted by AFRL.

Analysis of performance characteristics of the R-134a propellant system concluded that it is a very capable system for the M-SAT mission. The system is currently undergoing testing to ensure full functionality and safety in the designed condition. Due to safety constraints placed on the M-SAT mission by the UNP User's Guide, physical inhibits must be installed to minimize the risk of leaking propellant that might possibly damage the primary payload on the launch vehicle. To avoid this, three solenoid isolation valves are implemented to isolate propellant from the thrusters and the regulator. A regulator is used such that the high tank pressure (around 100 psia) is regulated to the desired pressure at each thruster nozzle. The R-134a propellant is designed to be distributed to each of the 12 electronically operated thruster solenoids. The outline of the propulsion system along with the 12 thrusters is shown in Figure 2.4, and the complete propulsion system can be seen in Figure 2.5. The complete propulsion system includes the propellant tank, three isolation valves, battery boxes, pressure transducers, and the propulsion bridge.

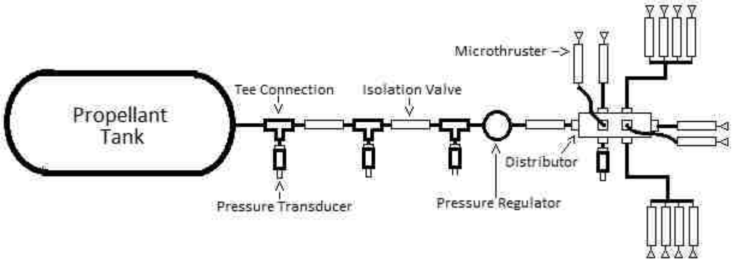

Figure 2.4 MR SAT Cold-Gas Propulsion System Configuration

The isolation valves and the thrusters will be controlled by the propulsion circuit board designed by the M-SAT team. The board will receive commands determined by the proximity operations guidance, navigation and control system. The four pressure transducers are used to ensure that the system is operating correctly during flight. The housing structures for the batteries MR SAT will use in flight are placed surrounding the propulsion tank. This design choice to house the batteries near the tank was made such that the waste heat from charging and discharging the batteries will be transferred to the propellant tank, which will help change the phase of the R-134a propellant from liquid to gas as it is exits the propellant tanks.

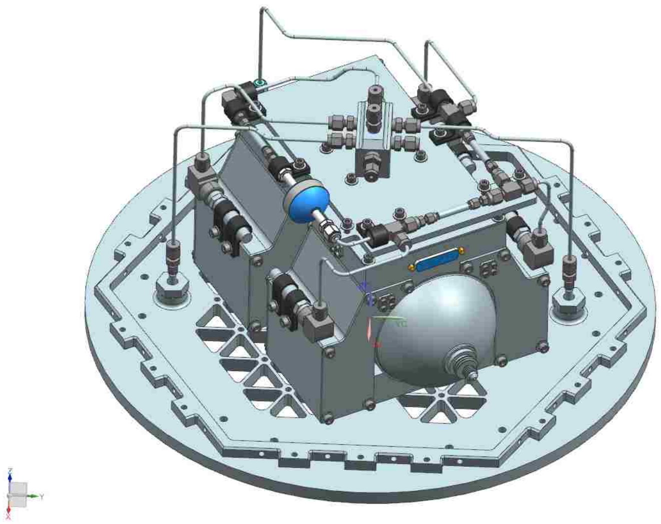

Figure 2.5 MR SAT Complete Propulsion System (Individual Thrusters and Propellant Lines not Shown)

2.2.1.1. Previous nozzle analysis and design. The original nozzle design was specifically tailored to the requirements of the MR SAT propulsion system. A tank volume of 2.5 L was chosen and the temperature range was defined to be between −50° C to 100° C. In a closed volume system like a propellant tank, the highest pressure of fluid will occur at the peak temperature. The maximum thermodynamic proprieties at this peak temperature of 100° C (212° F) were determined. The Maximum Design Pressure (MDP) was set at sealed container limitations with an absolute pressure value of 689.48 kPa (100 psia). The internal energy of the system, along with the density and maximum propellant mass were calculated at this determined maximum temperature and pressure. The maximum mass of R-134a that can be stored in the propellant tank was determined to be 60.523 grams. Using the previously mentioned propellant mass, along with design operating condition of 20° C and regulated absolute pressure of 137.95 kPa (20 psia) at each thruster, nozzle design analyses were conducted. The 20° C operating temperature was assumed because it is an approximate mean temperature that can be anticipated by a small spacecraft in LEO. The 137.95 kPa (20 psia) pressure limit is set by the propulsion system's pressure regulator.

In order to synthesize an accurate design for the nozzle it was necessary to take into consideration the structural integration of the thrusters. In order to ensure easy integration of the nozzle/valve assembly, the outer diameter of the nozzle structure was limited to 6 mm to match the the valve diameter of 6.35 mm. The inner nozzle exit diameter was set to 5 mm allowing a 0.5 mm wall thickness for structural rigidity, which constrained the exit area (A_e) of the nozzle for flow calculations.

The total mass of the satellite to be maneuvered by the thruster was estimated to be 25 kg. The specific heat ratio of the propellant was determined using Engineering Equation Solver (EES) at the previously mentioned operating conditions. Table 2.1 summarizes the discussed analysis parameters used for the MR SAT original nozzle design.

Table 2.1 Parameters of MR SAT Supersonic Micronozzle Design

Propellant Mass	m_p	60.52 grams
Nozzle Inlet Temperature	T_c	20 C (68 F)
Absolute Nozzle Inlet Pressure	P_c	137.9 kPa (20 psia)
Specific Heat Ratio	γ	1.127
Nozzle exit diameter	D_e	$5\text{x}10^{-3}$ m
Nozzle Exit Area	A_e	$1.9635\text{x}10^{-5}\ m^2$
Spacecraft Estimate Mass	m_o	25 kg

Once the dimensional and thermodynamic constraints were determined the remaining parameters needed for the nozzle design were the area expansion ratio ($\mathrm{AR} = \mathrm{A_e}/\mathrm{A}^*$), the throat area ($\mathrm{A}^*$) and diameter ($D_t$). The total ΔV of the propulsion system is the driver to meet the requirements of the propulsion system. The $\mathrm{I_{sp}}$ and ΔV of the system are functions of inlet temperature, specific heat ratio of the gas (γ), and the nozzle pressure ratio ($\mathrm{PR} = \mathrm{P_e}/\mathrm{P_c}$). P_e is defined as the fluid pressure at the exit of the nozzle, and P_c is defined as the absolute pressure at the inlet of the nozzle. PR was numerically calculated from the area ratio, AR. The relationship between AR and PR is given by

$$AR = \frac{A_e}{A^*} = \sqrt{\frac{\left(\frac{\gamma-1}{2}\right)\left(\frac{2}{\gamma+1}\right)^{\frac{\gamma+1}{\gamma-1}}}{PR^{\left(\frac{2}{\gamma}\right)}\left[1 - PR^{\frac{\gamma-1}{\gamma}}\right]}} \tag{2.2}$$

Further details on the governing equations and calculations are given in [11]. ΔV and $\mathrm{I_{sp}}$ were produced and plotted over a range of AR as shown in Figure 2.6. As can be seen both $\mathrm{I_{sp}}$ and ΔV exhibit asymptotic behavior that approaches a limit as the value of AR increases. This behavior exhibited by $\mathrm{I_{sp}}$ and ΔV is due to the fact that PR approaches zero as AR increases. Recall that, $\mathrm{I_{sp}}$ and ΔV are functions of only PR which was, as previously mentioned, calculated from AR. It is typically beneficial to have a higher AR value in terms of improving ΔV. A high AR value will correspond to a smaller throat area.

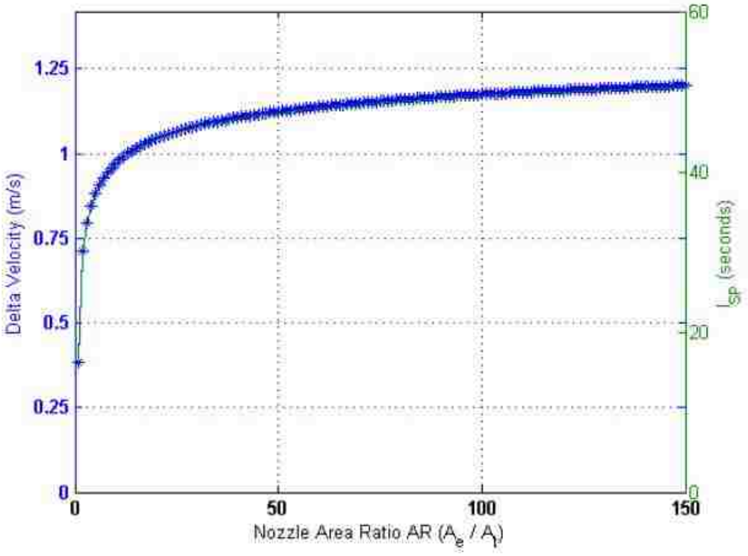

Figure 2.6 MR SAT Nozzle ΔV and I_{sp} for Different AR Values[11]

The chosen throat diameter of 0.5 mm (0.0197 inches) achieves an AR of a 100. The nozzle thrust over a range of AR can be seen in Figure 2.7. The priority of a propulsion system is to maximize ΔV, and thus the duration of the formation flight phase of the satellite. A maximum ΔV can be achieved with a high AR, however the produced thrust, which is critical for attitude control, will be reduced. A compromise was made to meet both requirements, as as well as to meet the geometric considerations of the thruster.

The MR SAT nozzle was manufactured by Micro Aerospace Solutions (MAS) located in Melbourne, Florida. The nozzle exit diameter was set to 5 mm for structural

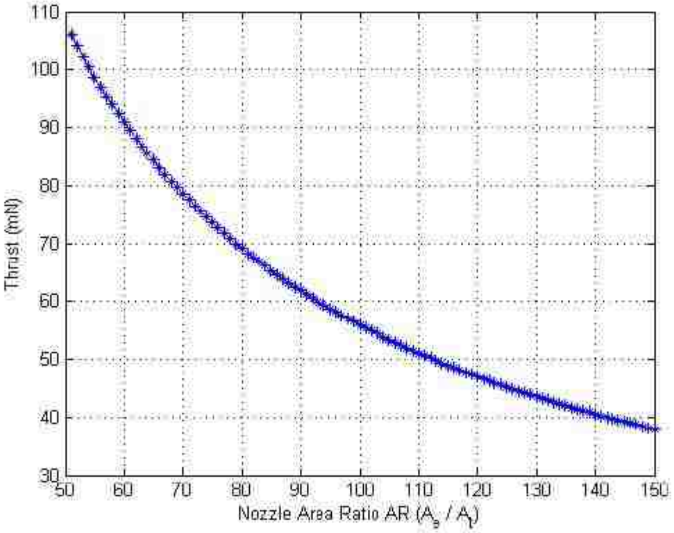

Figure 2.7 MR SAT Nozzle Thrust Production for Different AR Values [11]

integrity and satellite integration reasons. Using an AR of 100, the resulting throat diameter was 0.5 mm. The nozzle was manufactured out of stainless steel. The stainless steel option simplifies connection and integration methods to the stainless steel valves and offers similar thermal expansion. The geometry of the nozzle is show in Figure 2.8. The converging section of the MR SAT nozzle consists of a cone shaped inlet that joins directly to the inlet tubing from the valve. As can be seen in Figure 2.8, a straight sided cone was chosen as the diverging section of the nozzle. The diverging section of the nozzle has a 30° half cone angle which results in a more compact nozzle configuration.

The predicted performance of the MR SAT nozzle can be seen in Table 2.2. The conservative values shown in Table 2.2 are obtained by reducing the propellant temperature to a more conservative 15°C.

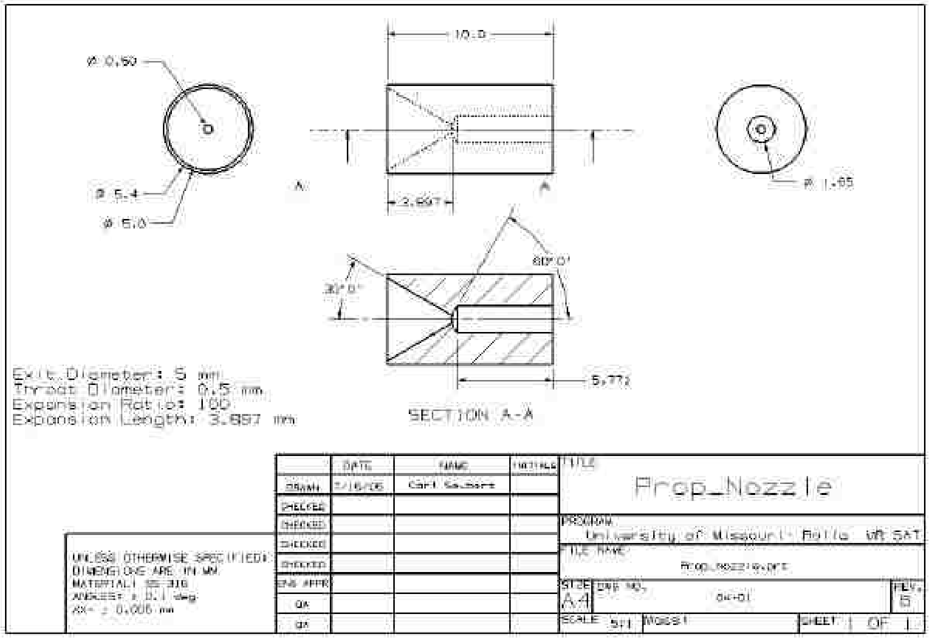

Figure 2.8 MR SAT Nozzle Geometry

Table 2.2 MR SAT Nozzle Theoretical Performance Predictions

	I_{sp} (s)	Thrust (mN)	$\dot{m}$ (g/s)
Ideal	44.09	62.79	0.1481
Conservative	43.71	37.37	0.0889

2.2.1.2. Testing and performance of MR SAT nozzle. This section provides a review of testing and evaluation of the protoype propulsion system of MR SAT conducted by [9] and the M-SAT team. More detailed information about the testing and integration of the MR SAT propulsion system can be found in the original source [9].

The testing setup of the MR SAT propulsion system simulated a similar environment experienced by thrusters in orbit. The goal of the test was to measure the force produced by the thruster using a scale placed inside a vacuum chamber. The test setup schematic can be seen in Figure 2.9. As seen in Figure 2.9, the R-134a tank was submerged in a water bath and the temperature was recorded by a thermocouple. This was done in order to accurately regulate and measure the temperature using ice cubes and a hot plate. The pressure was measured by two pressure transducers placed upstream of the pressure regulator and before the thruster in the vacuum chamber. The pressure transducer upstream of the regulator measured the pressure of the tank, whereas the pressure transducers before the thruster measured the pressure entering the thruster.

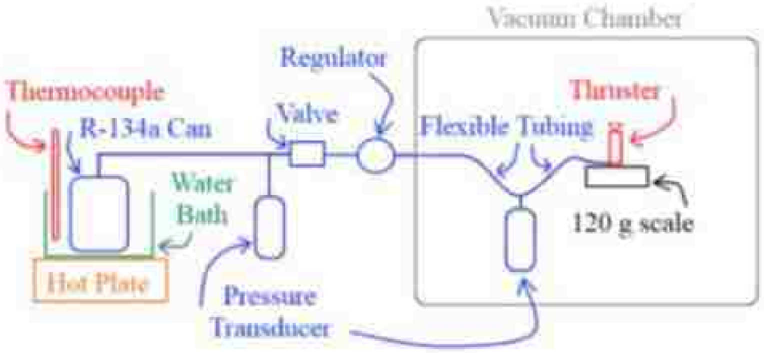

Figure 2.9 Schematic of MR SAT Thrust Testing Setup

The first step of the test was to ensure that all valves were closed, regulators set to zero, and the chamber door was sealed. The test commenced by either heating or cooling the propellant to the target temperature. Once the the target temperature was reached the vacuum chamber was pumped down to around 30 mTorr. The valve on the propellant tank was then opened and the regulator was set to the desired pressure value. Finally, the thruster was fired and the data were collected by a LabVIEW setup.

The testing measured thrust values at various pressure and temperature. The results are presented in Figure 2.10. The actual thrust value was determined to be 24.13 mN, after a few firing tests, instead of the ideal theoretically predicted 62.79 mN. The experimental I_{sp} was around 21 seconds rather than the theoretically predicted 44.09 seconds. More recent testing of the thruster setup conducted by the M-SAT team has estimated the thrust to be around 18.88 mN.

It was evident from the testing results that there is a substantial difference between the theoretical and actual produced thrust and I_{sp} of the thruster. The discrepancy in the results could be due to a number of things. Primarily, the cone-shaped nozzle, even though it meets most of the flight envelope requirements, it is by far not ideal. There are many inefficiencies associated with the coned nozzle configuration. Losses rising from divergent flow lines in a cone shaped nozzle might affect the flow, even with the application of a theoretical correction factor. The micro nozzle geometry itself might be inconsistent due to manufacturing errors. Micro Aerospace Solutions (MAS) was capable of machining to an accuracy of 0.0254 mm (0.001 inches). This means that a 0.5 mm throat diameter could vary anywhere between ±0.0254 mm. This variation in the diameter changes the AR of the nozzle which in turn reduces the accuracy of the theoretical predictions. Increasing the area ratio of the nozzle might give better performance but the tolerances allowed by the manufacturer makes reducing the throat size very challenging and would result in inaccurate dimensions. Changes to the current nozzle might result in a nozzle that exceeds the flight envelope requirements.

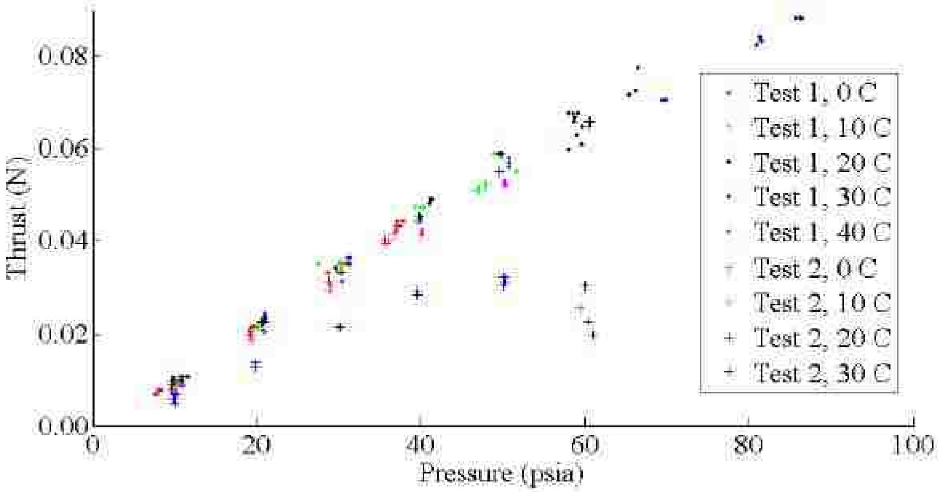

Figure 2.10 MR SAT Thrust Test Data [9]

These results, along with M-SAT taking new challenges such as the Lunar Derby Challenge, led the team to conclude that a new nozzle concept should be pursued and investigated.

2.2.2. CubeSat Propulsion System. The information provided in this section is a summary of the work conducted by the Lunar CubeQuestador (LCQ) team's Propulsion subsystem; all information presented below can be found in [29].

The Lunar CubeQuestador (LCQ) was designed with a similar cold gas propulsion system utilized by MR SAT. This decision was made on the premise that cold-gas propulsion is a well-known research area for the M-SAT team. However, the propulsion system of LCQ is designed to be used to brake into lunar orbit and achieve the goals of the Lunar Derby Challenge. The LCQ propulsion system consists of two fuel tanks, a pressure regulator, two solenoid valves and a nozzle. A diagram integrated propulsion system can be seen in Figure 2.11.

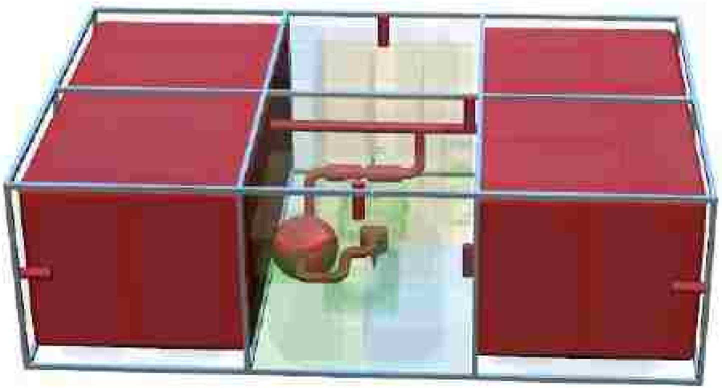

Figure 2.11 CubeSat Integrated Propulsion System

The LCQ fuel tanks were to be be manufactured out of a composite carbon fiber material by Composite Technology Development (CTD), Inc. of Lafayette, Colorado. The two tanks were rectangular in shape. CTD's KIBOKO pressure vessels are composite tanks developed to host gas and liquid for aerospace applications. The custom-made composite tanks have the benefit of being lighter than their metal counterparts, while maintaining microcrack-resistance. The tanks were to be situated at either ends of the the CubeSat for efficient use of space and better mass distribution. The propellant lines leave each tank, converge, and pass through two solenoids that provide redundancy in case of failure. The propellant lines then pass through the pressure regulator. The pressure regulator, as in MR SAT, ensures the consistency of the pressure introduced at the nozzle inlet. The goal of this cold-gas propulsion system is to provide sufficient ΔV capabilities to ensure the CubeSat is successfully inserted into lunar orbit.

The CubeSat utilizes six small pulsed plasma thrusters (PPT). The pulsed plasma thrusters are represented in Figure 2.12 as six small red cylinders. They were positioned on the edge of the satellite for attitude adjustment and reaction wheel desaturation. The PPTs are distributed by MAS and are capable of producing 0.005 N of thrust with an I_{sp} of 150 seconds.

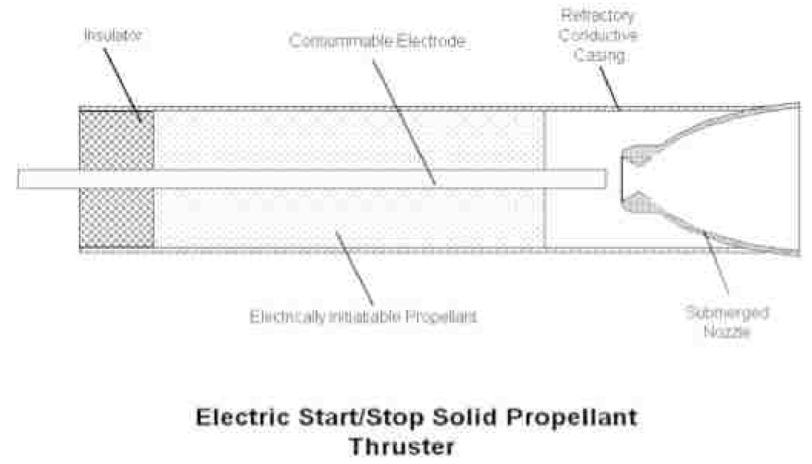

Figure 2.12 MAS Pulsed-Plasma Thruster

The propellant tanks would be subjected to a steady-state temperature of around 30° C, as shown by the Thermal subsystem, at a pressure of 367.3 psi. The Swagelok 6.35 mm (1/4") OD steel tubing will be used as the plumbing of the system. The tubing will then be connected to the matching port of two space-rated Marotta solenoid valves. The pressure regulator was not specified but it will ensure a consistent 24.7 psi pressure at the inlet of the nozzle. However, the regulator will most probably be a Swagelok type regulator because the M-SAT team is familiar with Swagelok regulators due to previous work on MR SAT propulsion system. The propellant is then channeled into the nozzle and expelled to provide thrust to the CubeSat.

2.2.3. Improved Nozzle Design. As this review documented, the previously designed nozzle was not able to achieve the desired performance values, and with M-SAT team taking on new challenges the need for a new and improved nozzle design is crucial in order to provide better performance characterises and ensure the success of the different missions. This thesis describes the procedure and analysis of designing and validating, through the use of computational fluid dynamics (CFD), a nozzle design that meets the requirements of a low-cost cold-gas propulsion system. The design of a new nozzle that increases the area ratio will improve the performance. As P_e approaches zero, PR ($PR = P_e/P_c$) approaches zero as well and AR increases. It is usually beneficial to have a higher AR value in terms of improving ΔV. Having the flow expand at vacuum will allow for chocked flow at the throat of the nozzle and maximum expansion at the exit without further reducing the throat size. Hence, the team decided to pursue a plug nozzle concept. The plug nozzle concept has the potential to preform better than conventional nozzle design and provide optimum performance. The MR SAT conical nozzle had a massive AR of 100 that still was not able to fully expand the flow and caused significant performance losses. The plug nozzle has the advantage of the absence of a physical boundary around the diverging section. This means that the boundary of an aerospike nozzle is the ambient pressure. This phenomenon associated with plug nozzle is what allows the plug nozzle to be more efficient than conventional nozzles at various altitudes. Altitude compensation of the plug nozzle can be used to the advantage of the team to achieve very high expansion.

In vacuum and spaceflight applications, the maximum theoretical performance would be achieved with an ideal nozzle with infinite exit area that would expand the gases to zero pressure thereby attaining the maximum exhaust gas velocity. Because the flow through the nozzle will be limited by the pressure at the inlet of the nozzle and the nozzle throat area, the nozzle increases thrust by increasing gas velocity as much as possible, while taking into account size limitations, as well as weight limitations and operational altitude. Low altitude operation limits the amount of nozzle expansion available because of higher ambient pressure. The absence of pressure in space enables the plug nozzle to achieve this maximum velocity given it will achieve a PR of zero, which will result in an infinite AR value. In vacuum, the absence of ambient pressure to constrain the exhaust plume will cause a huge expansion in the exhausted gas. The turning angle of the exhaust plume can be, approximately, determined by the Prandtl-Meyer expansion wave theory. The plug nozzle design operating at vacuum conditions will guarantee chocked flow and full expansion of the flow. Plug nozzles allow higher expansion ratios in significantly smaller volumes. The cold gas propulsion system eliminates the need of secondary mechanism to cool the central plug of the nozzle, which is a major disadvantage of most plug nozzles used in chemical propulsion.

The plug nozzle design presented in this thesis is tailored for the MR SAT and LCQ cold gas propulsion systems. However, similar analysis and procedure can be carried out for the application of any cold-gas thruster for small spacecraft.

3. NOZZLE DESIGN AND PROPELLANT SELECTION

3.1. CRITERIA FOR PROPELLANT SELECTION

The development of a low-cost, university-based cold gas propulsion system requires the use of a propellant that is safe and easily accessible. The use of a non-toxic, non-flammable propellant allows for safe and easy laboratory handling during design, fabrication, and testing of the system. Using a propellant that is easily obtainable and does not require licensing and permits is important for a university-based satellite team. Furthermore, the propellant must have simple transportation and storage requirements for easy handling by students and team members. The propellant must be compatible with spacecraft materials to ensure the safety of the spacecraft's hardware. Finally, the propellant must be environmentally friendly.

Based on the mentioned criteria, a number of propellant candidates were considered and investigated. Early development of this research focusing on MR SAT considered helium (He), neon (Ne), argon (Ar), xenon (Xe), carbon dioxide (CO_2), and nitrogen (N_2). Furthermore, the refrigerants 1,1,1,2-Tetrafluoroethane (R-134a) and 2,2-Dichloro-1,1,1-trifluoroethane (R-123a) were also considered. However R-123 was later discarded as it is defined as a Class II substance by the Environmental Protection Agency (EPA), whose production and sales do require certification and permits and will become illegal after the year 2015 [11]. Compounds such as butane and other hydrocarbons were not considered because of their flammability, which can be hazardous to students and team members as well as the spacecraft. Another compound that was not considered because of its environmental impact was sulfur hexafluoride (SF_6), even though it is non-toxic, it has a global warming potential that is 23,900 times greater than carbon dioxide [11].

The performed analysis in early development of the cold gas propulsion system presented in [11] suggested that R-134a is the primary choice for the propulsion system. The advantage of using a refrigerant as the propellant is the ability of the refrigerant to be stored as a low-pressure saturated liquid, which requires very low saturation temperature to allow it to be heated to a vapor state. Once the propellant is in vapor state it can be extracted and used as traditional cold gas propellant.

The maximum ΔV for MR SAT achieved by R-134a at sealed container status is 1.11 m/s while maintaining an I_{sp} of 49.9 seconds. R-134a is able to achieve this (relatively) high ΔV due to its high molecular mass and density which results in larger momentum transfer during propulsive pulses. R-134, also, provides lower mass flow rate values and yet offers high exhaust velocity due to its low specific heat ratio (γ) [30].

Based on the knowledge and experience gained from MR SAT propellant selection process, similar criteria were held for the LCQ propulsion system propellant options. Refrigerants such as R-410a, R-22, R-23, R-152a, R-134a, R-170 (ethane), R-290 (propane) and methane were initially considered. After preliminary investigations performed by the propulsion subsystem, the team decided to pursue R-410a refrigerant, with the ability to use R-134a refrigerant as a substitute. R-410 showed marginally better performance values but there are some compatibility concerns that arise when the the refrigerant is used with aluminum. So, the option of R-134a remained a possibility for preliminary design and testing. The option to use R-410a is due to the fact that it has slightly lower density than other propellants allowing the LCQ tanks to host more propellant. The extra propellant is needed to execute and complete all the maneuvers designed for the mission. The spacecraft would have a dry mass of 4.8953 kg and a propellant mass of 4.8777 kg, bringing the total mass of the CubeSat to 9.773 kg. For more information on the propellant selection of the refer to [29].

3.2. LCQ PREFORMANCE ANALYSIS

The preliminary evaluation of the performance of the nozzle assembly with LCQ propulsion system was based on isentropic one-dimensional flow equations and the rocket equation as found in [8], [31], and [21]. The propulsion system of LCQ was designed to have the ability to supply the needed thrust, I_{sp}, and ΔV for the CubeSat to complete the objectives of the Lunar Derby Challenge. The performed fluid dynamic analysis were completed using a MATLAB routine, Appendix C. Thermal analysis was conducted by the Thermal subsystem and determined the total temperature to be 30°C in the tanks. Assuming there are no thermal losses and the tubing of the system is adiabatic, the temperature is considered to be the total temperature throughout the tubing. However, the pressure drop is the primary driver of the system rather than the temperature of the propellant as shown by [11]. The tank's total pressure was varied between 200 psi and 500 psi at 100 psi increments to parametrically determine the best performance values of the LCQ system; the regulated pressure at the inlet of the nozzle was set to 24.7 psi. R-134a and R-410a provided similar results due to their similar γ values.

Engineering Equation Solver (EES) software was used to determine the propellants' specific heat values, C_p, and C_v as well as the corresponding γ (C_p/C_v) value at the specified temperature and pressure. More detailed information on the governing equations are found in [8], [31], and [21].

The area expansion ratio, AR, was defined as

$$AR = \frac{A_e}{A^*} \tag{3.1}$$

The Mach number at the exit is found using the area-Mach relation for isentropic flow given by

$$AR = \frac{1}{M}\left[\frac{2}{\gamma+1}\left[1+\frac{\gamma-1}{2}M^2\right]\right]^{\frac{\gamma+1}{2(\gamma-1)}} \tag{3.2}$$

The static temperature was determined using

$$T = T_o\left[1+\frac{\gamma-1}{2}M^2\right]^{-1} \tag{3.3}$$

where T_o is the total temperature.

The pressure was, similarly, determined using the Mach number and γ

$$P = P_o\left[1+\frac{\gamma-1}{2}M^2\right]^{-\frac{\gamma}{\gamma-1}} \tag{3.4}$$

where P_o is the total pressure.

The velocity of the propellant at the exit of the nozzle was evaluated as

$$u_e = M_e\sqrt{\gamma R T_e} \tag{3.5}$$

The characteristic velocity was given by

$$c^* = \left[\frac{\gamma + 1}{2}\right]^{\frac{\gamma+1}{2(\gamma-1)}} \sqrt{\frac{RT_o}{\gamma}} \tag{3.6}$$

The maximum flow rate at the choke-point of the nozzle was found using

$$\dot{m} = \frac{P_o A^*}{c^*} \tag{3.7}$$

The thrust was given by

$$F = \dot{m} u_e + P_e A_e \tag{3.8}$$

Specific impulse was found using the thrust and the mass flow rate of the propellant

$$I_{sp} = \frac{F}{\dot{m} g_o} \tag{3.9}$$

The effective exhaust velocity was found using I_{sp} and the gravitational acceleration g_o

$$c = I_{sp} g_o \tag{3.10}$$

The total mass of the spacecraft was defined by

$$m_o = m_p + m_d \tag{3.11}$$

in which m_p is the mass of the propellant and m_d is the dry mass of the satellite.

Additionally, ΔV was found using

$$\Delta V = c \ln(MR) \tag{3.12}$$

where MR is equal to the total mass of the spacecraft divided by the spacecraft's dry mass MR = m_o/m_d.

All the variables needed to preform the analysis are presented in Table 3.1. The performed analysis provides a good estimation of the performance of the spacecraft's propulsion system. However, this analysis is based on the area expansion ratio that does not necessarily dictate the expansion of the the flow of an aerospike nozzle in vacuum. The expansion of the flow in an aerospike nozzle operating in vacuum conditions is rather guided by expansion fans and the turning angle is determined by Prandtl-Meyer expansion wave theory [21] [24]. It is expected that the nozzle will perform better and provide higher thrust values due to the very high expansion forced by the absence of ambient pressure conditions. Furthermore, the produced thrust of the plug nozzle will have three different components: the thrust produced by the thruster at the throat of the nozzle, the thrust produced by the plug walls and finally the thrust produced by the base if the nozzle is truncated. The satellite capabilities of the LCQ propulsion system are shown in Table 3.2.

Table 3.1 Improved Micro Nozzle Dimensions

Characteristic	**Dimension**	**Unit**
Molecular Weight	72.58	g/mol
Density	1036.3	kg/m^3
Tank Pressure	2.5326×10^6	Pa
Propellant Mass	4.8777	kg
Ratio of Specific Heats	1.1251	
Regulated Pressure	1.703×10^5	Pa
Tank Temperature	30	°C
Nozzle Exit Area	5.4986×10^{-5}	m^2
Nozzle Throat Area	8.0608×10^{-6}	m^2

Table 3.2 LCQ Satellite Capabilities

I_{sp}	33.4935 (s)
Thrust	2.4734 (N)
ΔV	227.1572 (m/s)
$\dot{m}$	0.0071 (kg/s)

3.3. NOZZLE DESIGN AND METHODOLOGY

This section outlines the methodology and procedures used to design the supersonic plug nozzle and the development of the nozzle contour, as well as the generated 3D SolidWorks model.

3.3.1. Contour Design Methodolgy. There are a number of methods used to define the contour of the plug of an aerospike nozzle. The method used to develop the contour in this thesis study is based on the approximate method outlined by [32]. The approximate design method uses the method of characteristics and characteristic lines to define the contour shape of the nozzle. It is important to note that the method of characteristics uses the inviscid assumption in formulating the governing equations. A detailed explanation of the development of the characteristic lines and the method of characteristics is presented in Appendix B. A sonic flow at the throat of the nozzle is assumed; this sonic flow is expanded using a centered expansion wave originating at the lip of the plug nozzle. With reference to Figure 3.1, the angle the sonic flow direction makes with the axisymmetric line at the start of the external expansion of the nozzle equals the Prandtl-Meyer expansion angle of the centered wave at nozzle lip. The straight, constant-property characteristic line is inclined at an angle of α with respect to the direction of the flow (the geometric x-axis). For detailed information on the approximate method refer to [32]. The method uses the Prandtl-Meyer function to define the expansion waves originating at the lip of the nozzle cowl. The Prandtl-Meyer wave theory anf the derivation of the Prandtl-Meyer function are outlined and presented in Appendix A.

The inclination angle α is given by

$$\alpha = \mu - \nu \tag{3.13}$$

where μ is the Mach angle and ν is the Prandtl-Meyer angle.

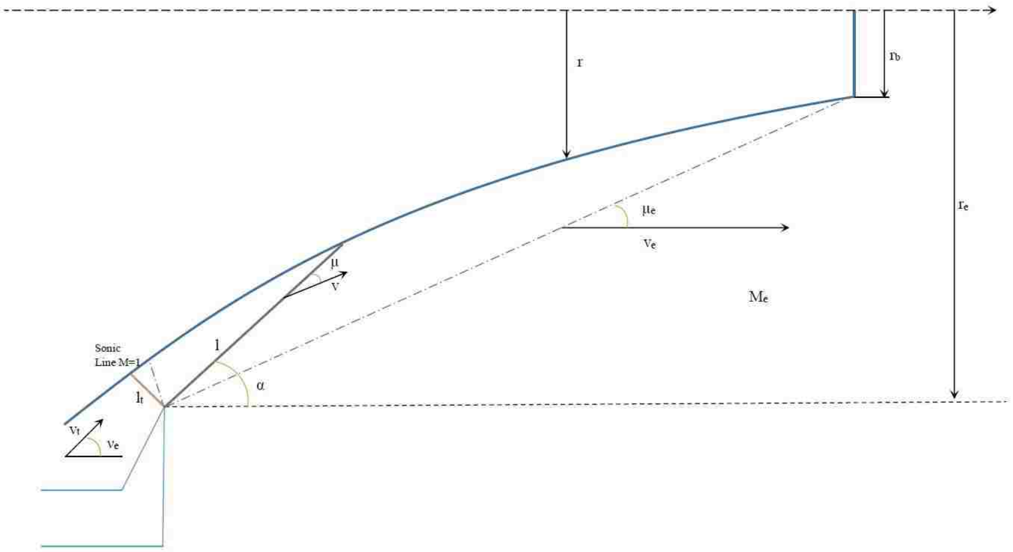

Figure 3.1 Geometry Outlining a Generic Two-Dimensional Annular Plug Nozzle

The expansion fan given by the Prantl-Meyer function is a continuous expansion region composed of an infinite number of Mach waves, bounded by the mach angle, μ. The Mach angle is found using

$$\mu = \arcsin\left(\frac{1}{M}\right) \tag{3.14}$$

The Prandtl-Meyer function, which relates the Prandtl-Meyer angle and the Mach number (M), is given as

$$\nu(M) = \sqrt{\frac{\gamma+1}{\gamma-1}}\tan^{-1}\sqrt{\frac{\gamma-1}{\gamma+1}\left(M^2-1\right)} - \tan^{-1}\sqrt{M^2-1} \tag{3.15}$$

Characteristics lines are particular directions in an xy-space where the flow variables are continuous but along which the derivatives of the flow variables are indeterminate and may even be discontinuous [21]. This conclusion as well as the philosophy and development of the characteristic lines and the method of characteristics are available in Appendix B as previously mentioned.

The characteristic line crosses the nozzle boundary at a distance (l) from the nozzle cowl lip. The distance can be computed by the continuity equation given by

$$\frac{l}{l_t} = \left(\frac{A}{\sin \mu}\right)\left(\frac{1}{A_t}\right) \tag{3.16}$$

where A is the flow passage area normal to the velocity vector (V), and l_t is the distance between the nozzle boundary and cowl lip. Equation 3.16 can be rewritten as

$$\lambda = (AR)M \tag{3.17}$$

in which AR is the nozzle expansion ratio and λ (l/l_t) is the nondimensional length of the characteristic line.

The Mach number is varied at a user specified increment from sonic to a desired mach number at the exit of the nozzle to start the iteration process of the method. A corresponding Prandtl-Meyer angle is calculated for each Mach number, and because the flow direction at the throat is known, the direction of the flow at each iteration can be determined as well and an updated area ratio is calculated using the area-Mach relation given by Equation (3.2). Once the Mach number is determined, the length of the characteristic line can be determined using the isentropic area ratio. Geometry can then be used, as outlined below, to calculate the location of each point on the spike contour for each characteristic line. The fact that each separate point on the plug curve is calculated independently allows the approximate method to have a higher degree of accuracy than the classical methods used to determine the streamlines of a flow-field [32].

With reference to Figure 3.1, the surface that the flow crosses is defined by

$$S = 2\pi \left(\frac{r_e + r}{2}\right)\left(\frac{r_e - r}{\sin\alpha}\right) \tag{3.18}$$

However, the actual passage area is affected by the angle the flow velocity makes with the surface, μ. The actual passage area is given by

$$A = S \sin\mu = \frac{\pi\left({r_e}^2 - r^2\right)}{M \sin\alpha} \tag{3.19}$$

The straight and constant-property characteristic line length from the cowl tip to the surface of the nozzle plug is obtained using

$$l = \frac{r_e - r}{\sin\alpha} \tag{3.20}$$

The exit area of the plug nozzle is given by

$$A_e = \pi \left({r_e}^2 - {r_b}^2 \right) \tag{3.21}$$

For an ideal plug nozzle with a full plug, r_b will be equal to zero and the exit area becomes

$$A_e = \pi ({r_e}^2) \tag{3.22}$$

Now, using Equation (3.19), Equation (3.20) can be rewritten as

$$l = \frac{r_e - \left[{r_e}^2 - \left(\frac{AM \sin \alpha}{\pi} \right) \right]^{1/2}}{\sin \alpha} \tag{3.23}$$

Finally, Equation (3.23) can be nondimensionalized by the exit radius of the spike (r_e) and becomes

$$\xi = \frac{l}{r_e} = \frac{1 - \left[1 - \left[AR_i (1 - {\eta_b}^2) M \frac{\sin \alpha}{AR} \right] \right]}{\sin \alpha} \tag{3.24}$$

where η_b is the nondimensional base radius.

3.3.2. Spike Contours. After the design method was developed and outlined, a MATLAB routine was created to execute the method and design the contour of the actual plug nozzle. The MATLAB code defines the contour of an annular axisymmetric aerospike nozzle based on the mathematical formulation described in Section 3.3.1. and can be found in Appendix C. The generated nondimensional nozzle contour for R-134a can be seen Figure 3.2, and the generated nondimensional nozzle contour for R-410a can be seen in Figure 3.3. The xy-coordinates were nondimensionalized by the exit radius.

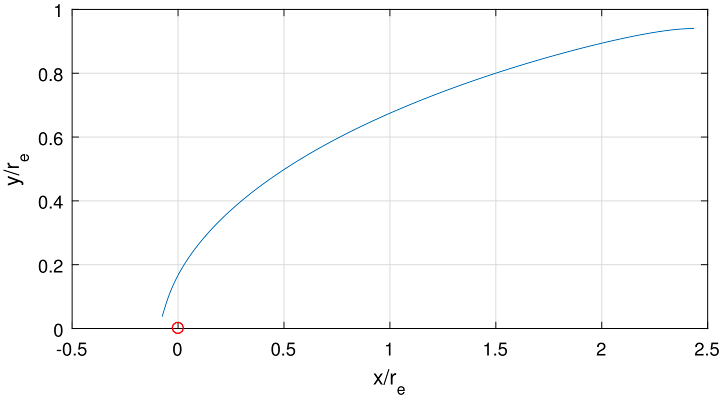

Figure 3.2 Generated Spike Contour for R-134a (γ = 1.127)

The script uses the expansion ratio (AR), ratio of specific heats (γ), and the nondimensional radius at the end of spike (η_b) (which is equal to zero for a full ideal spike) to generate the nozzle contour. The process starts by solving for the Mach number using the Mach-area ratio relationship. In order to improve accuracy and obtain a smoother contour with sufficient data points, the Mach number was equally divided to ten million increments ranging from one to the desired exit Mach number value previously determined by the isentropic one-dimensional analysis. The code then proceeds to use the Mach number values to find the Prandtl-Meyer angles and the Mach angles at each Mach increment. The flow

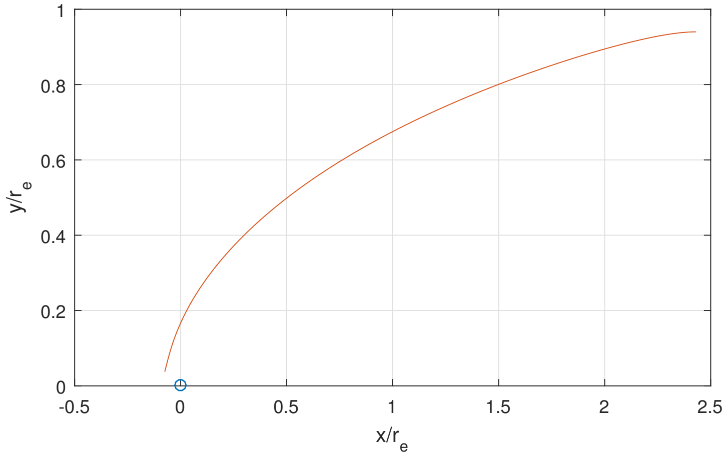

Figure 3.3 Generated Spike Contour for R-410a (γ = 1.125)

direction angle (α) is then found and the characteristic line lengths are determined. Finally, The xy-coordinates of an axisymmetric plug nozzle contour are recorded and plotted. The generated xy-coordinates are revolved around the central axis to obtain a three-dimensional plug nozzle spike.

3.4. SOLIDWORKS MODEL

The generated xy-coordinates were then exported to SolidWorks and a three-dimensional (3D) model of the aerospike nozzle was constructed. An isometric view of the nozzle is shown in Figure 3.4, and a section view of the nozzle can be seen in Figure 3.5. The 3D model of the nozzle shown in Figures 3.4 and 3.5 will be manufactured by an off-campus third party supplier. The plug nozzle will be printed out of stainless steel and will fit over the tubing of the propulsion system. It was critical to match the inlet diameter of the nozzle with the inner diameter of the tubing of the system to ensure exact and precise integration of the thruster setup. The dimensions of the nozzle can be seen in Table 3.3.

Table 3.3 Improved Micro Nozzle Dimensions

Characteristic	**Dimension**	Unit
Total Length	29.718	mm
Inlet Diamaeter	4.572	mm
Exit Area	54.986	mm^2
Throat Area	8.0608	mm^2
Area Ratio	6.8214	
Total Packaged Volume	2.1303	mm^3

This compact plug nozzle design, unlike a conventional C-D nozzle, would be practical and would meet the restriction of the the Poly Picosatellite Orbital Deployer (P-POD) dispenser on the Space Launch System (SLS). A conventional C-D bell nozzle will be far too long and would have been impractical to host within the P-POD restrictions. A draft of the dimensions of the nozzle is shown in Figure 3.6.

Figure 3.4 Aerospike Nozzle Isometric View

Figure 3.5 Aerospike Nozzle Section View

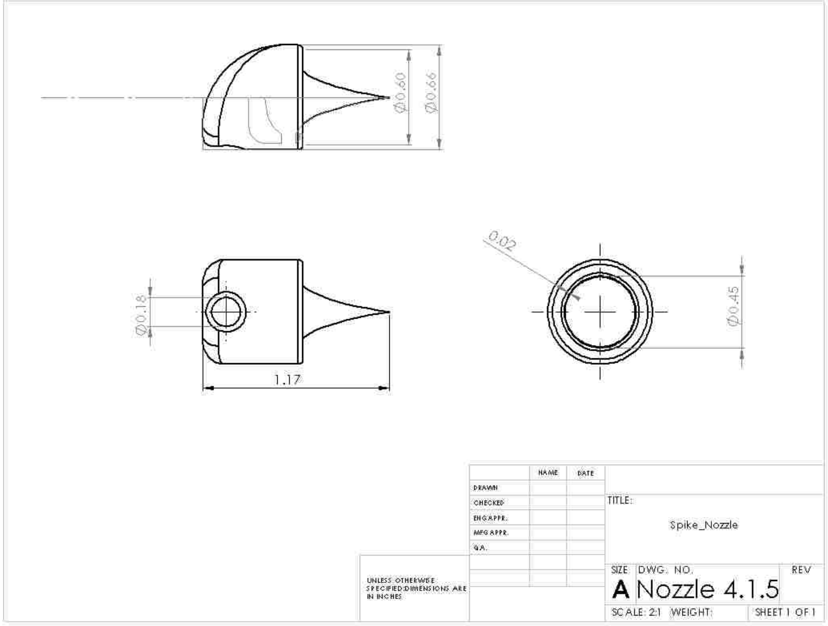

Figure 3.6 Aerospike Nozzle Dimensions

4. NOZZLE PERFORMANCE ANALYSIS AND CFD

This section describes the modeling and simulation of the aerospike nozzle flow using the commercial computational fluid dynamics (CFD) software package FLUENT provided by ANSYS. The goal of the CFD analysis is to evaluate the validity of the nozzle design method and the nozzle's ability to achieve the desirable performance. The flow-field, Mach number, pressure distribution, and thrust are the main investigated flow properties.

4.1. CFD NOZZLE GEOMETRY AND MODEL

The generated SolidWorks nozzle model was imported to ANSYS Workbench DesignModeler in order to create a two-dimensional model for simulation. A cross-sectional symmetry plane was created in the symmetry-plane of the nozzle to obtain an accurate cross sectional representation of the nozzle as shown in Figure 4.1.

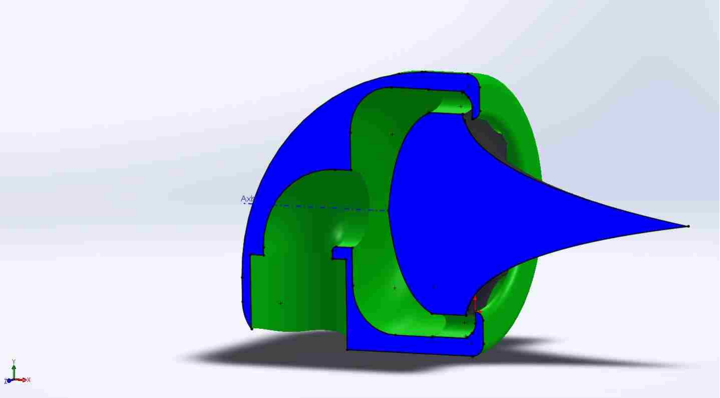

Figure 4.1 Nozzle Cross Section Used in Creating the Two-Dimensional Model

A computational domain was the constructed around the nozzle to simulate the vacuum environment in space as shown in Figure 4.2. It was important to extend the computational domain behind the nozzle throat to account for the massive expansion caused by the absence of ambient pressure. The geometry of the nozzle was split between three zones creating a multi-zone geometry as shown in Figure 4.2. The mulit-zone geometry allows for the construction of a high-quality mesh and reduced mesh element skewness. The multi-zone geometry also helps in obtaining structured mesh elements. Due to the axisymmetric nature of the investigated nozzle, only the top half of the nozzle is considered.

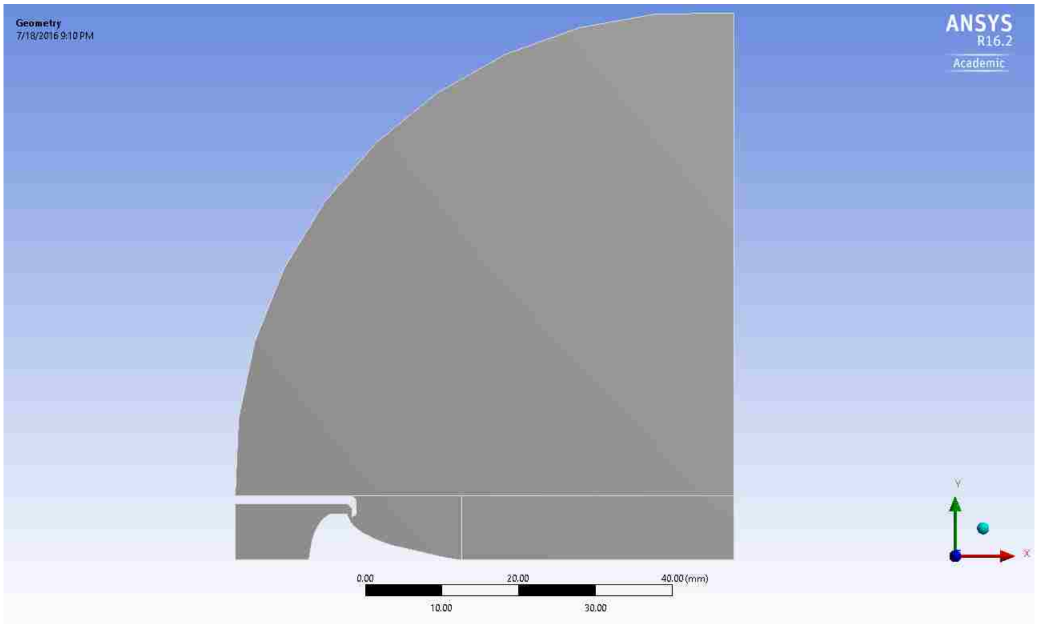

Figure 4.2 Nozzle Computational Flow-Field Domain

4.2. MESHING STRATEGY AND DETAILS

The meshing of the computational model was performed using the meshing tool available on ANSYS Workbench. Due to the complexity of the geometry of the plug nozzle and the existence of a number of curved surfaces it was not possible to obtain only structured quadrilateral mesh elements. The nozzle geometry was divided into three separate regions in order to increase the number of quadrilateral elements and reduce the number of triangular elements and obtain a high quality mesh; the different mesh regions are shown in Figure 4.2. It is usually favorable to obtain a structured mesh that is characterized by regular connectivity, however, this restricts the elements that can be used in the meshing process and might result in low-quality elements due to the complexity of the geometry. Low quality-elements affect the accuracy of the obtained solution. Hence, a hybrid mesh was used instead. A hybrid mesh contains structured and unstructured regions. The partial differential equations governing the fluid flow are discretized and solved within each separate mesh element. The mesh is shown in Figure 4.3.

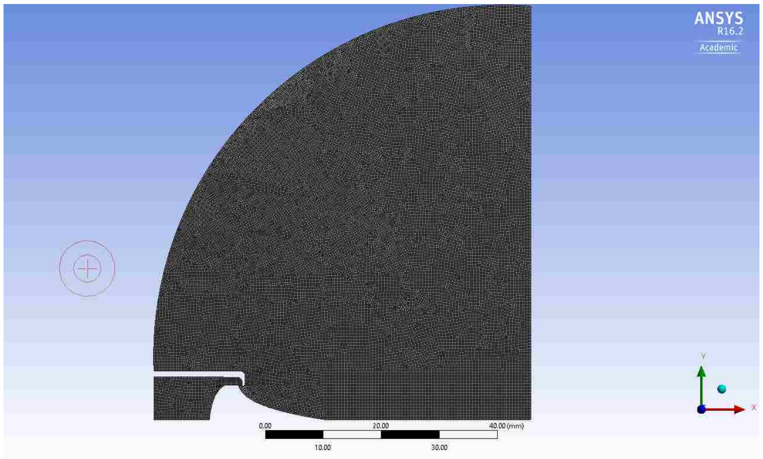

Figure 4.3 The Generated Mesh

Albeit, some of the mesh elements were not structured, due to the complexity of the computational domain, the overall quality of the mesh was improved by the multi-zone mesh. ANSYS uses a few measures to quantify the mesh quality. Two of the most important measures of mesh quality are mesh skewness and mesh orthogonal quality [33]. Skewness refers to the difference between the shape of an element to that of an ideal (equilateral or equiangular) element of the same area. Skewness determines how close to ideal a cell (element) is.

Typical skewness ranges and their respective cell quality are shown in Table 4.1. A skewness value between 0.5 and zero is desired and is usually and indicator of good cell quality. Orthogonal quality also ranges between zero and one, where values closer to one are best and values closer to zero are worst. Table 4.2 shows typical ranges of orthogonal quality and their respective cell quality.

Table 4.1 Skewness and Corresponding Element Quality

Skewness	Element Quality
0	Equilateral
0 – 0.25	Excellent
0.25 – 0.5	Good
0.5 – 0.75	Fair
0.75 – 0.9	Poor
0.9 – 1	Bad

The skewness and orthogonal quality of the generated mesh are shown in Figure 4.4 and Figure 4.5, respectively. The minimum skewness values is $1.415\text{x}10^{-10}$ and the maximum skewness value is 0.5135 with an average value of $2.0982\text{x}10^{-2}$. The minimum

Table 4.2 Orthogonal Quality and Corresponding Element Quality

Skewness	Element Quality
0	Equilateral
0.9 – 1	Excellent
0.9 – 0.7	Good
0.7 – 0.2	Fair
0.2 – 0.15	Acceptable
0.15 – 0	Bad

orthogonal quality is 0.7462 and the maximum orthogonal quality is 1 with an average value of 0.9976. The details of the mesh are illustrated in Table 4.3.

Table 4.3 Mesh Details

Type	Multi-zone Qaud/Tri
Number of Elements	58, 921
Average Skewness	0.002
Average Orthogonal Quality	0.99757

4.3. FLUENT SETUP

In order to model the supersonic flow of the aerospike nozzle and correctly capture the strong expansion expected at the exit of the nozzle, the correct computational setup was crucial for the accuracy of the simulation process. A density-based solver was utilized in the simulation. The density-based solver is recommended for high-speed compressible

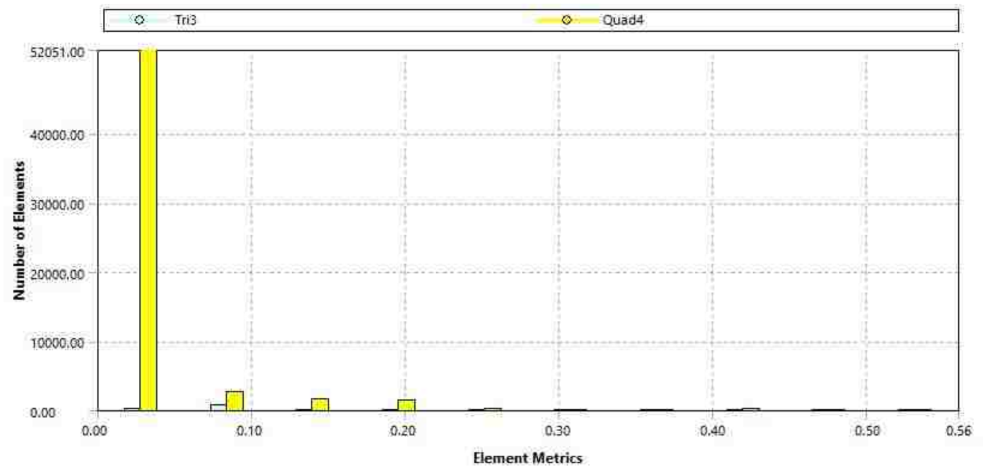

Figure 4.4 Skewness of the Generated mesh

flows formulation and it solves the coupled governing equations of continuity, momentum, and energy simultaneously. because the governing equations are nonlinear and coupled, several iterations of the solution loop must be performed by the solver before a converged solution can be obtained. An implicit linearization process of the governing equations was used in the density-based solver. This formulation allows for each equation in the coupled set of governing equations to be linearized independently with respect to all dependent variables in the equation set. The implicit formulation facilitates the solution of all variables (flow properties) in all cells in the computational domain at the same time. A flow chart simplifying the utilized solver formulation is shown in Figure 4.6.

Given the nature and geometry of the problem a double-precision solver was utilized in the solution process. For compressible flows that are driven by pressure differences and for flows through disparate length scales, FLUENT recommends the use of a double-precision solver. An energy-equation inviscid model was chosen for the simulation. The choice of

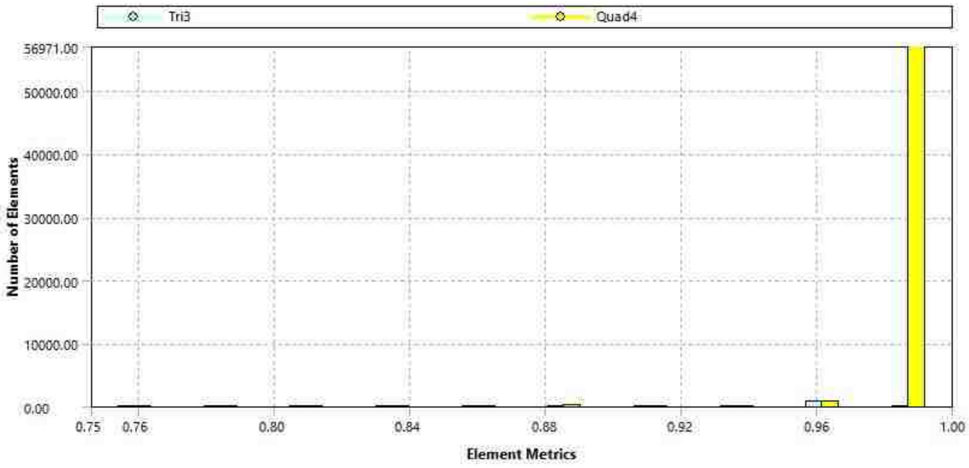

Figure 4.5 Orthogonal Quality of the Generated Mesh

an inviscid model is justified to capture the inviscid nature of the method of characteristic, which the development of the nozzle contour is based on. The two-dimensional space of the computational domain was modeled as an axisymmetric problem.

The FLUENT model's solver/solution information and operating conditions are illustrated in Table 4.4 and Table 4.5, respectively.

Table 4.4 Solver and Solution Information

Solver	Coupled
Type	Density-based
Velocity Formulation	Absolute
2-D space	Axisymmetric
Gradient option	Cell-based
Energy equation	Checked
Viscous model	Inviscid

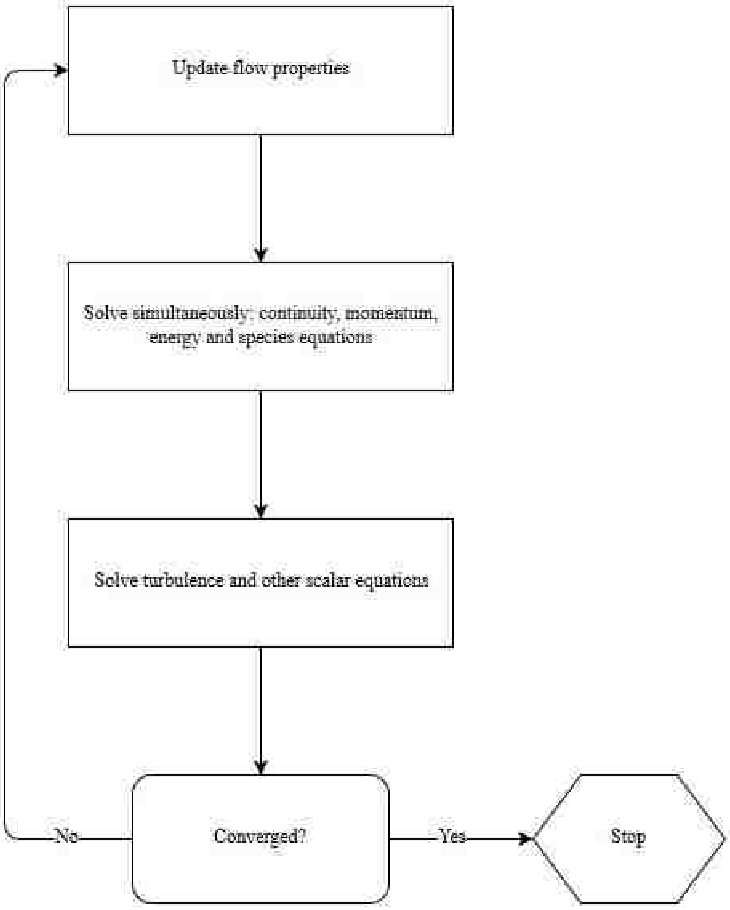

Figure 4.6 Flow Chart of The Density Based Method

Table 4.5 Operating Conditions

Gravity	Not checked
Operating pressure	0
Reference location X	0 (m)
Reference location Y	0 (m)

4.3.1. Fluid Type. Two fluids were initially considered for the simulation process. R-134a and R-410, however, both fluids gave very similar performance values. R-134a was modeled as an ideal gas that allows for the density of the fluid to be solved using the gas law for compressible fluids given by

$$\rho = \frac{P_{op} + P}{\frac{R}{M_w} T} \tag{4.1}$$

where P_{op} is the operating pressure, M_w is the molecular mass of the fluid, and R is the universal gas constant. Modeling the fluid as an ideal gas is recommended by FLUENT for compressible flow problems. R-410a was modeled in the same manner and only simulation for R-410a are discussed further due to the same performance of both refrigerants and to enable comparison with performance values obtained in Section 3.2. The material properties are shown in Table 4.6.

Table 4.6 CFD Model Material Proprieties

Material Type	Fluid
Density	Ideal gas
C_p	840.2 (j/kg-K)
M_w	72.58 (kg/kgmol)

4.3.2. Boundary Conditions. A total of five boundary conditions were necessary to obtain a numerical solution for the addressed problem. The edges of the domain of the model were split into five different boundaries in order to simulate the different initial conditions. As seen in Figure 4.7, in order to represent the pressure as primary driver of the thruster system, the boundary condition type utilized for the inlet of the nozzle was a pressure inlet. A pressure inlet is also the preferred boundary condition for compressible flow simulations. The nozzle contour and physical boundaries were modeled as walls. The domain was modeled as a pressure far-field. The pressure far-field conditions are used to model free-stream condition at infinity, with conditions specified, and is only applicable when the ideal gas law is used to define the density of the fluid. The far-field has been chosen to capture the strong plume caused by the nozzle's infinite expansion. The outlet of the domain was modeled as a pressure outlet. The pressure outlet boundary condition enables the extrapolation of the flow properties downstream of the nozzle from the flow interior. This is very useful because it is challenging to determine the conditions that far from the nozzle's physical exit in space. The details of the boundary conditions are shown in Table 4.7.

Table 4.7 Boundary Conditions Details

Boundary	**Type**	**Pressure (Pa)**	**Temperature (K)**
Inlet	Pressure inlet	170,300	300 (constant)
Outlet	Pressure outlet	5	300 (constant)
Far-field	Pressure far-field	5	300 (constant)
Cowl	Wall	N/A	N/A
Contour	Wall	N/A	N/A
Plug	Wall	N/A	N/A
Symmetry	Axis	N/A	N/A

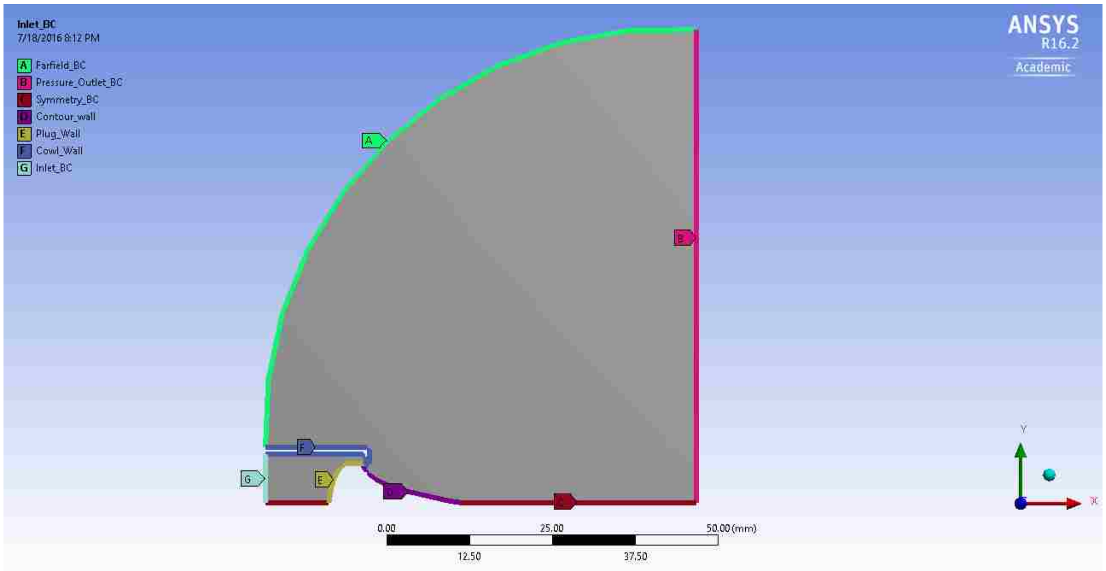

Figure 4.7 Domain of the Solution and Boundary Conditions

After correctly setting up FLUENT by identifying the solver, the fluid type, and the correct boundary conditions, the solution can be initialized and controlled as shown in Table 4.8 to commence the numerical procedure.

Table 4.8 Solution Control and Initialization Information

Discretization	Second order upwind
Courant number	1
Initialization	From inlet
Initial values	Computed from inlet
Reference frame	Relative to cell zone

4.4. VALIDATION MODEL

Before commencing the process of numerically evaluating the performance of the nozzle, it was necessary to apply the developed model on a known problem in order to ensure its validity and asses the accuracy of its predictions. The validation model consisted of a conical plug nozzle designed and simulated at California State University [34]. The simple conical shape of the nozzle contour allows for relatively simple reconstruction and meshing, following a similar strategy outlined in previous sections. The model was reconstructed using SolidWorks and then it was imported into ANSYS Workbench DesignModeler. After generating the virtual geometry, it was imported into ANSYS Workbench meshing feature and the model was meshed following the previously discussed procedure. The simulations were, then, conducted using the developed model and contours of the axial velocity as well as the pressure generated for comparison. The contours of velocity and pressure obtained by [34], shown in Figure 4.8 and 4.9, respectively, are compared against the velocity and pressure contours obtained using the generated and discussed CFD setup, shown in Figure 4.10 and 4.11, respectively.

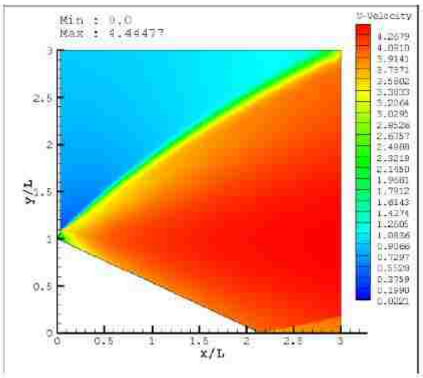

Figure 4.8 Normalized Axial Velocity Contours [34]

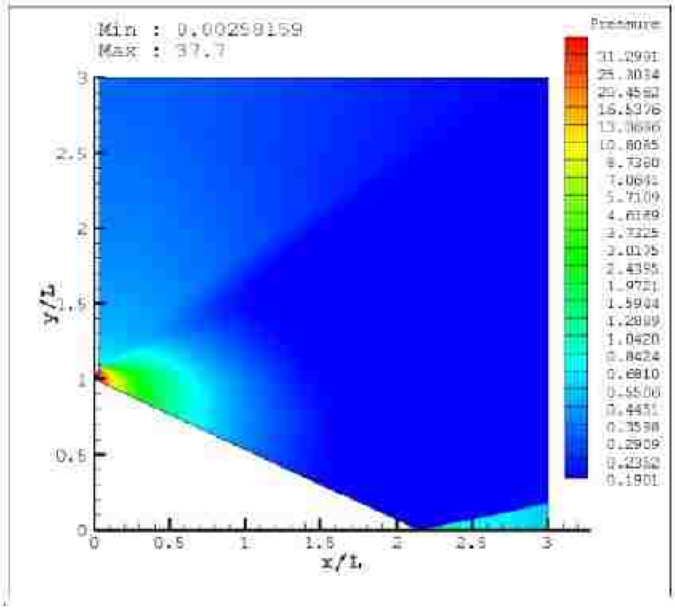

Figure 4.9 Normalized Pressure Contours [34]

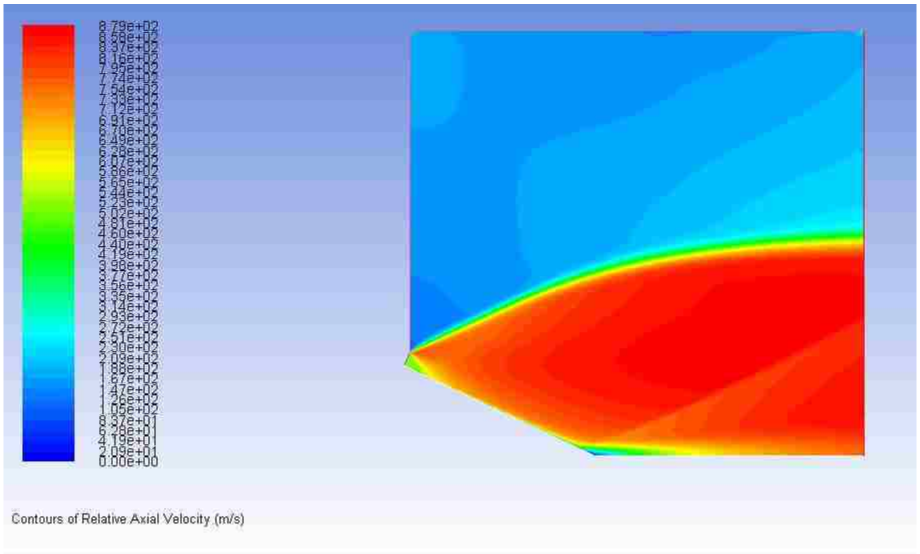

Figure 4.10 Generated Axial Velocity Contours

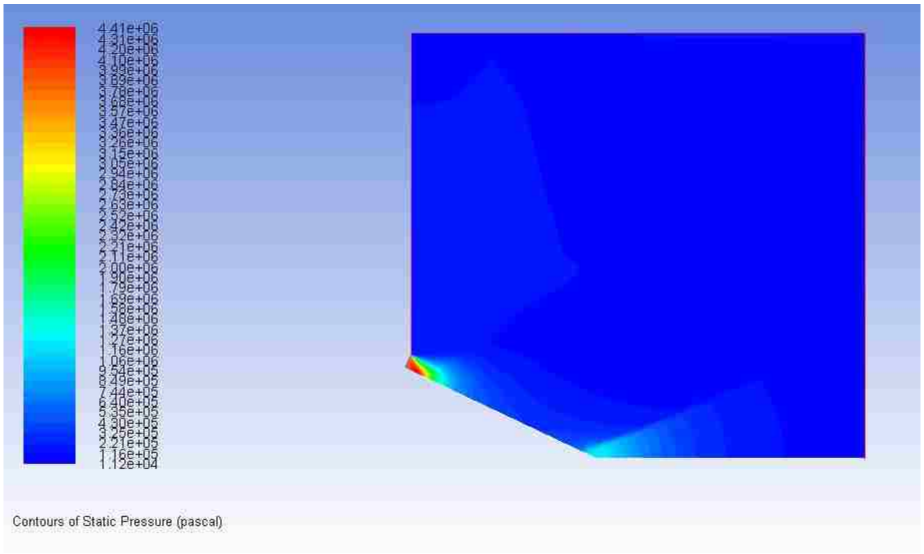

Figure 4.11 Generated Pressure Contours

Notice that the values of pressure and axial velocity from [34] were normalized. It is obvious that the established CFD model was capable of reproducing accurate results of the validation case and can be used to numerically evaluate the performance of the geometry and computational domain of the developed contoured aerospike nozzle.

4.5. FULL NOZZLE CFD RESULTS

As established, the aerospike nozzle is an expansion device that includes a primary nozzle (thruster) and a contoured plug on which the external flow expands. The inviscid solutions in space-like environment outlined by the Mach number contours shown Figure 4.12 and Figure 4.13, show that a very strong expansion of the jet plume is caused by the vacuum conditions and the infinite pressure ratio as expected and undergoes a centered expansion wave at the cowl lip and rotates up. The expansion of the jet boundary illustrates the effects of the absence of ambient pressure on the jet of an aerospike nozzle. This also shows the ability of the plug nozzle to adapt for different pressure ratios.

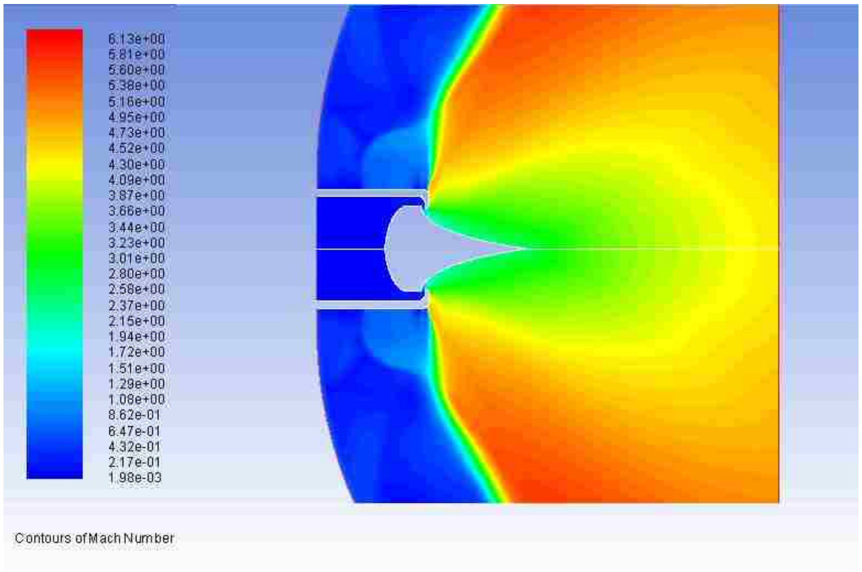

Figure 4.12 Full Nozzle Mach Number Contours

If the plug nozzle was numerically simulated at sea-level conditions, the jet boundary would be narrower and almost fully attache to the contour of the nozzle. A very high Mach number region is also observed above the cowl lip and an oblique shock wave that was caused by the infinite expansion of the flow is formed. The reflected expansion waves acting on the nozzle contour are canceled out by the suitable nozzle contour design. The maximum turning angle of the plume can be estimated using the Prandtl-Meyer relation and is found to be around 127.2°. Figures 4.12 and 4.13 also show that the flow expands on the nozzle contour as well as away from the contour forming a large exhaust plume. The

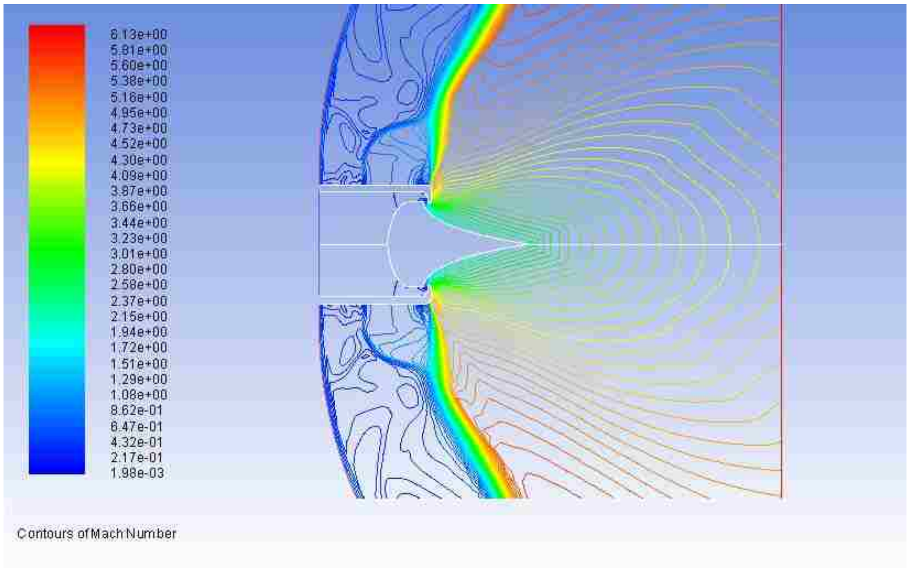

Figure 4.13 Full Nozzle not-Filled Mach Number Contours

analysis also shows that the domain of the expansion waves covers an area larger than the plug of the nozzle and the flow continues to expand after the plug. The pathlines of the flow also continue to diverge after the plug of the nozzle.

As seen in Figure 4.14, the pressure contours shown closely mimic the characteristic lines used in the design of the nozzle contour. The pressure distribution on the nozzle contour is shown in Figure 4.15. The strong expansion of the flow also causes a huge drop in the pressure when the flow exits the nozzle throat to the very low pressure space environment, as shown in Figures 4.14 and 4.14, and the pressure becomes a monotonically decreasing function.

Thrust is the major component of evaluating the performance of a nozzle of a certain propulsion system. The thrust of an aerospike nozzle is calculated differently than that of a conventional nozzle. There are three main components of thrust in an aerospike nozzle.

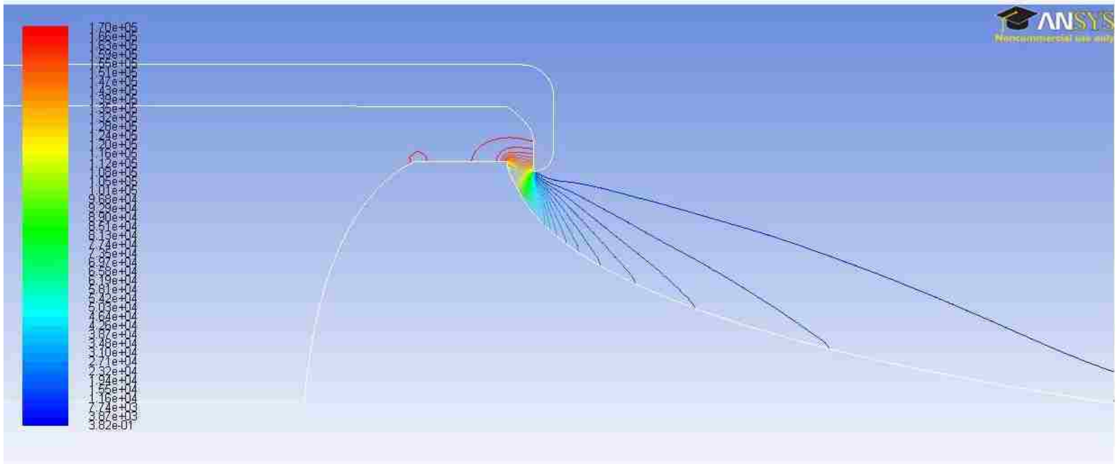

Figure 4.14 Full Nozzle Pressure Contours

The thrust produced by the thruster of the nozzle at the throat which can be calculated using the mass flow and pressure at the nozzle throat. The second component of thrust of an aersopike nozzle is the thrust produced by the contour of the nozzle, which can be calculated by integrating the pressure distribution on the contour along the plug of the nozzle. The third and final thrust component is the thrust produced by the base of an aerospike nozzle when it is truncated. Truncation of the plug of an aerospike nozzle allows for a shorter nozzle without a significant penalty on thrust as shown in the following sections. The base thrust can be calculated by multiplying the base area and the pressure acting on it. The total thrust force is the summation of the, thruster, contour, and base thrust components. Notice that the base thrust for an ideal full spike plug nozzle is equal to zero. Table 4.9 shows the thrust produced by the aerospike nozzle and the updated performance parameters of the system.

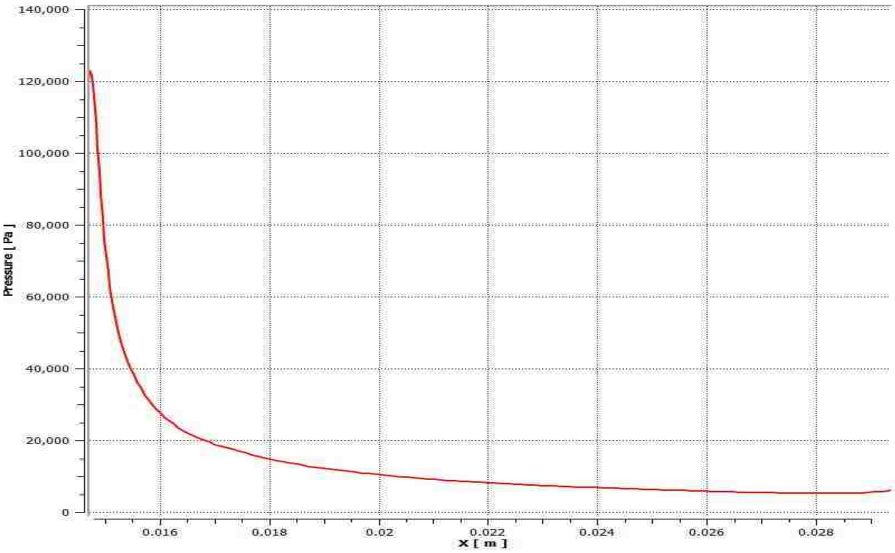

Figure 4.15 Full Nozzle Pressure Distribution on Plug

Table 4.9 Updated LCQ Satellite Capabilities

I_{sp}	50.2209 (s)
Thrust	3.5169 (N)
ΔV	340.6046 (m/s)
$\dot{m}$	0.0071 (kg/s)

4.6. TRUNCATED NOZZLES

The aerospike nozzle can be truncated in order to reduce the mass and limit the space of a propulsion system. However this truncation causes some changes in the flow-field of the plug nozzle. Given the small nozzle geometry it was decided to truncate the nozzle to

50 and 20 percent of its original length. The same boundary conditions were utilized for the truncated versions, with exception of creating another boundary for the nozzle base. The geometry and boundary conditions of the 50 percent and 20 percent truncated nozzle can be seen in Figures 4.16 and 4.17, respectively.

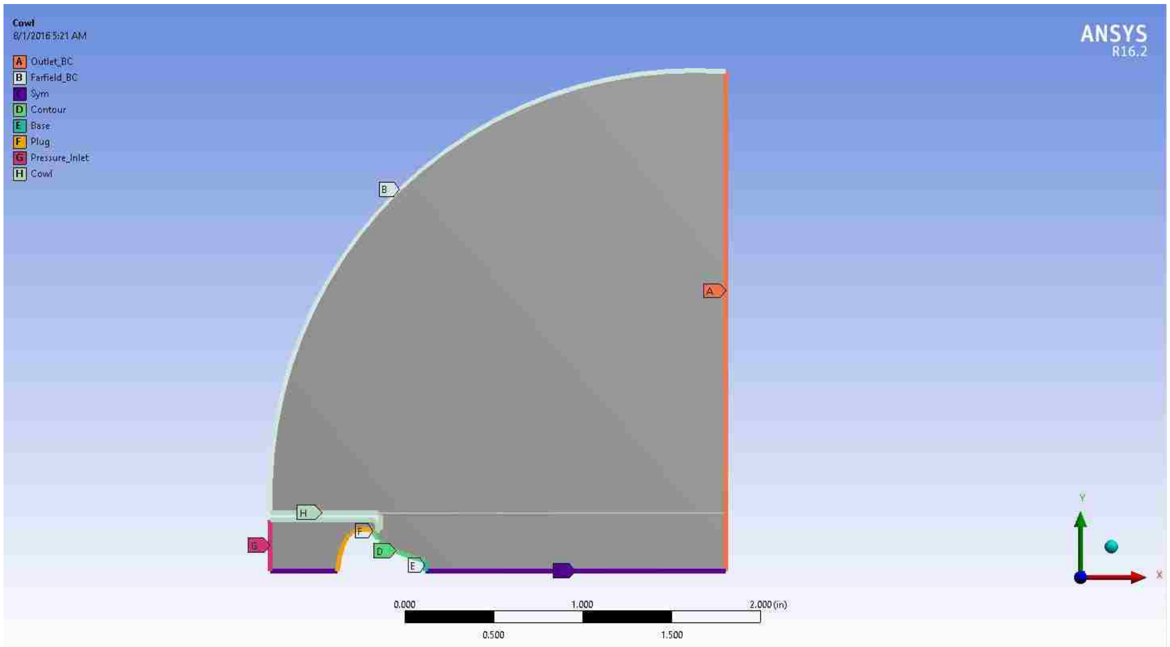

Figure 4.16 Domain of the Solution and Boundary Conditions of the 50% Truncated Plug Nozzle

The mesh details of the 50 percent and 20 percent truncated nozzle geometries are summarized in Table 4.10. The same FLUENT setup described in the previous sections was utilized in the numerical analysis. Table 4.11 illustrates the boundary conditions used for the truncated nozzles.

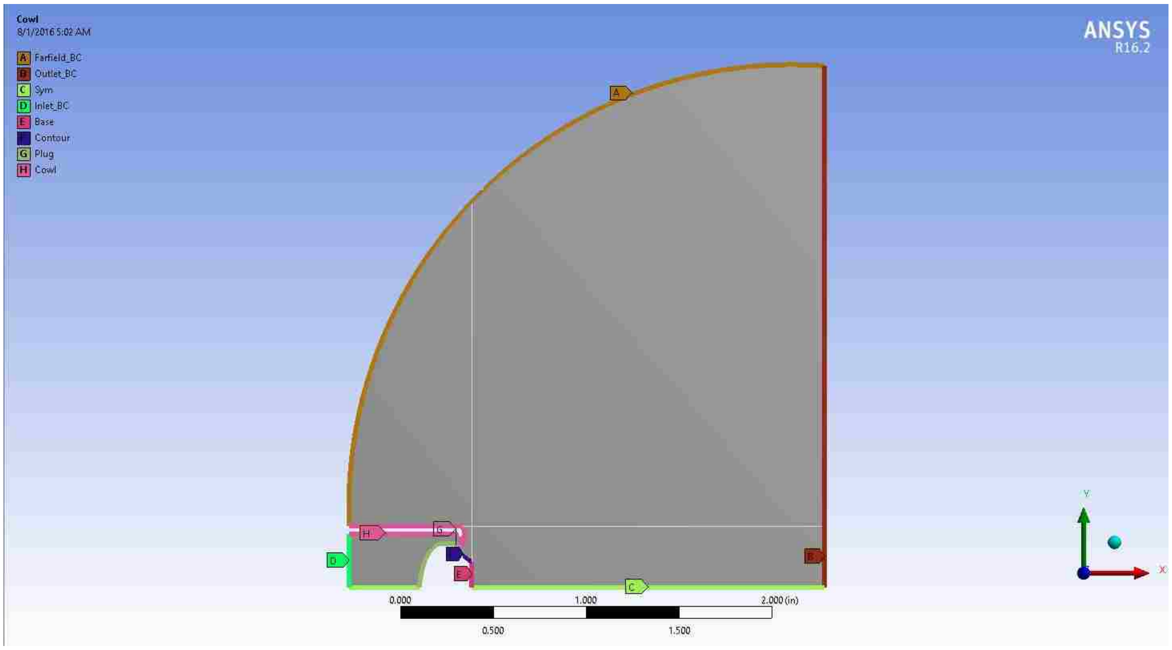

Figure 4.17 Domain of the Solution and Boundary Conditions of the 20% Truncated Plug Nozzle

Table 4.10 Mesh Details for 50% and 20% Truncated Plug Nozzles

50% Nozzle	
Type	Multi-zone Qaud/Tri
Number of Elements	74,160
Average Skewness	0.0052
Average Orthogonal Quality	0.988
20% Nozzle	
Type	Multi-zone Qaud/Tri
Number of Elements	48,000
Average Skewness	0.0056
Average Orthogonal Quality	0.9926

Table 4.11 Boundary Conditions Details for the 50% and 20% Truncated Plug Nozzles

Boundary	**Type**	**Pressure (Pa)**	**Temperature** (°K)
Inlet	Pressure inlet	170,300	300 (constant)
Outlet	Pressure outlet	5	300 (constant)
Far-field	Pressure far-field	5	300 (constant)
Cowl	Wall	N/A	N/A
Contour	Wall	N/A	N/A
Plug	Wall	N/A	N/A
Base	Wall	N/A	N/A
Symmetry	Axis	N/A	N/A

4.6.1. Effects of Truncation on the Flow-field. As seen in Figure 4.18 the 50 percent plug nozzle behaves differently and results in a different flow-field structure than that of the full spike (100 percent nozzle). In Figure 4.19 a very strong expansion of the jet plume is observed and is caused by the absence of the ambient pressure boundary. A trailing shock wave is observed downstream from the base of the nozzle and is caused by the expansion of the flow at the truncated edge of the nozzle and the convergences of the flow at the symmetry axis. The Mach number contours of the 50 percent configuration, shown in Figure 4.18 and Figure 4.19, show that the expansion waves originating from the tip of the cowl face the truncation point of the aerospike nozzle which causes the flow to encounter a sharp expansion which also results in a high-Mach number region of flow above the plug of the nozzle. A portion of the flow continues to converge towards the nozzle axis and continues expanding beyond the nozzle plug. Notice that a portion of the expansion waves result in rotational flow at the base of the nozzle inflicting a pressure force on its surface.

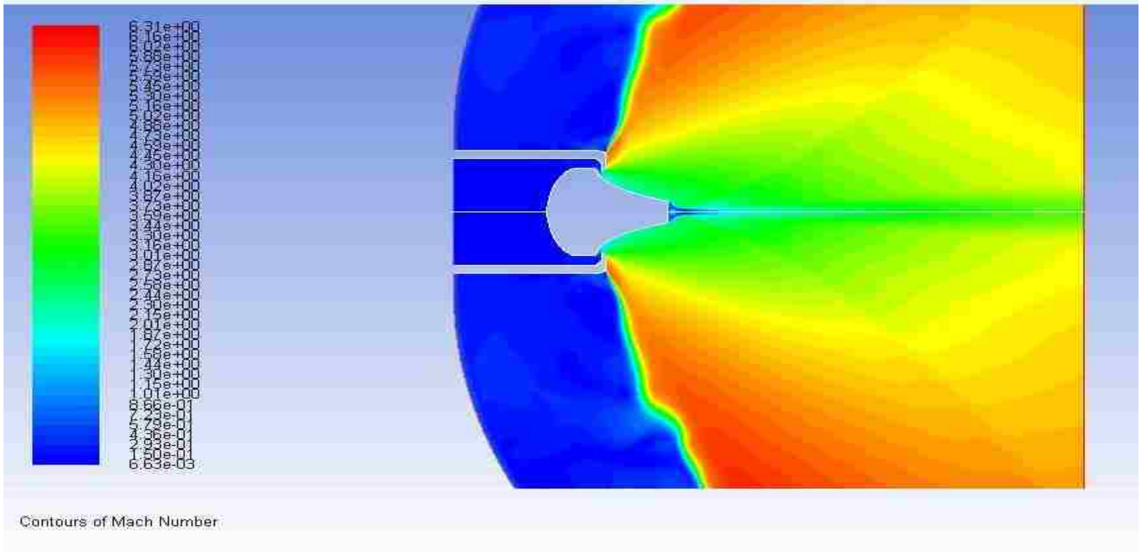

Figure 4.18 50% Truncated Nozzle Mach Number Contours

The Mach number contours of the 50 percent configuration, shown in Figure 4.18 and Figure 4.19, show that the expansion waves originating from the tip of the cowl face the truncation point of the aerospike nozzle which causes the flow to encounter a sharp expansion which also results in a high-Mach number region of flow above the plug of the nozzle. A portion of the flow continues to converge towards the nozzle axis and continues expanding beyond the nozzle plug. Notice that a portion of the expansion waves result in rotational flow at the

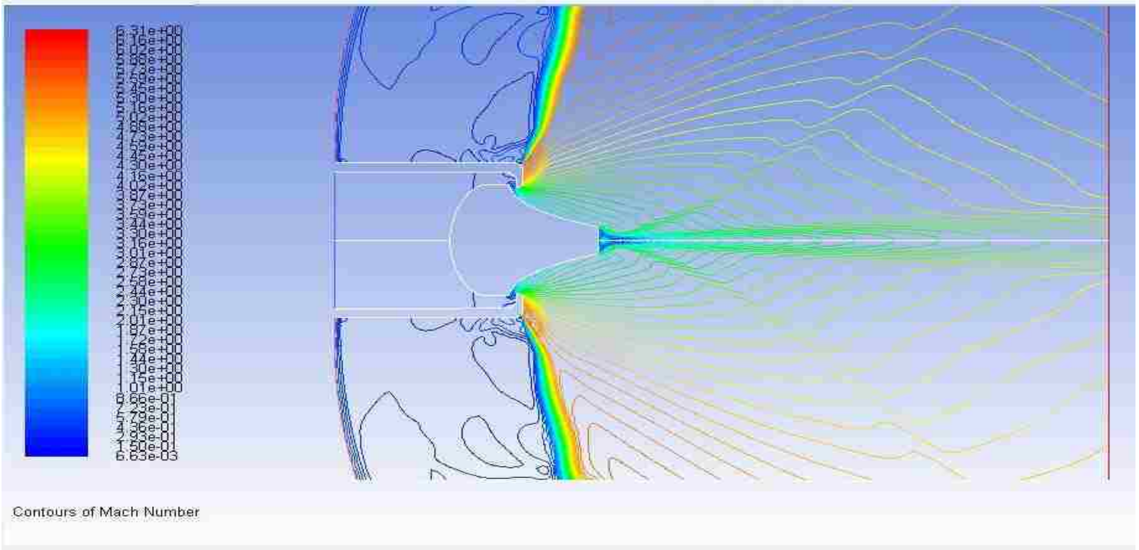

Figure 4.19 50% Truncated Nozzle not-Filled Mach Number Contours

Further, similar to the 100 percent nozzle case, the jet boundary locally expands more stronger and more fiercely due to the absence of ambient pressure and the local Mach number value also becomes very high. Furthermore, the convergence of the jet downstream of the nozzle base on the axis causes the base-flow region to be independent from ambient conditions. And because the external pressure is very low, the difference between the isolated base pressure and the ambient pressure also increases. This becomes very important when the base pressure is calculated and it serves as demonstration of the important advantages of plug nozzles operating in space environment. Figure 4.20 shows the pressure contours of the 50 percent truncated plug nozzle, and the pressure distribution on the plug contour of the 50 percent nozzle can be seen in Figure 4.21.

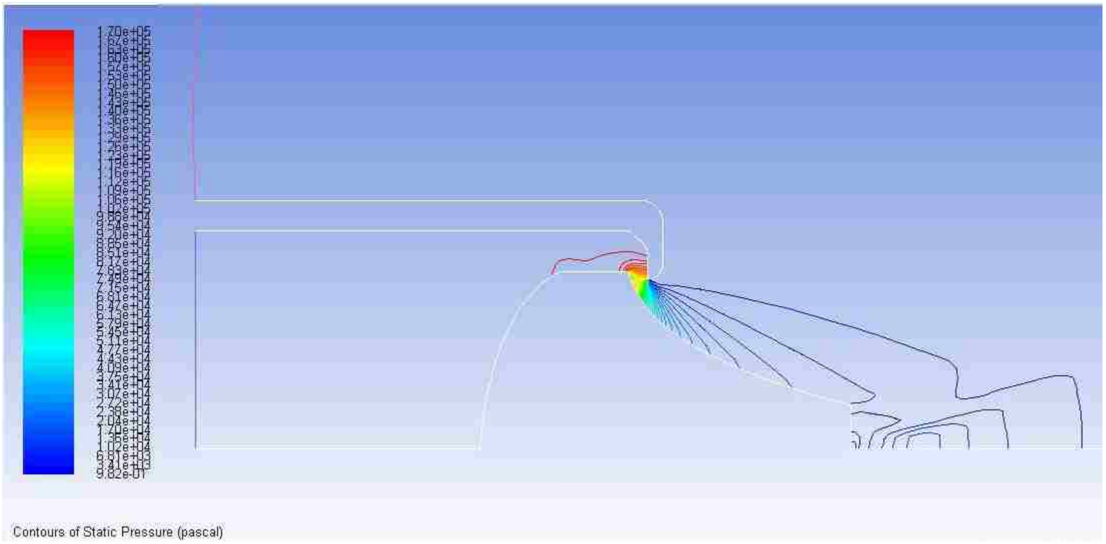

Figure 4.20 50% Truncated Nozzle Pressure Contours

The previous trend also occurs in the 20 percent truncated nozzle case. However, as show in Figure 4.23, the expansion of the jet is even stronger and fiercer because the flow encounters the truncated portion of the nozzle in an even shorter distance and the expansion waves originating from the plug encounter another expansion wave cased by the expansion of the flow at the tip of the truncated region of the plug resulting in a very high-Mach number region. Figure 4.22 and Figure 4.23 shows the Mach number contours of the 20 percent truncated spike. After encountering the trailing shock wave, the flow will further expand after the truncated region and converges downstream at the symmetry axis of the nozzle.Figure 4.24 shows the pressure contours of the 20 percent truncated plug nozzle, and Figure 4.25 shows the pressure distribution on the contour of the plug. Due to the absence of ambient pressure, the expansion covers an area larger than the plug itself in all spike configurations.

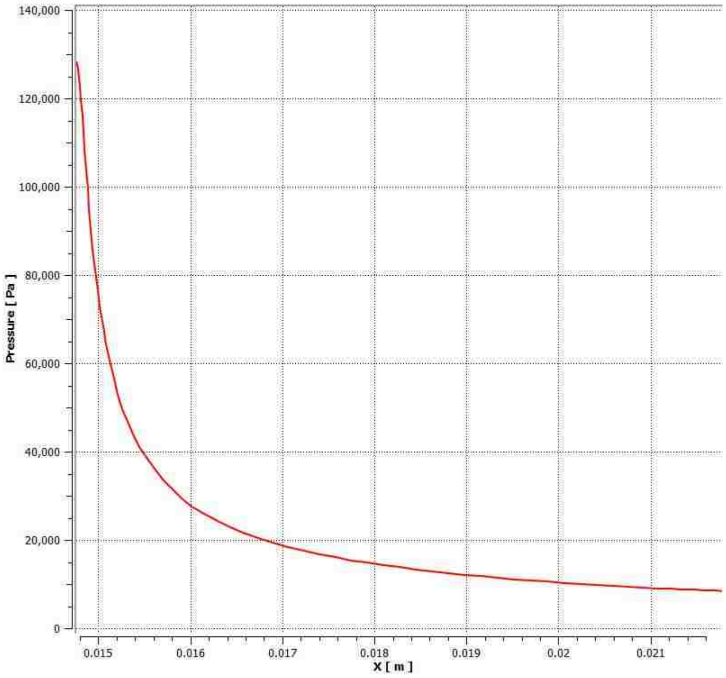

Figure 4.21 50% Truncated Nozzle Pressure Distribution on Plug

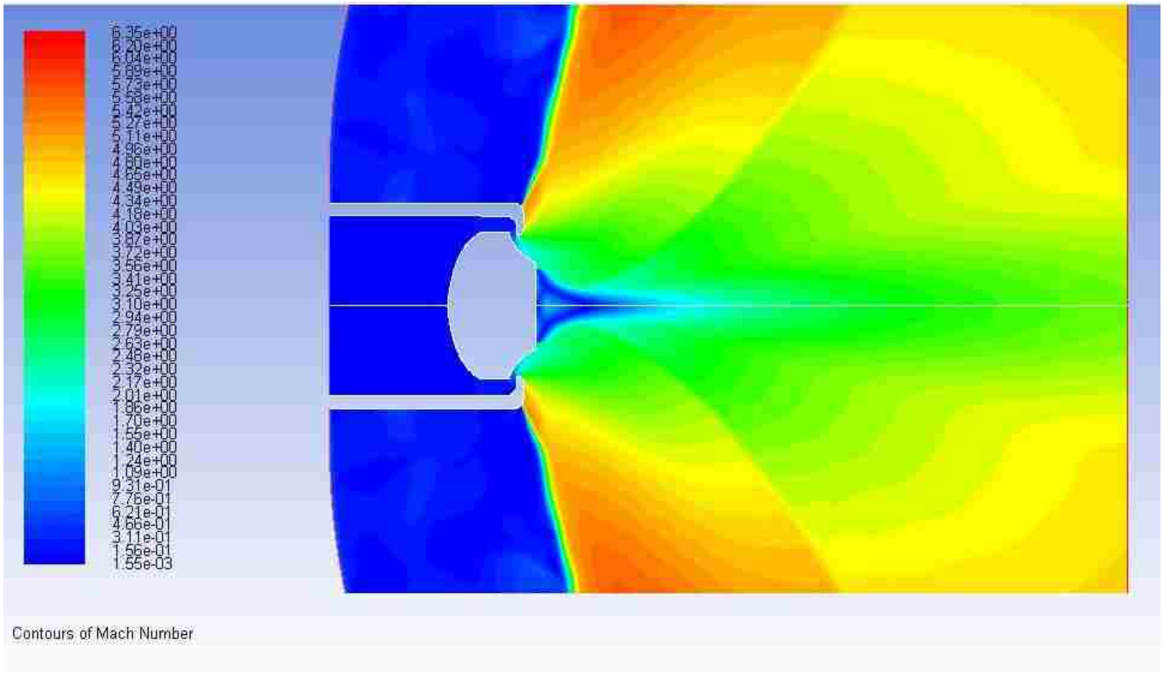

Figure 4.22 20% Truncated Nozzle Filled Mach Number Contours

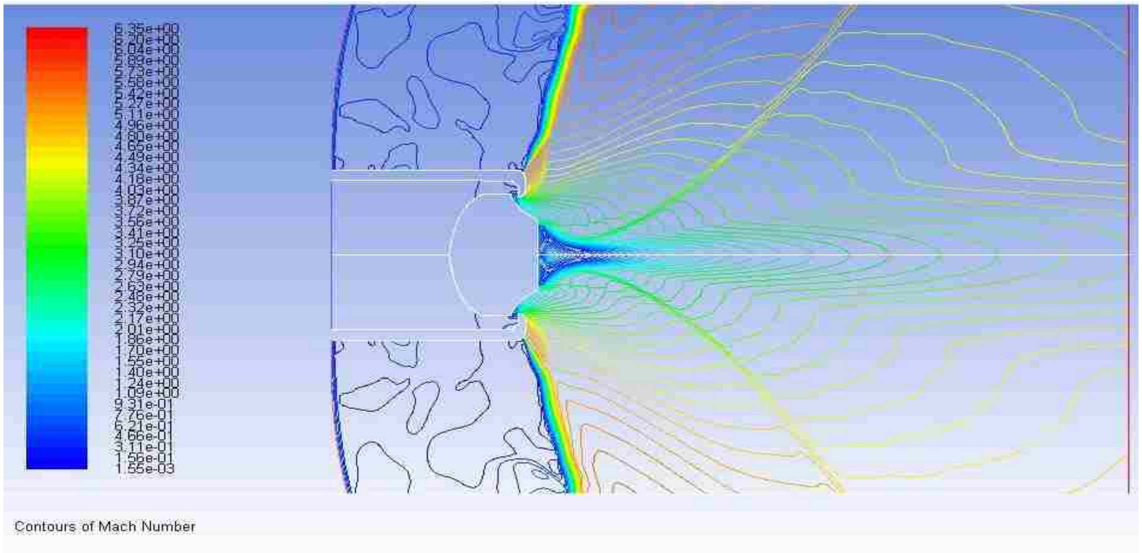

Figure 4.23 20% Truncated Nozzle not-Filled Mach Number Contours

4.6.2. Effects of Truncation on Thrust. As previously mentioned, the thrust of any propulsion system is a usually a good indicator of its performance. The thrust produced by an axisymmetric plug nozzle has three main components: the thrust produced by the thruster exit (throat), the thrust produced by the plug region, and the thrust produced by the base region. For an ideal 100 percent spike nozzle the base area is equal to zero. The base region of the plug nozzle becomes of great importance when the nozzle is operated in spaceflight and vacuum environment.

When truncation of the plug of an aerospike nozzle occurs, the nozzle plug becomes shorter and the area of the surface area of the plug decreases which causes the the portion of thrust produced by the the plug's ramp to be reduced. However, this truncation also causes the base region to have a larger area which causes the thrust portion produced by the base region of the nozzle to increase when it is operated in very low-pressure environments. This

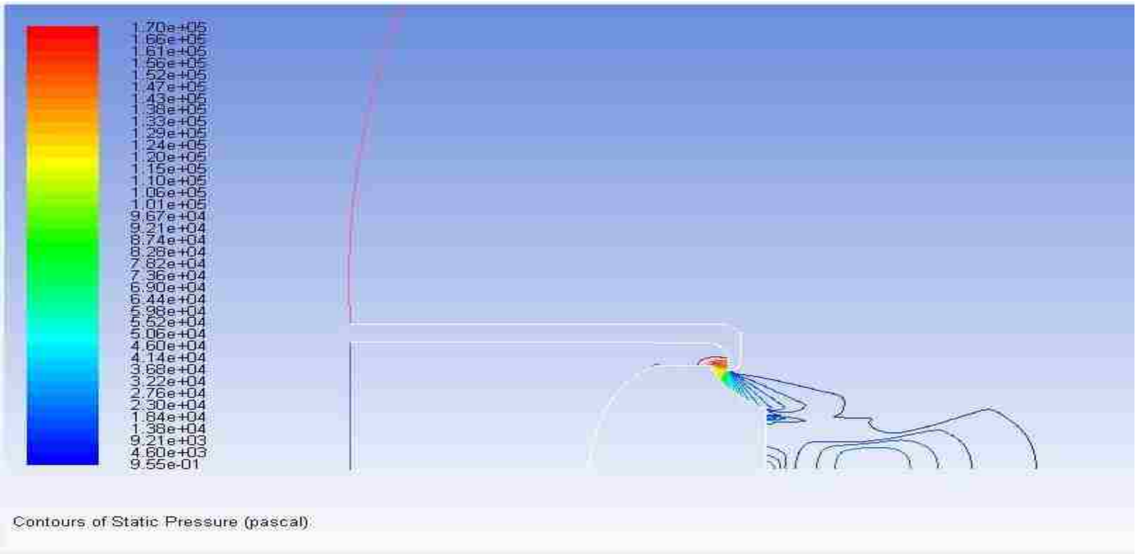

Figure 4.24 20% Truncated Nozzle Pressure Contours

increase in the base thrust compensates the loss of thrust by the shortened plug and reduced plug surface area. The contribution of thrust by each thrust component to the total thrust is shown in Figure 4.26.

When the nozzle is truncated, the plug is shortened and its lateral area decreases consequently. This decrease causes the thrust component of the ramp to decrease as well, as shown in Figure 4.26. Although the thrust produced by the nozzle plug is decreased, the thrust component produced by the base region is increased due to the increased base area caused by the truncation of the plug. This compensates the loss in thrust from the shortened plug, and the total thrust produced becomes almost equal for all of the nozzle's different truncation configurations. This effect is reversed during operation in atmospheric conditions. For example, in over-expanded plug nozzles, the ambient pressure is higher than the exhaust pressure and would result in a negative base region thrust component. The

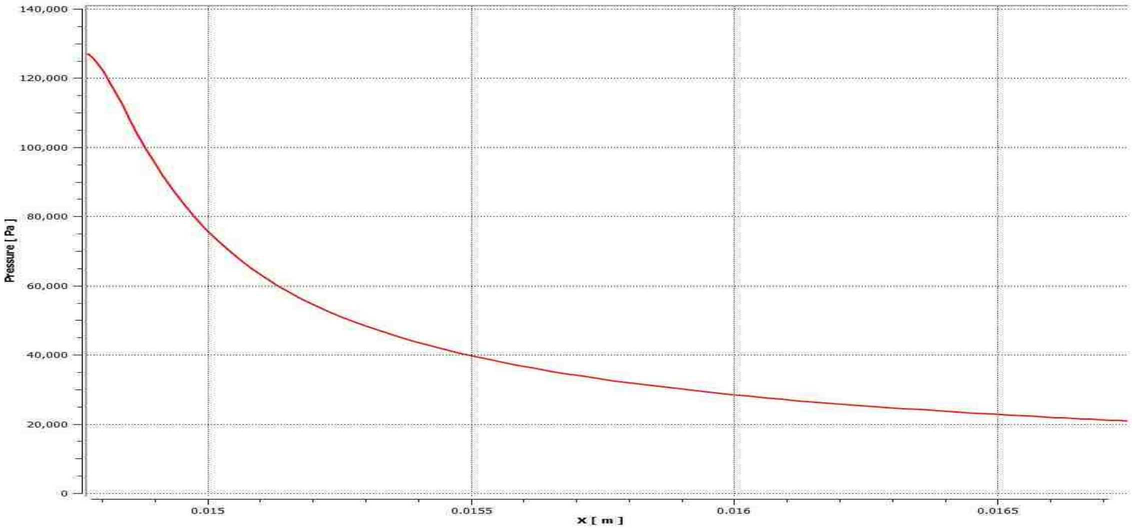

Figure 4.25 20% Truncated Nozzle Pressure Distribution on Plug

very high altitude of the spacecraft causes a constant pressure acting on the base region of the nozzle. As established in the previous section, this is caused by the convergence of the exhaust plume downstream the nozzle's base on the symmetry axis. Hence, the base is isolated from external conditions. The absence of ambient pressure results in positive ambient-to-base pressure value.

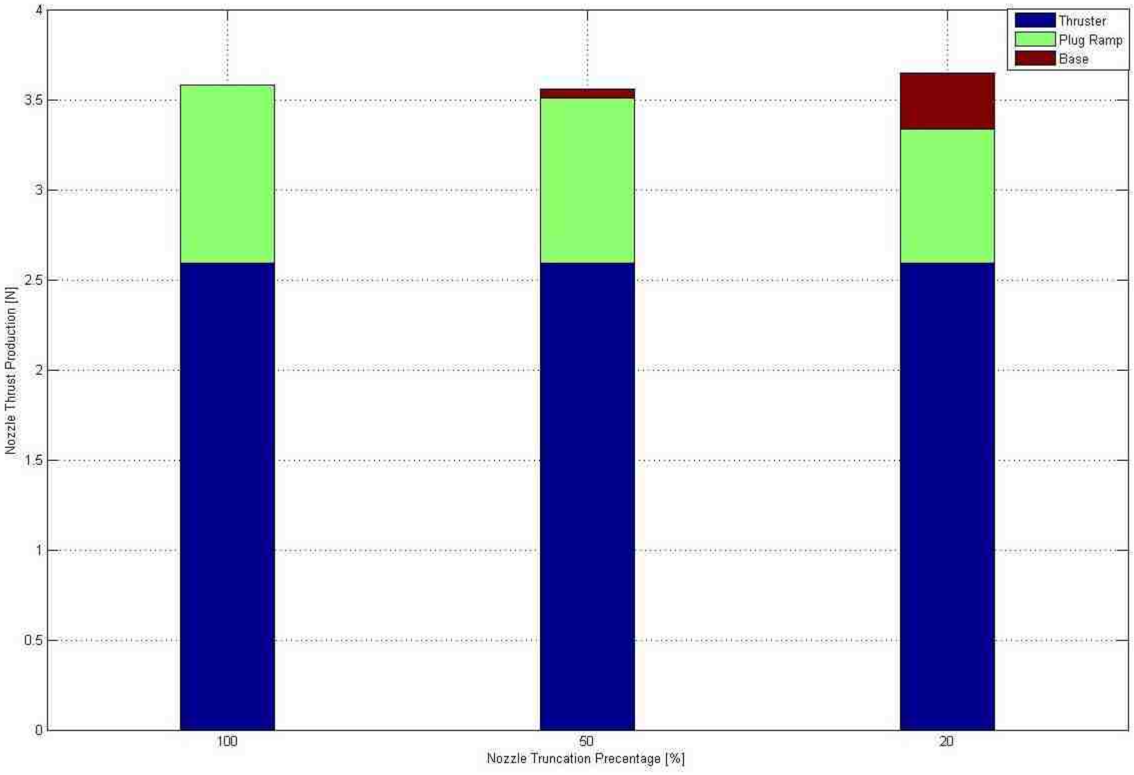

Figure 4.26 Comparison of Thrust Produced by Different Nozzle Truncations

5. RECOMMENDATIONS AND FUTURE WORK

Computational fluid dynamics is a third approach that complements theory and testing. CFD is an intermediate step synergistically complementing the pure theoretical considerations and the actual testing and experiment. However, CFD does not replace either of theory or experiment. It helps to identify, understand, and interpret the results of theory and weigh the performance of the presented designs to save time and cost allowing for minimal cost design modifications.

It is recommended to increase the procedure ability to more accurately predict and investigate real flow regimes by expanding it on it to include the effects of rotational flow and viscosity. As was noted, CFD provides an intermediate step between theory and experiment; to that end, future testing of the propulsion system should be conducted by the team and must take place in a thermal-vacuum chamber to asses the accuracy of the presented analysis and accurately determine the thrust capabilities of the refrigerant based cold-gas propulsion system and the thruster. A comparison of the actual thrust obtained from testing the aerospike nozzle against the theoretical values ideal values obtained by numerical CFD analysis will validate the accuracy of the presented nozzle design and the developed procedure for the nozzle design. This comparison will allow the M-SAT team to predict accurate thrust ratios and might prove to save overall mass and cost of the satellite.

More exhaustive and extended research that are beyond the scope of this research can be performed on the aerospike nozzle. This thesis provides design and analysis procedure that allows for increasing the limited amount of research and testing data available on aerospike nozzle and to outline their advantages for use in very high altitudes and spaceflight environment. However, with extended laboratory testing, the propulsion system can be validated and could be implemented as the propulsion system of the LCQ CubeSat. Although, the LCQ team placed placed sixth in Ground Tournament 2 (GT-2), which disqualified the team from obtaining a launch opportunity on the Space Launch System (SLS), the team is continuing its mission of developing a cold gas propulsion system for microsatellites and CubeSats. Further, the team will examine some other launch options such as the United Launch Alliance (ULA – a fifty-fifty joint venture owned by Lockheed Martin and the Boeing Company) who are offering free launch opportunities for CubeSats.

6. SUMMARY AND CONCLUSIONS

The goal of this thesis study was to expand on the gained knowledge of the M-SAT team in its pursuit of developing a low-cost cold-gas propulsion system. Cold-gas propulsion systems can be the future of safe and low-cost propulsion systems for small spacecraft. This thesis provides further enhancement of the capabilities of the refrigerant-based system. A refrigerant-based cold-gas propulsion system is a relatively low-cost system compared to other propulsion systems and is safe to handle and assemble due to the nature of the refrigerant propellants. The propellant system has the ability to use either R-410a or R-134a propellants.

In their mission to develop a low-cost refrigerant-based cold-gas propulsion system, the M-SAT team continues to work on and develop new technologies as well as expand and enhance existing ones. This study documents the procedures of developing an aerospike nozzle for a small spacecraft's cold-gas propulsion system. This procedure includes the design process from research to design and analysis.

An aerospike micro-nozzle has been designed, modeled and numerically tested using the computational fluid dynamics (CFD) commercial code FLUENT. CFD analysis predicts the performance of the aerospike nozzle in space environment including the flow-field and thrust capabilities of the nozzle. The thrust of a plug nozzle has three main components: thrust resulting from the thruster (throat) of the nozzle, thrust resulting from the pressure force acting on the plug of the nozzle, and finally, the thrust produced by the base of the nozzle if the nozzle is truncated. The obtained results show the main advantages demonstrated by plug nozzles. The increase in thrust and the insensitivity to nozzle truncation due to the increased base area in spaceflight. The reduction in thrust caused by truncating the plug of the nozzle is almost completely compensated for by the thrust produced by the base pressure of the nozzle. At high altitudes the base area of the nozzle becomes isolated from ambient conditions and the flow of the nozzle creates a constant pressure that acts on it. With the value of the ambient pressure close to zero in orbit, a positive pressure deficit that contributes to the total thrust force is established on the base of the nozzle. The use and selection of the truncation amount, when small spacecrafts are considered, will mainly depend on the flight envelope restrictions and the required ease of integration. However, it is established that the plug nozzle has the ability to provide more thrust, resulting in improved performance, compared to a conventional nozzle of the same area expansion ratio. With the improvements in capabilities that this design offers, university satellites might now investigate and attempt missions that would have required more complicated, unsafe, and expensive propulsion system options to produce marginally higher thrust values.

The performed CFD analysis might over-predict the nozzle performance due to the assumptions of inviscid, isentropic, irrotational flow. However, it can be concluded that CFD analysis and the codes presented in this research can serve as design tool for supersonic micro-nozzle design for small spacecraft propulsion systems. The developed procedure can serve as a tool for the M-SAT team and other university-based satellite research teams to investigate other types of rocket nozzles and further advance the limited data and research available on aerospike nozzles.

A plug nozzle operating in near-vacuum or spaceflight could provide a higher area expansion ratio (AR) than a conventional C-D nozzle. The higher expansion presented by the aerospike nozzle results in an increase in specific impulse (I_{sp}) and in higher thrust values. This might translate to a decrease in the needed propellant mass, and subsequently a decrease in the overall mass of the spacecraft.

APPENDIX A

PRANDTL-MEYER WAVE THEORY AND THE PRANDTL-MEYER FUNCTION

This section discusses the meaning of the Prandtl-Meyer expansion waves and the derivation of the Prandtl-Meyer function used in the nozzle design method as shown by [21]. All information presented here is from [21] and a more detailed discussion is available in the original source.

PRANDTL-MEYER WAVE THEORY AND DERIVATION OF THE PRANDTL-MEYER FUNCTION

The Prandtl-Meyer wave theory explains the formation of an expansion wave when a supersonic flow is turned away from itself. This phenomenon is the opposite of formation of a shock wave when a flow is turned into itself. An expansion corner will increase the flow Mach number (M) as seen in Figure A.1. Furthermore, the density (ρ), pressure (P), and temperature (T) of the flow will decrease through an expansion corner. The expansion fan is a continuous region composed of infinite number of Mach waves that are bounded by the Mach angles given by μ_1 and μ_2 upstream and downstream, respectively, as seen in Figure A.1. The streamlines of the flow through an expansion corner are smooth curved lines. Also, The expansion through an expansion wave is isentropic.

A centered expansion fan is an expansion wave originating from a sharp convex corner. With reference to Figure A.1, if the flow properties upstream of the expansion fan are known, the goal is to determine and establish the flow properties (M_2, P_2, T_2) downstream of the expansion fan.

As shown in Figure A.2, consider an infinitesimal change across a Mach wave that is produced by an infinitesimal deflection in the flow ($d\theta$), the low of cosines is used to define the flow velocity, V, such

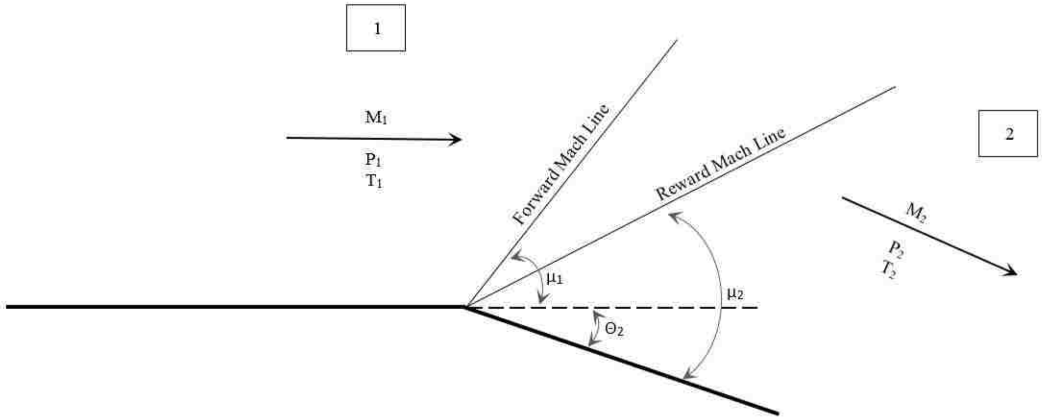

Figure A.1 Generic Prandtl-Meyer Expansion Wave

$$\frac{V + dV}{V} = \frac{\sin\left(\frac{\pi}{2} + \mu\right)}{\sin\left(\frac{\pi}{2} - \mu - d\theta\right)} \tag{A.1}$$

Recall the following trigonometric identities

$$\sin\left(\frac{\pi}{2} + \mu\right) = \sin\left(\frac{\pi}{2} - \mu\right) = \cos\mu \tag{A.2}$$

$$\sin\left(\frac{\pi}{2} - \mu - d\theta\right) = \cos\left(\mu + d\theta\right) = \cos\mu\cos d\theta - \sin\mu\sin d\theta \tag{A.3}$$

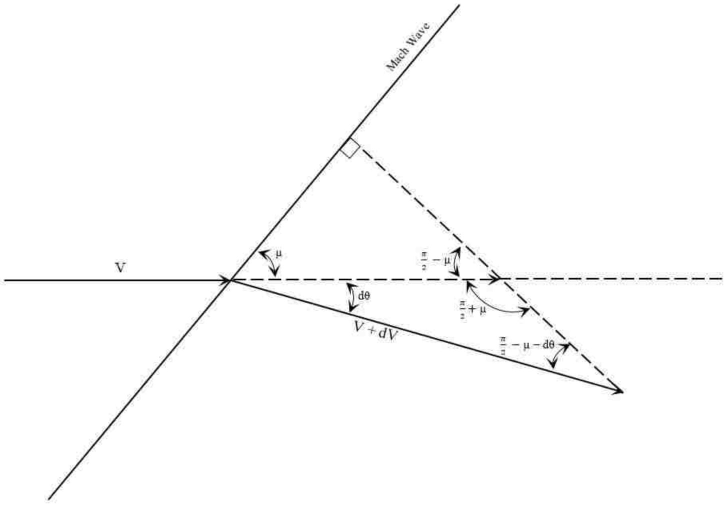

Figure A.2 Infinitesimal Changes Across Mach Wave

Using Equations A.2 and A.3, Equation A.1 becomes

$$1 + \frac{dV}{V} = \frac{\cos\mu}{\cos\mu\cos d\theta - \sin\mu\sin d\theta} \tag{A.4}$$

Using the small angle assumption for the infinitesimal change $d\theta$, Equation A.4 can be rewritten as

$$1 + \frac{dV}{V} = \frac{\cos\mu}{\cos\mu - d\theta\sin\mu} = \frac{1}{1 - d\theta\tan\mu} \tag{A.5}$$

Expanding Equation A.5 as a series and ignoring the second order and higher-order terms in the expansion

$$1 + \frac{dV}{V} = 1 + d\theta \tan \mu + \ldots \tag{A.6}$$

Solving for $d\theta$

$$d\theta = \frac{\frac{dV}{V}}{\tan \mu} \tag{A.7}$$

The Mach angle, μ is defined as

$$\mu = \sin^{-1} \frac{1}{M} \tag{A.8}$$

From trigonometric relations, Equation A.8 can also be written as

$$\tan \mu = \frac{1}{\sqrt{M^2 - 1}} \tag{A.9}$$

Now, substituting Equation A.9 in Equation A.7

$$d\theta = \sqrt{M^2 - 1}\frac{dV}{V} \tag{A.10}$$

Equation A.10 is the governing equation of the Prandtl-Meyer flow. Equation A.10, that treats an infinitesimally small deflection (expansion), can be integrated over the complete angle θ_2 in Regions 1 and 2 of the flow as shown in Figure A.1 to obtain

$$\int_{\theta_1}^{\theta_2} d\theta = \int_{M_1}^{M_2} \sqrt{M^2 - 1}\frac{dV}{V} \tag{A.11}$$

In order to evaluate the the right-hand side (RHS) of Equation A.12, the term dV/V must be obtained in terms of the Mach number, M. The Mach number is defined as the local velocity of the flow over the sonic speed of the flow (a). Hence, the local velocity of the flow is given by

$$V = Ma \tag{A.12}$$

Taking the natural logarithm of both sides of Equation A.12 gives

$$\ln V = \ln M + \ln a \tag{A.13}$$

Differentiating Equation A.13

$$\frac{dV}{V} = \frac{dM}{M} + \frac{da}{a} \tag{A.14}$$

The adiabitec energy equation is given by

$$\left(\frac{a_0}{a}\right)^2 = \frac{T_0}{T} = 1 + \frac{\gamma - 1}{2} M^2 \tag{A.15}$$

Solving for a from Equation A.15

$$a = a_0 \left(1 + \frac{\gamma - 1}{2} M_2\right)^{-\frac{1}{2}} \tag{A.16}$$

Differentiating Equation A.16

$$\frac{da}{a} = \frac{\gamma - 1}{2} M \left(1 + \frac{\gamma - 1}{2} M^2\right)^{-1} dM \tag{A.17}$$

Now, substituting Equation A.17 in Equation A.14

$$\frac{dV}{V} = \frac{1}{1 + \frac{\gamma-1}{2} M^2} \frac{dM}{M} \tag{A.18}$$

Substituting the developed relation between dV/V and M in the previous equation (Equation A.18) in Equation A.11

$$\int_{\theta_1}^{\theta_2} d\theta = \theta_2 - 0 = \int_{M_1}^{M_2} \frac{\sqrt{M^2 - 1}}{1 + \frac{\gamma-1}{2} M^2} \frac{dM}{M} \tag{A.19}$$

The RHS of Equation A.21 is known as the Prandtl-Meyer function and is denoted by the symbol ν. After evaluating the integral, the Prandtl-Meyer function becomes

$$\nu(M) = \sqrt{\frac{\gamma + 1}{\gamma - 1}} \tan^{-1} \sqrt{\frac{\gamma - 1}{\gamma + 1}(M^2 - 1)} - \tan^{-1} \sqrt{M^2 - 1} \tag{A.20}$$

Now, Equation A.21 can be evaluated as

$$\theta_2 = \nu(M_2) - \nu(M_1) \tag{A.21}$$

The Prandtl-Meyer function for air ($\gamma = 1.4$), along with the corresponding Mach angle, is tabulated in [21] as a function of the Mach number. With reference to Figure A.1, since the flow properties at Region 1 are known, the Prandtl-Meyer angle for Region 1 ($\nu(M_1)$) can be determined from the tabulated data. $\nu(M_1)$ and θ_2 can be used to calculate the Prandtl-Meyer angle in Region 2, $\nu(M_2)$. Subsequently, $\nu(M_2)$ can be used to determine the Mach number in Region 2, M_2. M_2 and M_1 are used to obtain the properties of the flow in Region 2 using the isentropic expansion relations.

APPENDIX B

THE METHOD OF CHARACTERISTICS AND CHARACTERISTIC LINES

This section describes the development and the philosophy of the method of characteristics and characteristic lines used in the development of the method used to design the contour of the aerospike nozzle, as shown by [21]. All information presented here is from [21] and a more detailed discussion is available in the original source.

THE METHOD OF CHARACTERISTICS

1. Definition. The method of characteristics is one of the oldest and most used numerical techniques for obtaining the solution of supersonic, steady, inviscid flows. The numerical method is highlighted by:

- The calculation of the properties of the flow field at discrete points in the flow-field.
- Expanding the flow-field properties in terms of a Taylor's series expansion.
- In the theoretical limit of an infinite number of grid points in the flow-field, the solutions provided by the method are exact and subject to a truncation error arising from neglecting the higher order terms in the Taylor's series expansion.

2. Characteristic lines. Consider the rectangular computational flow-field shown in Figure B.1, the flow properties at each of the grid points in the rectangular xy-space are either known or to be determined. The grid points are indexed by i and j in the x and y directions, respectively. For instance, the term $u_{i,j}$ denotes the known x component of velocity at point (i, j). The velocity at point $(i + 1, j)$ (the point to the right of (i, j)) can be obtained using Taylor's series expansion as the numerical method dictates

$$u_{i+1,j} = u_{i,j} + \left(\frac{\partial u}{\partial x}\right)_{i,j} \Delta X + \left(\frac{\partial^2 u}{\partial^2 x}\right)_{i,j} \frac{(\Delta x)^2}{2} + \ldots \tag{B.1}$$

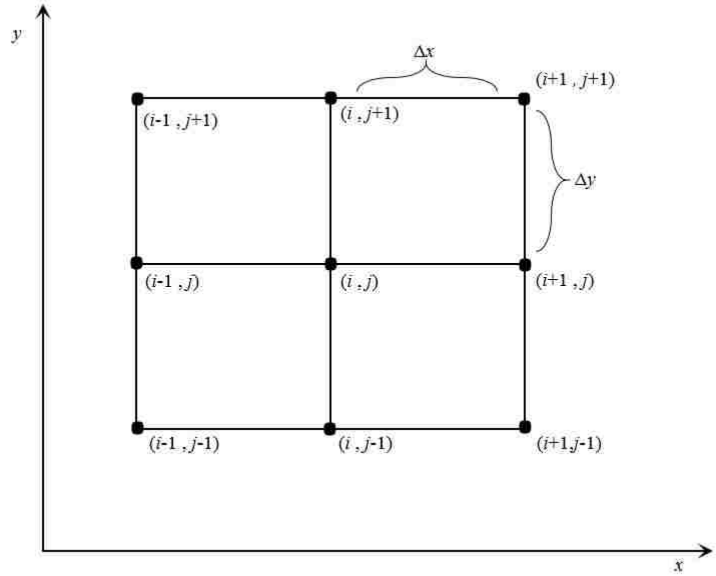

Figure B.1 Rectangular Computational Finite-Difference Flow-Field

Neglecting the higher-order terms in Equation B.1 gives

$$u_{i+1,j} = u_{i,j} + \left(\frac{\partial u}{\partial x}\right)_{i,j} \Delta X + \ldots \tag{B.2}$$

In order to determine the derivative $\partial u/\partial x$ in Equation B.2 the velocity potential equation for two-dimensional irrotational flow in terms of velocities must be considered. The velocity potential is given by

$$\left(1 - \frac{u^2}{a^2}\right)\frac{\partial u}{\partial x} + \left(1 - \frac{v^2}{a^2}\right)\frac{\partial v}{\partial y} - \frac{2uv}{a^2}\frac{\partial u}{\partial y} = 0 \tag{B.3}$$

Solving for the derivative $\partial u/\partial x$ in the velocity potential equation (Equation B.3)

$$\frac{\partial u}{\partial x} = \frac{\frac{2uv}{a^2}\frac{\partial u}{\partial y} - \left(1 - \frac{v^2}{a^2}\right)\frac{\partial v}{\partial y}}{\left(1 - \frac{u^2}{a^2}\right)} \tag{B.4}$$

Assuming that the velocity components u and v are known at every grid point along a vertical line as shown in Figure B.2. Meaning if the velocity and its components, u and v, are known at points $i, j)$, $(i, j-1)$, and $(i, j+1)$, and their derivatives in the y direction, $\partial u/$ and $\partial v/\partial y$, are known as well and in fact can be determined from the finite-difference quotients discussed in [21] and [35]. When the determined derivatives are substituted in Equation B.4, the right-hand side (RHS) of Equation B.4 yields a number for $\partial u/\partial x$ that in turn can be substituted in Equation B.2 to find $u_{i+1,j}$. However, a special case arises when the denominator of the RHS in Equation B.4 is equal to zero. Which causes the derivative $\partial u/\partial x$ to be indeterminate and sometimes even discontinuous. As seen in Figure B.2, this happens when the x-component of velocity, u, at $x = x_o$ is equal to the speed of sound, $u = a$. Using geometry to define the angle μ in Figure B.2 yields $\sin\mu = u/V = a/V = 1/M$. Hence, the angle μ is known as the Mach angle.

This implies that there exists a line that makes a Mach angle with respect to the direction of the streamline at a point along which the derivative of u is indeterminate and may even be discontinuous. These lines in the flow are known as the characteristic lines, and, as demonstrated above, they are also Mach lines. The derivatives of the other flow properties are also indeterminate along these lines.

Now that the characteristic lines definition is established, the method of characteristics can be outlined in three major steps.

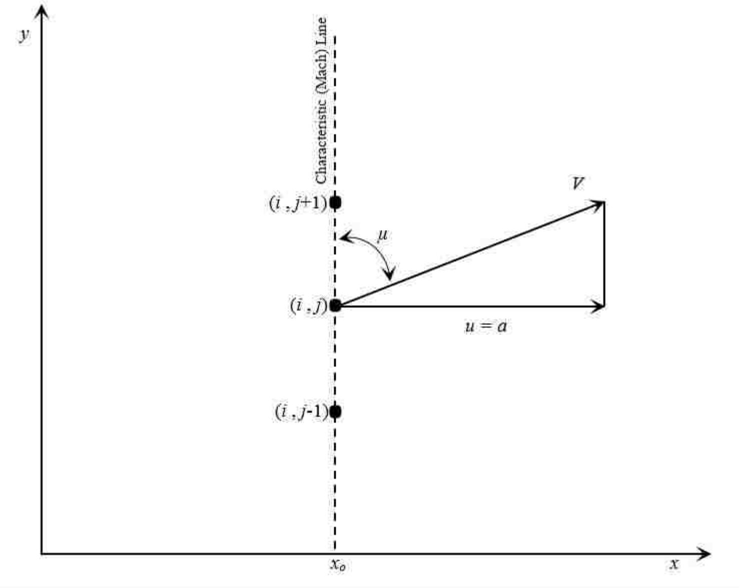

Figure B.2 Characteristic Line Illustration

STEP 1: DETERMINATION OF THE CHARACTERISTIC LINES

These are particular lines in the flow-field were the flow variables are continuous but their derivatives are indeterminate and sometimes even discontinuous. The characteristic lines can be determined by considering the governing equation of steady, adiabatic, two-dimensional, irrotational supersonic flow in terms of velocity potential given by

$$\left(1-\frac{\Phi_x^2}{a^2}\right)\Phi_{xx}+\left(1-\frac{\Phi_y^2}{a^2}\right)\Phi_{yy}-\frac{2\Phi_x\Phi_y}{a^2}\Phi_{xy}=0 \tag{B.5}$$

in which Φ is the full-velocity potential, and $\Phi_x = u$, $\Phi_y = v$. u and v are the x and y components of velocity, $\mathbf{V} = u\mathbf{i} + v\mathbf{j}$. The full velocity potential is a function of x and y, and $\Phi_x = f(x, y)$ hence

$$d\Phi_x = \frac{\partial \Phi_x}{\partial x} dx + \frac{\partial \Phi_x}{\partial y} dy = \Phi_{xx} dx + \Phi_{xy} dy \tag{B.6}$$

$$d\Phi_y = \frac{\partial \Phi_y}{\partial x} dx + \frac{\partial \Phi_y}{\partial y} dy = \Phi_{xy} dx + \Phi_{yy} dy \tag{B.7}$$

Rewriting and organizing Equations B.5 through B.7 yields

$$\left(1 - \frac{u^2}{a^2}\right) \Phi_{xx} - \frac{2uv}{a^2} \Phi_{xy} + \left(1 - \frac{v^2}{a^2}\right) \Phi_{yy} = 0 \tag{B.8}$$

$$(dx)\Phi_{xx} + (dy)\Phi_{xy} = du \tag{B.9}$$

$$(dx)\Phi_{xy} + (dy)\Phi_{yy} = du \tag{B.10}$$

Equations B.8 through B.10 can be put in a system of linear, algebraic equations with variables Φ_{xx}, Φ_{yy} and Φ_{xy}. The variables can be solved for using Cramer's rule. For example, solving for Φ_{xy}

$$\Phi_{xy} = \frac{\begin{vmatrix} 1-\frac{u^2}{a^2} & 0 & 1-\frac{v^2}{a^2} \\ dx & du & 0 \\ 0 & dv & dy \end{vmatrix}}{\begin{vmatrix} 1-\frac{u^2}{a^2} & -\frac{2uv}{a^2} & 1-\frac{v^2}{a^2} \\ dx & dy & 0 \\ 0 & dx & dy \end{vmatrix}} = \frac{N}{D} \tag{B.11}$$

Referring to Figure B.3, the velocity potential derivative Φ_{xy} of the streamline passing through point A has a specific value that can be found using Equation B.11 for an arbitrary dx and dy. The arbitrary choice of dx and dy values will yield corresponding values for velocity change du and dv, respectively. At point A, the values of du and dv will always yield the same value for the velocity potential for any chosen dx and dy. However, when the values for dx and dy make the denominator of Equation B.11 (D) equal to zero, then the velocity potential is not defined in that specific direction defined by the chosen dx and dy. A value of an infinite velocity potential is not physically consistent, as a result, if dx and dy give $D = 0$ in Equation B.11, then in order to keep the velocity potential finite, the numerator has to equal zero as well, i.e., $N = 0$ ($\Phi_{xy} = N/D = 0/0$). this means that the velocity potential at that point is indeterminate. Recall that the direction in the flow-field that yield indeterminate derivatives of the flow properties are characteristic lines. So, the lines in the flow-field that make $D = 0$ and $N = 0$ are characteristic lines.

Setting $D = 0$ in Equation B.11 gives

$$\left(1-\frac{u^2}{a^2}\right)\left(\frac{dy}{dx}\right)^2_{char} + \frac{2uv}{a^2}\left(\frac{dy}{dx}\right)_{char} + \left(1-\frac{v^2}{a^2}\right) = 0 \tag{B.12}$$

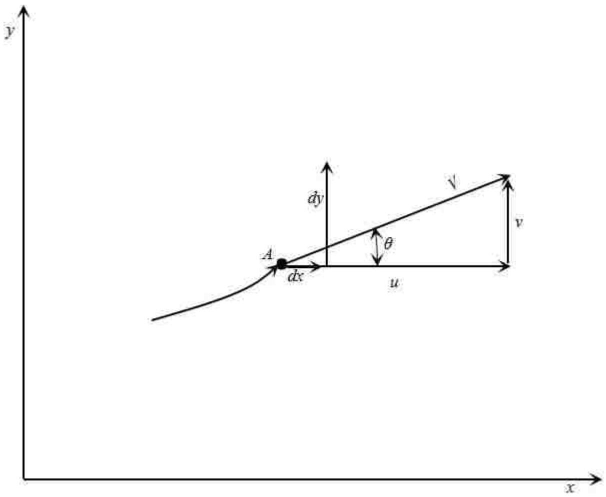

Figure B.3 Generic Geometry of a Streamline

where $(dy/dx)_{char}$ is the slope of the characteristic line. Treating the slope of the characteristic line as a variable and using the quadratic equation gives

$$\left(\frac{dy}{dx}\right)_{char} = \frac{-uv/a^2 \pm \sqrt{[(u^2+v^2)/a^2]}}{[1-(u^2/a^2)]} \tag{B.13}$$

The previous equation defines the characteristic curves in the xy-space. Further consideration of the term inside the square root in Equation B.13 shows that

$$\frac{u^2+v^2}{a^2} - 1 = \frac{V^2}{a^2} - 1 = M^2 - 1 \tag{B.14}$$

and the following conclusions about the characteristic lines and Equation B.5 can be established

- If $M > 1$, there will be two real characteristic lines through every point in the flow-field and Equation B.5 will be a hyperbolic partial differential equation (PDE).
- If $M < 1$, the characteristic lines are imaginary and Equation B.5 will be an elliptic PDE.
- If $M = 1$, there will be only on real characteristic line through every point in flow and Equation B.5 will be a parabolic PDE.

More about hyperbolic, elliptic, and parabolic partial differential equations can be found in [36].

It is obvious from the previous definitions that steady, inviscid flow in governed by hyperbolic PDEs. Referring back to Figure B.3, the following relations can be established

$$u = V \cos\theta \tag{B.15a}$$

$$v = V \sin\theta \tag{B.15b}$$

$$M^2 = \frac{V^2}{a^2} = \frac{1}{\sin\mu^2} \tag{B.15c}$$

Using Equations B.15a through B.15c in Equation B.13 yields

$$\left(\frac{dy}{dx}\right)_{char} = \frac{\frac{-\cos\theta\sin\theta}{\sin^2\mu} \pm \sqrt{\frac{\cos^{\theta} + \sin^2\theta}{\sin^2 /mu} - 1}}{1 - \frac{\cos^2\theta}{\sin^2\mu}} \tag{B.16}$$

Using trigonometry to manipulate the term inside the square root in Equation B.16

$$\sqrt{\frac{\cos^{\theta} + \sin^2\theta}{\sin^2 /mu} - 1} = \sqrt{\frac{1}{\sin^2\mu} - 1} = \sqrt{\csc^2\mu - 1} = \sqrt{\cot^2\mu} = \frac{1}{\tan\mu} \tag{B.17}$$

Substituting in Equation B.16 yields

$$\left(\frac{dy}{dx}\right)_{char} = \frac{-\cos\theta\sin\theta/\sin^2\mu \pm 1/\tan\mu}{1 - (\cos^2\theta/\sin^2/\mu)} \tag{B.18}$$

Equation B.18 in turn reduces to

$$\left(\frac{dy}{dx}\right)_{char} = \tan(\theta \mp \mu) \tag{B.19}$$

The importance of Equation B.19 can be summarized in Figure B.4. The streamline passing through point A makes an angle θ with the geometric x axis, and Equation B.19 shows that there are two characteristic lines (Mach lines) passing through point A both at an angle μ above and below the streamline. Furthermore, The characteristic line above the streamline, given by $\theta + \mu$, is typically referred to as the left running characteristic line and is denoted by C_+, and the characteristic line below the streamline given by $\theta - \mu$ is typically referred to as the right-running characteristic line and is denoted by C_-.

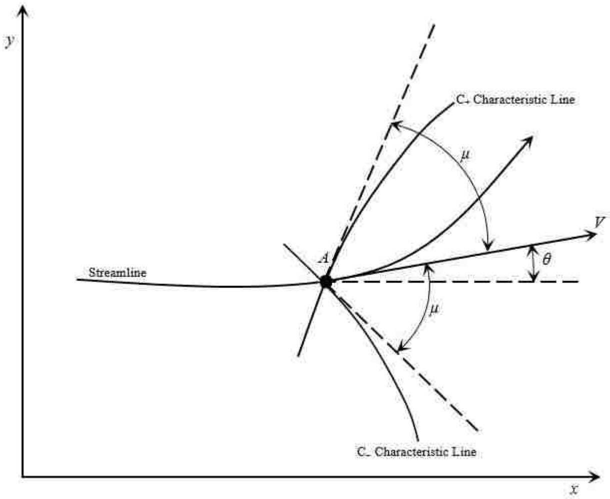

Figure B.4 Left- and Right- Running Characteristic Lines

STEP 2: DETERMINATION OF THE COMPATIBILITY EQUATIONS

After determining the characteristic lines and the the direction of the characteristics line by setting $D = 0$ in Equation B.11, the second step in the method of characteristics is determining the compatibility equations by, consequently setting $N = 0$ in Equation B.11. For two-dimensional, steady, adiabtic, irrotational flow, the compatibility equations are a combination of the continuity, momentum, and energy equations and they can be related to the Prandtl-Meyer function, as shown below. Setting $N = 0$ and solving in terms of dv/du yields the following equation

$$\frac{dv}{du} = \frac{-[1 - (u^2/a^2)]dy}{[1 - (v^2/a^2)]dx} \tag{B.20}$$

The dy/dx term in Equation B.20 is in fact $(dy/dx)_{char}$ found in Step 1, because when $N = 0$ we are restricted to only consider the case when $D = 0$ to keep the flow derivatives finite as previously explained.

Using Equation B.13 in Equation B.20 yields

$$\frac{dv}{du} = \frac{\frac{uv}{a^2} \mp \sqrt{\frac{u^2+v^2}{a^2} - 1}}{1 - \frac{v^2}{a^2}} \tag{B.21}$$

Using Equations B.15a and B.15b in Equation B.21

$$\frac{d(V\sin\theta)}{d(V\cos\theta)} = \frac{M^2\cos\theta\sin\theta \mp \sqrt{M^2-1}}{1 - M^2\sin^2\theta} \tag{B.22}$$

which in turn reduces to

$$d\theta = \mp\sqrt{M^2-1}\frac{dV}{V} \tag{B.23}$$

Equation B.23 is the compatibility equation that defines the change in the properties of the flow-field along a characteristic line. It is important to note that Equation B.23 is the same as Equation A.10 For Prandtl-Meyer flow, which means that Equation B.23 can be integrated to give the Prandtl-Meyer function and allow the replacement for the compatibility equations by the following algebraic compatibility equations

$$\theta + \nu(M) = constant = K_{-} \tag{B.24}$$

$$\theta - \nu(M) = constant = K_{+} \tag{B.25}$$

Equation B.24 relates the velocity magnitude and direction along the C_{-} characteristic line, and Equation B.25 relates the velocity magnitude and direction along the C_{+} characteristic line. The K_{-} and K_{+} constants are analogous to the Riemann invariants for unsteady flow. More detailed information on the Riemann function and Riemann invariants is given in [36], [21] and [35].

STEP 3: SOLVING THE COMPATIBILITY EQUATIONS

Starting from the given initial conditions of the flow-field the compatibility equations developed in Step 2 are solved step-by-step along the characteristic lines. This allows the flow-field to be mapped completely along the characteristic lines and establish what is known as the "characteristic net." The characteristics and the compatibility equations must be determined and solved simultaneously. For two-dimensional, irrotational flow, the compatibility equations become algebraic equations independent of geometric locations as shown in Step 2. The processes, of applying the method of characteristics to a certain flow-field, are known as "unit processes." Unit processes vary for different points depending on their location in the flow-field; internal, on a free boundary (wall), or on a shock wave. The unit processes are outlined and discussed in detail in the original source of this discussion [21], and they serve as the principal technique of the nozzle contour design process.

APPENDIX C

NOZZLE DESIGN AND PERFORMANCE ANALYSIS MATLAB CODES

Different MATLAB programs used to design the aerospike nozzle and perform preliminary propulsion system performance are presented in this section.

NOZZLE CONTOUR DESIGN

```
% Date: 11/8/2015
% Description: This script finds the contour of an annular axisymmetric
% aerospike nozzle based on the mathmatical formulation outlined in the
% reference given below.
% Reference: 'Approximate Method for Plug Nozzle Design' by G. Angelino
% note: the equation for 'alpha' in Equation (5) in the above reference is
% wrong. The correct equation for alpha is: [alpha = nu_e - nu(M) + mu(M)]
%_______Thanks to Austin Holmsley for the great help
    _____________________________________________
% Inputs: - Expansion ratio [AR]
%       - ratio of specific heats [gamma]
%       - non-dimensional radius at end of spike [eta_b] (zero for a
%         non-truncated spike)
% Outputs: x,y coordinates of an axisymmetric spike contour
%_________________________________________________________________________
% Functions used: - Mach2AR, AR2Mach (convert between Area ratio and Mach)
%              - Mach2Prandtl (convert from Mach to Prandtl-Meyer angle)
%              - Mach2Mangle (convert Mach to Mach angle)
%_________________________________________________________________________
% note: these coordinates are revolved around the central axis to obtain
% the 3-D spike
%_________________________________________________________________________
% all non-dimensional values are non-dimensionalized by [r_e] the exit
% radius of the spike (see Figure 1b. in the Reference)
```

```
AR = 6.05;
gamma = 1.1251;
eta_b = 0.06;

% input tube inner diameter (the units of this parameter determine the units of
    the dimensional results)
t_diam = ("input value of tube diameter");
A_t = pi*((t_diam/2)^2); % throat area
A_e = AR*A_t;
r_e = sqrt(A_e/pi);

M_e = AR2Mach(AR,gamma);
nu_e = Mach2Prandtl(M_e,gamma);
N = 10000000;
M_vals = linspace(1,M_e,N);
AR_vals = Mach2AR(M_vals,gamma);
nu_vals = Mach2Prandtl(M_vals,gamma);
mu_vals = Mach2Mangle(M_vals);
alpha_vals = nu_e-nu_vals+mu_vals;

% non-dimensional values
l_nondim_vals = (1-sqrt(1-(AR_vals.*(1-(eta_b.^2)).*M_vals.*(sin(alpha_vals)./AR))
    ))./sin(alpha_vals);
r_nondim_vals = 1-(l_nondim_vals.*sin(alpha_vals));
x_nondim_vals = l_nondim_vals.*cos(alpha_vals);
y_nondim_vals = l_nondim_vals.*sin(alpha_vals);
Length_nondim = max(x_nondim_vals)-min(x_nondim_vals);

% dimensional values
l_vals = l_nondim_vals.*r_e;
```

```
r_vals = r_nondim_vals.*r_e;
x_vals = x_nondim_vals.*r_e;
y_vals = y_nondim_vals.*r_e;
Length = Length_nondim.*r_e;

%Plotting
figure
plot(r_nondim_vals,x_nondim_vals);
xlabel('r/r_e')
ylabel('x/r_e')
figure
plot(x_nondim_vals,y_nondim_vals,0,0,'o');
xlabel('x/r_e')
ylabel('y/r_e')

fprintf('Exit Mach number = %g \n',M_e)
fprintf('Length = %g [in] \n',Length)
fprintf('Cowl Seperation = %g [in] \n \n',min(l_vals))
fprintf('Flow Turn Angle = %g [deg] \n',nu_e*180/pi)

% Create a text file containing coordinates for input in CAD
n = 500;
m = N/n;
p = length(x_vals);
x = x_vals(1:m:p);
y = y_vals(1:m:p);
z = zeros(1,n);

A = [x;y;z];
fileID = fopen('Angelino_Aerospike.txt','w');
```

```
fprintf(fileID,'%6.10f %12.10f %12.10f\n',A);
fclose(fileID);
```

SUB-FUNCTIONS USED IN THE NOZZLE DESIGN CODE

```
% Description: Sub-program Uses the secant method to find the Mach number
% associated with a given Prandtl-Meyer angle.

function M = Prandtl2Mach(nu,gamma)

M0u = 6; % first initial guess (upper bound)
M0l = 1.25; %second initial guess (lower bound)
maxits = 50; % maximum number of iterations
tolerance = 0.000001; % tolerance
i = 0; % initialize i
f1 = sqrt((gamma+1)/(gamma-1)); % constant function of gamma
f2 = sqrt((gamma-1)/(gamma+1)); % constant function of gamma

f = f1*atan(f2*sqrt((M0u^2)-1))-atan(sqrt((M0u^2)-1))-nu; % Prandtl-Meyer function
    : f(M) - nu = 0
j = abs(f); % initialize j which checks how close to zero our current guess gets
    us

while j>tolerance && i<=maxits

   f = f1*atan(f2*sqrt((M0l^2)-1))-atan(sqrt((M0l^2)-1))-nu;
   k = f1*atan(f2*sqrt((M0u^2)-1))-atan(sqrt((M0u^2)-1))-nu;
   y = (M0l*k-M0u*f)/(k-f);
   M0l = M0u;
   M0u = y;
   f = f1*atan(f2*sqrt((M0u^2)-1))-atan(sqrt((M0u^2)-1))-nu;
```

```
    j = abs(f);
    i = i+1;

end
M = M0u;
end

%Converting Mach number to Prandtl-Meyer angle
function [nu] = Mach2Prandtl(M,gamma)
f1 = (gamma+1)/(gamma-1);
f2 = 1/f1;
nu = sqrt(f1).*atan(sqrt((f2.*((M.^2)-1))))-atan(sqrt((M.^2)-1));
end

% Getting the Mach angle from Mach number
function [mu] = Mach2Mangle(M)
mu  = asin(1./M);
end

% Mach number to area ratio (AR)
function [AR] = Mach2AR(M,gamma)
f1 = 2/(gamma+1);
f2 = (gamma-1)/2;
f3 = (gamma+1)/(gamma-1);
AR = sqrt((1./(M.^2)).*((f1.*(1+(f2.*(M.^2)))).^f3));
end

% Area ratio to Mach number
function [M] = AR2Mach(AR,gamma)
f1 = 2/(gamma+1);
```

```
f2 = (gamma-1)/2;
f3 = (gamma+1)/(gamma-1);
M0 = 4;
M = M0;
Function = (1/(M^2))*((f1*(1+(f2*(M^2))))^f3)-(AR^2);
Tolerance = 0.0001;
maxits = 200;
J = abs(Function);
i = 1;
while J>Tolerance && i<=maxits
    Function = (1/(M^2))*((f1*(1+(f2*(M^2))))^(f3))-(AR^2);
    dFunction = (f3/(M^2))*((f1*(1+(f2*(M^2))))^(f3-1))*2*f2*f1*M + (-2/(M^3))*((f1
        *(1+f2*(M^2)))^(f3));
    y = M-(Function/dFunction);
    M = y;
    Function = (1/(M^2))*((f1*(1+(f2*(M^2))))^(f3))-(AR^2);
    J = abs(Function);
    i = i+1;
end
end
```

EVALUATING DIFFERENT PROPELLANTS' PERFORMANCE

```
% CubeQuest Propulsion Subsystem
% Fluid Dynamic and Thermal Analysis of CubeQuest Prop System: Code evaluates the
    %performance of different propellants. The proprieties of the different
    propellants were %found using EES (Engineering Equation Solver)
% Equations created using the isentropic 1-D analysis approach
P_tank = 300; % [psi]
V = .00470685;
```

```
%Initializing

Temp = 30; % [C]

DV = [0,0,0,0];

Best = [0,0,0,0];

Pressure = [0,0,0,0];

SpecificImpulse = [0,0,0,0];

PropMass = [0,0,0,0];

BestThrust = [0,0,0,0];

i = 1;

for P_tank = 200:100:500

for propellant = 1:6


% Conversion Ratios

Psi_to_Pa = 6894.76;% 1 psi to 6894.76 Pa

C_to_Kelvin = 273.15;


P = 24.7;


T_0 = Temp + C_to_Kelvin; % Initial tank temp (static/total) [K]

P_0 = P_tank*Psi_to_Pa;  % Initial tank total pressure [N/m^2]

R_univ = 8.314;          % Universal gas constant [J/mol-K]

g0 = 9.81;               % Gravitational accel [m/s^2]


%Tabulation of gas characteristics for each propellant type

if propellant == 1 %R410a


Prop = 'R410a ';

MW = 0.07258; % [kg/mol]

R = R_univ/MW;
```

```
% Found using EES
if P_tank == 200
Cp = 1168; % [J/(kg*K)]
Cv = 839.6; % [J/(kg*K)]
mp = .2318; % [kg]
end

if P_tank == 300
Cp = 1759; % [J/(kg*K)]
Cv = 930.2; % [J/(kg*K)]
mp = 4.872; % [kg]
end

if P_tank == 400
Cp = 1727; % [J/(kg*K)]
Cv = 925.8; % [J/(kg*K)]
mp = 4.908; % [kg]
end

if P_tank == 500
Cp = 1699; % [J/(kg*K)]
Cv = 922.2; % [J/(kg*K)]
mp = 4.942; % [kg]
end
end

if propellant == 2 %R22

Prop = 'R22 ';
MW = 0.086476;
```

```
R = R_univ/MW; % [kg/mol]

% Found using EES

if P_tank == 200

Cp = 1280; % [J/(kg*K)]

Cv = 689; % [J/(kg*K)]mp = 5.519; % [kg]

end


if P_tank == 300

Cp = 1270; % [J/(kg*K)]

Cv = 679.9; % [J/(kg*K)]

mp = 5.54; % [kg]

end


 if P_tank == 400

Cp = 1260; % [J/(kg*K)]

Cv = 697.8; % [J/(kg*K)]

mp = 5.561; % [kg]

end


if P_tank == 500

Cp = 1251; % [J/(kg*K)]

Cv = 697.8; % [J/(kg*K)]

 mp = 5.581; % [kg]

end

end


if propellant == 3 %R23

Prop = 'R23 ';

MW = 0.07002;  % [kg/mol]

R = R_univ/MW;
```

```
% Found using EES
if P_tank == 200
Cp = 875.5; % [J/(kg*K)]
Cv = 672.8; % [J/(kg*K)]
mp = .2016; % [kg]
end

if P_tank == 300
Cp = 979.4; % [J/(kg*K)]
Cv = 704.8; % [J/(kg*K)]
mp = .3239; % [kg]
end

if P_tank == 400
Cp = 1131; % [J/(kg*K)]
Cv = 742.9; % [J/(kg*K)]
mp = .469; % [kg]
en

if P_tank == 500
Cp = 1381; % [J/(kg*K)]
Cv = 789.8; % [J/(kg*K)]
mp = .65; % [kg]
end
end

if propellant == 4 %R134a
Prop = 'R134a ';
MW = 0.10203; % [kg/mol]
R = R_univ/MW;
```

```
% Found using EES
if P_tank == 200
Cp = 1438; % [J/(kg*K)]
Cv = 918.3; % [J/(kg*K)]
mp = 5.608; % [kg]
end

if P_tank == 300
Cp = 1430; % [J/(kg*K)]
Cv = 917.7; % [J/(kg*K)]
end

if P_tank == 400
Cp = 1422; % [J/(kg*K)]
Cv = 917.2; % [J/(kg*K)]
mp = 5.649; % [kg]
end

if P_tank == 500
Cp = 1414; % [J/(kg*K)]
Cv = 916.8; % [J/(kg*K)]
mp = 5.668; % [kg]
end

end

if propellant == 5 %R152a
Prop = 'R152a ';
MW = 0.06605; % [kg/mol]
```

```
R = R_univ/MW;

% Found Using EES
if P_tank == 200
Cp = 1827; % [J/(kg*K)]
Cv = 1162; % [J/(kg*K)]
mp = 4.184; % [kg]
end

if P_tank == 300
Cp = 1818; % [J/(kg*K)]
Cv = 1161; % [J/(kg*K)]
mp = 4.197; % [kg]
end

if P_tank == 400
Cp = 1810; % [J/(kg*K)]
Cv = 1160; % [J/(kg*K)]
mp = 4.209; % [kg]
end

if P_tank == 500
Cp = 1803; % [J/(kg*K)]
Cv = 1159; % [J/(kg*K)]
mp = 4.221; % [kg]
end
end

if propellant == 6 %R290 (Propane)
Prop = 'Propane ';
```

```
MW = 0.159808;  % [kg/mol]
R = R_univ/MW;
% Found Using EES
if P_tank == 200
Cp = 2782; % [J/(kg*K)]
Cv = 1686; % [J/(kg*K)]
mp = 2.283; % [kg]
end
if P_tank == 300
Cp = 2758; % [J/(kg*K)]
Cv = 1686; % [J/(kg*K)]
mp = 2.294; % [kg]
end
if P_tank == 400
Cp = 2737; % [J/(kg*K)]
 Cv = 1686; % [J/(kg*K)]
mp = 2.304; % [kg]
end
if P_tank == 500
Cp = 2717; % [J/(kg*K)]
Cv = 1686; % [J/(kg*K)]
mp = 2.314; % [kg]
end
end
gamma = Cp/Cv; % Specific Heat Ratio
P_reg = P*Psi_to_Pa;% Regulated static pressure (See below for iteration where
    this is assumed to be total pressure change)
Ae = 0.0852287235*0.00064516; % Nozzle exit area [m^2]
A_star = 0.0124942926*0.00064516; % Nozzle throat area [m^2]
AR = Ae/A_star; %Exit to throat area ratio
```

```
ar = 1;       %Initial approx for exit to throat area
Me_approx = 1; %Initial approx for exit mach number
n = 0;        %Matrix index
while ar <= AR %Uses Area-Mach Relation for isentropic flow to approximate the
    mach number at the exit
n = n+1;
Me_approx = Me_approx + 0.0001;
ar = (1/Me_approx)*((2/(gamma+1))*(1 +(((gamma-1)/2)*(Me_approx^2))))^((gamma+1)
    /(2*(gamma-1)));
M_exit(n) = Me_approx;
end
M_exit = M_exit(n); %Final approx for exit mach number without overshooting area
    ratio
tol = 1e-2;
% No Heat addition
T_tot_exit = T_0;
T_exit = T_tot_exit/(1 + (gamma-1)/2*M_exit^2);
% Assuming isentropic nozzle, total temp and pressure constant throughout
% Pressure losses in the lines and the pressure regulator can be assumed to
% be negligible
% P_tot_exit = P_0; % Total Pressure at exit (no losses) - A knockdown factor can
    be added to account for real flow through lines, regulator, and HEX
% P_exit = P_tot_exit/(1+((gamma-1)/2)*M_exit^2)^(gamma/(gamma-1));

% This iteration assumes that the regulated pressure is the new total
% pressure that the nozzle HEX, lines, and nozzle inlet will experience.
%----------------------------------------------------------------------------
P_exit = P_reg/(1+((gamma-1)/2)*M_exit^2)^(gamma/(gamma-1)); % Static exit
    pressure
P_tot_exit = P_exit*(1+((gamma-1)/2)*M_exit^2)^(gamma/(gamma-1));
```

```
%-------------------------------------------------------------------------
ue = M_exit*sqrt(gamma*R*T_exit(end)); % Propellant velocity at nozzle exit [m/s]
c_star = (((gamma+1)/2)^((gamma+1)/(2*(gamma-1))))*sqrt(R*T_tot_exit/gamma); %[m/s
    ]

% Max max flow rate at choke-point of nozzle
mdot = (P_tot_exit*A_star)/c_star; % [kg/s]

Thrust = mdot*ue + P_exit*Ae; % Thrust produced [N]
Isp = Thrust/(mdot*g0);     % Specific Impulse [s]
c = Isp*g0;    % Effective exhaust velocity [m/s]

md = 4.8953; % Dry mass of CubeQuestador including all components minus fuel [kg]
TankVol = 0.00470685; % Available Tank Volume [m^3]

mp_0 = mp; % Porpellant mass [kg]
m0 = mp_0+md; % Total mass [kg]
MR = m0/md;
DeltaV = c*log(MR); % DeltaV [m/s]
burn_time = mp_0/mdot;

if DeltaV > DV(i)
   DV(i) = DeltaV;
   Best(i) = propellant;
   Pressure(i) = P_tank;
   SpecificImpulse(i) = Isp;
   PropMass(i) = mp;
   BestThrust(i) = Thrust;
end
end
```

```
i = i+1;
end
fprintf('\n\n')

Properties = {'Best Propellant';'DeltaV (m/s)';'Propellant Mass (kg)';'Isp (s)';'
    Thrust (N)'};

P200 = {'R152a';num2str(DV(1));num2str(PropMass(1));num2str(...
    SpecificImpulse(1));num2str(BestThrust(1))};
P300 = {'R152a';num2str(DV(2));num2str(PropMass(2));num2str(...
    SpecificImpulse(2));num2str(BestThrust(2))};
P400 = {'R152a';num2str(DV(3));num2str(PropMass(3));num2str(...
    SpecificImpulse(3));num2str(BestThrust(3))};
P500 = {'R152a';num2str(DV(4));num2str(PropMass(4));num2str(...
    SpecificImpulse(4));num2str(BestThrust(4))};

% Table Showing Properties of the Best Propellant at different Tank
% Pressures P200 = Tank Pressure of 200 psi
F = table(P200,P300,P400,P500,'RowNames',Properties);
disp(F)
```

BIBLIOGRAPHY

[1] Sputnik 1, 2015. URL https://www.nasa.gov/multimedia/imagegallery/image_feature_924.html.

[2] Sputnik's Impact on America, 2007. URL http://www.pbs.org/wgbh/nova/space/sputnik-impact-on-america.html.

[3] Henry Helvajian and Siegfried W. Janson, editors. *Small Satellites: Past, Present, and Future*. The Aeropsace Press, El Segundo, CA, U.S.A, 1st. edition, 2008.

[4] Mission to Earth: Explorer 1. URL http://www.jpl.nasa.gov/missions/explorer-1/.

[5] Explorer and Early Satellites, . URL https://www.nasa.gov/mission_pages/explorer/explorer-overview.html.

[6] Vanguard I, . URL http://nssdc.gsfc.nasa.gov/nmc/spacecraftDisplay.do?id=1958-002B.

[7] James R. Wertz, David F. Everett, and Jeffery J. Puschell. *Space Mission Engineering: The New SMAD*. Microcosm, Inc., Howthorne, California, U.S.A, 2011. ISBN 978-1-881-883-15-9.

[8] G. P. Sutton and O. Biblarz. *Rocket Propulsion Elements*. John Wiley Sons, Inc., New Jersey, U.S.A, 8^{th} edition, 2010. ISBN 978-0-470-08024-5.

[9] Ryan Alan Pahl. Integration and Test of a Refrigerant-Based Cold-Gas Propulsion System for Small Satellites. Masters thesis, Rolla, Missouri, U.S.A., 2010.

[10] Philip G. Hill and Carl Peterson. *Mechanics and Thermodynamics of Propulsion*. Addison-Wesley Publishing Company, Inc., U.S.A., 2^{nd} edition, 1992. ISBN 0-201-470-14659-2.

[11] Carl Reiner Seubert. Refrigerant-Based Propulsion System for Small Spacecraft. Masters thesis, Missouri University of Science and Technology, Rolla, Missouri, U.S.A., 2007.

[12] SNAP-1: The Mission, 2016. URL https://www.sstl.co.uk/Missions/SNAP-1-Launched-2000/SNAP-1/SNAP-1-The-Mission.

[13] ESA Proba-2 Fact Sheet, 2009. URL http://esamultimedia.esa.int/docs/Proba/Proba-2_Factsheet_8oct.pdf.

[14] Gas Propulsion System, 2016. URL https://www.sstl.co.uk/Products/Subsystems/Propulsion-Systems/Gas-Propulsion-System.

[15] CryoSat Mission Overview, 2016. URL http://m.esa.int/Our-Activities/Observing-the-Earth/The-Living_Planet-Programme/Earth-Explorers/CryoSat-2/Overview.

[16] CryoSat-2, 2016. URL https://eoportal.org/web/eoportal/satellite-missions/c-missions/cryosat-2#spacecraf.

[17] M-SAT Mission Statement, 2015. URL http://web.mst.edu/~mrsat/about.htm.

[18] University Nanosat Program (UNP), 2013. URL http://prs.afrl.kirtland.af.mil/UNP/About.aspx.

[19] University Nanosat Program, 2006. URL http://www.vs.afrl.af.mil/UNP/index.html.

[20] Joshua L. Rovey. Multi-mode Microtube-Electrospray Propulsion - Aerospace Plasma Laboratory. 2016. URL http://campus.mst.edu/aplab/index_files/2016May-APLab-OngoingProjects.pdf.

[21] John D. Anderson. *Modern Compressible Flow: With Historical Perspective*. McGraw-Hill Companies, Inc., 3^{rd} edition, 2003. ISBN 0-07-242443-5.

[22] G. V. R. Rao. Exhaust Nozzle Contour For Optimum Thrust. *Journal of Jet Propulsion*, 28:377–382, 1958.

[23] Falcon 9, 2016. URL http://www.spacex.com/falcon9.

[24] Ken Davidian. The Aerospike Nozzle, 1999. URL http://www.hq.nasa.gov/pao/History/x-33/aero_faq.htm.

[25] Linear Aerospike Engine, Propulsion for the X-33 Vehicle, 2000. URL http://www.nasa.gov/centers/marshall/news/background/facts/aerospike.html.

[26] Eric Besnard, Hsun Hu Chen, and Tom Mueller. Design, Manufacturing and Test of A plug Nozzle Rocket Engine. (02-4038), 2002.

[27] Firefly α, 2016. URL http://www.fireflyspace.com/vehicles/firefly-b.

[28] Shannon Eilers and Stephen Whitmore. Development and Testing of a Multiple Use Plug Hybrid (for) Nanosats (MUPHyN). 26th Annual AIAA/USU Small Satellite Conference, 2012.

[29] Missouri University of Science and Technology-Missouri Satellite Research Team - CubeQuest Propulsion Subsystem PRP Rev 7831. 2016.

[30] M. C. Christe. Propellant Selection for a Nanosat Cold Gas, Low pressure, Propulsion System. *AIAA Student Conference Paper, Region V*, 2006.

[31] M.J.L. Turner. *Rocket and Spacecraft Propulsion: Principles, Practice and New Developments*. Springer Praxis Books. Springer Berlin Heidelberg, 2008. ISBN 9783540692034. URL https://books.google.com/books?id=xBYYasVPpvAC.

[32] Giafranco Angelino. Approximate method for plug nozzle design. *AIAA Journal*, 2 (10):1834–1835, 1964.

[33] ANSYS Inc. *ANSYS FLUENT User's Guide*. ANSYS, Canonsburg, PA, 2011.

[34] Tayo Ladeinde and Hsun Chen. Performance Comparison of a Full-Length and a Truncated Aerospike Nozzle. (10-6593), 2010.

[35] J. Anderson. *Computational Fluid Dynamics*. Computational Fluid Dynamics: The Basics with Applications. McGraw-Hill Education, 1995. ISBN 9780070016859. URL https://books.google.com/books?id=dJceAQAAIAAJ.

[36] W.A. Strauss. *Partial Differential Equations: An Introduction, 2nd Edition*. Wiley Global Education, 2007. ISBN 9781118313169. URL https://books.google.com/books?id=OWocAAAAQBAJ.

VITA

Abdalla Bani was born in Tripoli, Libya to Ali and Samira Bani. He was the second of three siblings. He graduated from high school in Tripoli and went to the University of Tripoli to pursue a degree in Electrical Engineering. In 2009 he decided to join the Missouri University of Science and Technology Electrical Engineering Department. But during the second semester of his freshman year Abdalla decided to join the Mechanical and Aerospace Engineering (MAE) Department. He earned his Bachelor of Science in Aerospace Engineering in May 2013. After earning his bachelor's degree, Abdalla Decided to continue his education and pursue a master's degree in Mechanical Engineering. In December 2016, Abdalla received a Master of Science in Mechanical Engineering.

During his years at Missouri University of Science and Technology, Abdalla was a graduate teaching assistant in the MAE department and also worked with the Office of International Affairs. Abdalla was a member of the Missouri University of Science and Technology Research Satellite Team (M-SAT) propulsion subsystem. He was also an AIAA and ASME member. Upon his B.S. graduation in 2013, Abdalla and his senior design teammate, Tyler Martin, formed The Orion Fund: Pursuit of Life Scholarship. The scholarship offers a monetary vote of confidence in the success of a promising individual who had to overcome adversity. Abdalla and Tyler served as chairpersons of the fund.